

SHAPE MEMORY POLYMERS AS DIRECT CONTACT DRY ADHESIVES FOR
TRANSFER PRINTING AND GENERAL USE

BY

JEFFREY D. EISENHAURE

DISSERTATION

Submitted in partial fulfillment of the requirements
for the degree of Doctor of Philosophy in Mechanical Engineering
in the Graduate College of the
University of Illinois at Urbana-Champaign, 2017

Urbana, Illinois

Doctoral Committee:

Assistant Professor Seok Kim, Chair
Professor Placid Ferreira
Professor Moonsub Shim
Assistant Professor SungWoo Nam

Abstract

For most diminutive life on Earth, control over external adhesive forces is crucial for survival. As humans, we pay little notice because at our scale inertial forces typically overwhelm adhesive forces by a wide margin. Nonetheless, the study and development of dry adhesives, which rely on ubiquitous intermolecular attractions to repeatedly form and break attachment to their adherends, have garnered substantial interest in recent decades. High performance artificial dry adhesives may unlock the door for many exciting new technologies from nanoscale manufacturing to wall climbing robots, but thus far the challenges have proven substantial and few successful commercial applications have come to fruition.

This dissertation represents an initial investigation into the benefits and potential limitations of developing shape memory polymer (SMP)-based dry adhesives. Prior to the presentation of experimental results, a review of the current state of dry adhesive knowledge including both theory, observations of the natural world, and lessons learned by other researchers in their attempts to develop a wide variety of synthetic dry adhesives is provided. It is concluded that dry adhesives fundamentally function through careful control of elastic energy, an idea that is very well suited to explore using SMPs which offer a large change in compliance across their thermal transition temperature. Thermoset epoxy SMPs are identified as an ideal choice for the investigation due to their mechanical strength, chemical resistance, manufacturability and convenient glass transitions among other features. The dry adhesive performance of a selected SMP is first evaluated for the purpose of microscale transfer printing, wherein micro-objects are assembled through precise control of adhesive surface forces. Significant benefits over existing solutions in terms of maximum adhesive strength during loading (~ 7 MPa), minimum strength for release (~ 0 MPa), and process versatility are confirmed, culminating in demonstrations of several challenging assemblies. The increase in adhesive strength is explained by invoking arguments from linear fracture mechanics and considering the dramatic compliance change experienced by the SMP between bond and load events. Advanced methods of heating and meaningful steps towards commercial-scale parallel printing processes are demonstrated.

The suitability of SMP for larger-scale applications is considered next. Strength rivaling or exceeding known alternatives is demonstrated, showing adhesion exceeding 2 MPa for 6 mm diameter adhesives while retaining excellent releasability through the use of microstructuring. A method of internally heating the SMP by adding conductive carbon nanoparticles is explored, including quantitative analyses of conductivity and the SMP composite's storage and loss moduli. The resulting flexible and conductive bi-layer SMP adhesive supports load while attached to surfaces of varied curvature. Variations on the SMP formula have their adhesive and mechanical properties tested, and are used to produce a self-contained SMP prototype wall-hanging adhesive.

Acknowledgements

First and foremost I must thank my wonderful wife Elizabeth, who has lovingly and patiently been at my side, offering words of encouragement, innumerable meals, and an apparently inexhaustible supply of humorous song lyrics throughout the latter half of my graduate career. I could not have even started my graduate studies were it not for my parents, Paul and Katherine, who have always helped and encouraged me to succeed and pursue my goals. I attribute much of my success towards my brother, Tom, who has always set the best example that I could hope to follow.

The work presented in this dissertation would not have been possible without the constant efforts of my adviser, Professor Seok Kim, who provided not only funds and ideas, but wise and patient guidance throughout my time as a graduate researcher. Much of my work would have likewise been exceedingly difficult without the assistance and advice from my graduate colleagues and co-authors, particularly with respect to their efforts in microfabrication and finite element analysis. Hohyun Keum, Sang-Il Rhee, and Junkyu Park especially spent many long hours in the cleanroom in service to my transfer printing experiments. The majority of microfabrication work, all original electron microscopy images, and nearly all material analysis provided herein were gathered only with the assistance of staff at the Frederick Seitz Materials Research Laboratory. In particular Scott MacLaren's help with AFM analysis and Kathleen Walsh's attention to the dynamic mechanical analysis equipment made my life substantially easier. I must also thank the staff within the Mechanical Science and Engineering department, including Katherine Smith who always cheerfully helped me to navigate the complexities of administrative matters and Laurie Macadam who placed and tracked orders for nearly every nut and bolt I used for the past six years. Finally, I must thank the members of my committee who have graciously offered their time and attention to review and advise my work to ensure its quality and completeness.

Table of Contents

Chapter 1. Introduction.....	1
1.1 Transfer Printing and the Role of Dry Adhesion	2
1.2 Other Current and Potential Artificial Dry Adhesive Applications	3
Chapter 2. Dry Adhesive Design and Characterization.....	4
2.1 Desirable Properties for Dry Adhesive Systems	4
2.1.1 Strong and Reversible Adhesion.....	4
2.1.2 High Adhesion to Preload Ratio	5
2.1.3 Durability	6
2.2 Performance Metrics	6
2.3 Test Methods	9
2.4 Fundamental Concepts for Creating a Dry Adhesive System.....	11
2.4.1 Attractive Forces.....	11
2.4.2 Controlling Elastic Energy.....	13
2.4.3 Enhancing Work of Adhesion Through Energy Dissipation and Absorption.....	18
Chapter 3. Existing Strategies for Creating a Successful Dry Adhesive.....	22
3.1 Observations of Natural Systems	22
3.2 Biomimetic Artificial Fibrillar Dry Adhesives	26
3.2.1 Benefits and Challenges of Artificial Fibrillar Designs.....	27
3.2.2 Fabrication Techniques and Scaling Issues	31
3.3 Alternative Strategies for Enhancing Artificial Dry Adhesive Performance	33
3.4 The Use of Shape Memory Polymers in Dry Adhesive Systems.....	35
Chapter 4. The Use of Shape Memory Polymers for Transfer Printing	38
4.1 Single-Unit Transfer Printing Using SMP	40
4.1.1 Microscale Adhesion Performance	41
4.1.2 Microscale Relief Features Improve Adhesive Reversibility	45
4.1.3 A Resistive Method of Rapid Localized Heating	48
4.2 Multi-Unit Transfer Printing Using SMP	50
4.2.1 Design and Fabrication of Laser-Activated CBSMP Print System	52
4.2.2 Modeling and Characterization.....	55
4.2.3 Printing Demonstrations	63

Chapter 5. Scaling Up Shape Memory Polymer Dry Adhesives.....	67
5.1 SMP as a Reversible Macroscale Dry Adhesive.....	67
5.1.1 Observations Particular to the Sample Geometry.....	69
5.1.2 Demonstrating Adhesive Performance.....	71
5.2 Internally Heated Conductive SMP Dry Adhesives.....	72
5.2.1 Transmission Line Model (TLM) Measurements of Electrical Conductivity	72
5.2.2 A Composite Design for Improved Electrical Heating and Connectivity.....	76
Chapter 6. Alternative Formulations.....	83
Chapter 7. Conclusion.....	89
List of References.....	91
Appendix A. Materials and SMP Property Test Procedures.....	105
A.1 Preparation of NGDE2.....	105
A.2 Preparation of High Molecular Weight SMP Formulations.....	105
A.3 Other Materials.....	106
A.4 Dynamic Mechanical Analysis (DMA) -Based Test Measurements.....	107
A.4.1 Procedure for DMA-based Testing of Chapter 5.....	107
A.4.2 Procedure for DMA-based Testing of Chapter 6.....	108
A.5 Thermogravimetric Analysis.....	108
A.6 Surface Roughness Characterization.....	109
A.7 Work of Adhesion to Silicon Measurement.....	109
A.8 SMP Thermal Expansion Coefficient.....	110
Appendix B. Single Microstamp, Micro-heater, and Ink Structure Fabrication and Performance Test Procedures.....	111
B.1 Microstamp Fabrication.....	111
B.2 Fabrication of Microheaters.....	111
B.3 Adhesion Tests for SMP stamps.....	112
B.4 Assembly of Silicon Inks.....	112
Appendix C. Laser-Activated Stamp Array Fabrication and Performance Test Procedures	114
C.1 Fabrication of SMP stamps.....	114
C.2 Fabrication of Silicon and Gold-Coated Silicon Inks.....	114
C.3 CBSMP Microstructure Absorption Tests.....	115
Appendix D. Large-Area Microtip Fabrication and Performance Test Procedures.....	116

D.1 Microtip Stress Fields and Size Selection	116
D.1.1 Finite Element Modeling	116
D.1.2 The Effect of Air Trapped and Compressed Near Microtips	119
D.2 Silicon Microtip Pattern Molds	120
D.3 Bonding Procedure	120
Appendix E. Conductive CBSMP Fabrication and Performance Test Procedures	121
E.1 CBSMP Blend Preparation	121
E.2 15/30 CB Composite Design	121
Appendix F. Blister Test Procedure and Demonstrative Prototype Fabrication	122
F.1 Blister Adhesion Testing	122
F.2 Practical Adhesive Demonstration	122
Appendix G. Examples of Published Dry Adhesive Performance	123

Chapter 1. Introduction

This dissertation describes a variety of experimental studies and demonstrations exploring the use of shape memory polymers (SMP) as direct-contact dry adhesives. The work is motivated by a study of the mechanics of adhesion, and particularly the importance of controlling elastic compliance which is an ability innate to SMPs. A discussion of alternative dry adhesive designs, both biological and artificial, is provided to give context to the present work's purpose and findings. The remainder of this initial chapter is devoted to first introducing the reader to the existence and importance of adhesive forces in the natural world, and to provide examples of human uses for artificial dry adhesives for which the present work is or may one day be directly applicable.

The size of an animal influences their relationship with adhesion substantially as they navigate the world around them. As relatively large vertebrates, humans move primarily by using the weight of our bodies to produce friction between our feet and the ground below. Climbing smooth surface unaided is impossible, even for more agile species of ape or monkey which can nimbly climb trees by gripping trunks and branches around their circumference. An ant, by contrast, would find this method of climbing a grass blade or the face of your kitchen cabinet wholly unsuitable, while having no trouble walking inverted on even the smoothest surface. The difference is, first and foremost, a matter of physical scale: the ant has far less mass in proportion to its surface area, and thus the surface forces acting upon it are vastly increased relative to its inertial forces. Many arthropods and smaller vertebrates have evolved specialized adhesive systems to take the fullest advantage of this principle, allowing them to deftly move about their natural environment with little regard for the shape or orientation of its surfaces.

The mechanisms by which the adhesive organs of these animals function remained largely elusive until a flurry of research in recent decades has begun to not only fully describe the morphology and properties of the organs, but also a wealth of experimental and theoretical evidence demonstrating the interaction of surface forces and kinetics to produce strong, controllable, and reliable adhesive contact [1]–[6]. The wealth of recent insights has helped to generate interest and hope among researchers that it is possible to develop an artificial dry adhesive system capable of mimicking the best that nature has to offer; a title frequently and deservedly awarded to the adhesive toe pads of the tokay gecko. Having a relatively large body mass for an animal relying on adhesive contact, the gecko is expected to require exceptional

performance and indeed contemporary investigations have proven this to be the case [7]. Detailed investigation of the gecko toe pads reveals a complex hierarchical microstructure, formed of long and branched hairs terminated in sub-micron spatulae. These and other observations indicating that similar structures have independently evolved in many climbing animal species [8] have inspired the development and characterization of a great many artificial dry adhesives.

1.1 Transfer Printing and the Role of Dry Adhesion

As in biological systems, artificial dry adhesives are especially important and often uniquely capable when it comes to performing tasks at very small length scales. The current micromanufacturing industry, responsible for the creation of virtually every modern electronic device and interfacing system, operates through carefully controlled additive and subtractive layer-by-layer processes. This approach to manufacturing allows for the manufacture of many small, planar structures in parallel, and thus has been well suited to the production of current and past generations of microcircuitry. Nonetheless, serious challenges exist when attempting to produce devices with significant depth (three-dimensional devices) and particularly when many dissimilar layers and materials are required. Chemical and physical etch and deposition processes have a complex often deleterious range of effects on previously-processed features, seriously limiting compatibility between materials in a single device. The complexity and corresponding expense of process design thus generally increases exponentially with device complexity.

A possible solution to this limitation is to separately fabricate the constituent pieces of a device as process compatibility allows, thereby making each simple to produce, and to then combine them together to form the final product. Though a straightforward task when applied to the assembly of large computer components, assembling the microscopic components of their chips in this way is not so. The reason is again the vanishing of mass and corresponding inertial forces in proportion to surface forces. Transfer printing describes a collection of processes which are intended to overcome this challenge by using smart control of surface forces, particularly adhesive forces, to transfer and assemble, or print, very small objects herein referred to collectively as inks. In nearly all likely applications, the integrity and cleanliness of the inks are crucial and thus wet adhesives which utilize transferrable glue layers and other processes which leave residues are undesirable. Instead, the working surface which effects the

transfer, referred to as the "stamp," is comprised of a dry adhesive which may dynamically change effective adhesive strength through control of elastic and dissipative processes at their surface, leaving little or no residual material behind. These aspects are explained more fully in the following chapters.

1.2 Other Current and Potential Artificial Dry Adhesive Applications

Though the study of dry adhesives is a relatively young field, successful designs have many potential applications at home and in industry, both mundane and exotic. A particular feature of dry adhesives which makes them potentially desirable for many applications is their reusability; since no material is transferred or expended in the process of forming and breaking an adhesive bond, it is repeatable. This quality makes them well suited for applications in outer space, where discarding supplies is to be strongly avoided, suction devices are unusable due to the vacuum environment, and non-ferrous spacecraft construction precludes magnetic attachment [9]. Several works have demonstrated dry adhesives which work well in high vacuum and over large temperature fluctuations experienced on the exteriors of spacecraft [9]–[13], and prototype climbing robots for space applications utilizing dry adhesion have been developed [14]. Many near-term earthbound applications exist as well, including the biomedical field where work is being done adapting the technology for wearable sensors [15] and surgical tool grips [16]. Household applications, including reusable wall-hangings and tapes, children's toys, non-slip surfaces for kitchens, bathrooms, automobiles and more seem likely next steps for dry adhesive technology to take hold. In the meantime, researchers continue working to develop wall-climbing robots [17]–[22], and even human-scale devices [23], [24], which could eventually have a variety of important applications, including helping emergency workers to find and rescue disaster victims, allowing military forces to scout buildings and other locations with greater ease and safety, or by simply giving building maintenance workers a means of inspecting heating ducts and other critical systems. The usefulness of small unmanned aerial vehicles (UAVs) for many of these same tasks is significantly impacted by their typically short flight times. Researchers are working to develop effective dry adhesives which will allow UAVs to perch on walls or other surfaces to conserve energy while observing or awaiting instruction [25]–[27]. The following chapters elaborate on the challenges researchers currently face and recent progress made in our attempts to bring dry adhesive solutions to these varied applications.

Chapter 2. Dry Adhesive Design and Characterization

The adhesive performance of two mating surfaces depends on many factors including their morphology, chemical makeup, cleanliness, loading conditions and environmental factors including temperature, light, humidity and the presence or absence of a surrounding fluid. The term performance, additionally, may describe a variety of characteristics of the adhesive pairing including failure stress for a particular set of loading conditions, work of adhesion, durability, and the ease of release in the case of reversible adhesives. In this section, I first consider the qualities which make for a desirable dry adhesive, and briefly discuss the fundamentals of how these qualities are achieved in practice. Observations from the natural world teach and reinforce the concepts of basic dry adhesion mechanics, guiding researchers first towards biomimetic surface patterning and fibrillar designs. Examples of alternative designs, generally intended to use the lessons of compliance control to create simpler but effective dry adhesives, are provided towards the end of the section.

2.1 Desirable Properties for Dry Adhesive Systems

Liquid adhesives and pressure sensitive adhesives (PSAs) are ubiquitous in modern society. The fundamental difference in function between the more common artificial liquid and PSAs, and a typical dry adhesive, is the reusable and releasable nature of the dry adhesive. While a liquid adhesive or a PSA cures or flows to bond two surfaces together permanently (or at the very least, cannot be reused with the same performance should the surfaces be later separated), a dry adhesive is intended to create a nondestructive temporary bond which may be undone and repeated many times without prohibitively degrading its adhesive performance between bond cycles.

2.1.1 Strong and Reversible Adhesion

A useful dry adhesive must, first and foremost, be capable of generating a bond of adequate strength to its adherend for its intended application, in what we may refer to as the dry adhesive's "adhesion on" configuration. The strength of an adhesive bond is typically measured either in terms of its load bearing capacity at failure, or in terms of the energy dissipated during the separation of adhesive and adherend. This measured "maximum" adhesive strength of a dry adhesive bond will vary depending on many factors regarding both adhesive and adherend, but is typically several orders of magnitude below that

of a comparably sized “wet” adhesive bond, which may support loads well in excess of 1 kN cm^{-2} [28]. Nonetheless, dry adhesives are capable of generating adequate strength for low and moderate load situations, particularly when bond area may be increased.

The weaker bond of a dry adhesive is the price paid for its reusability, and corresponding ability to detach non-destructively from its adherend. Though less strong than permanent bond methods, detachment through a dry adhesive’s primary loading path is usually prohibitively difficult. Therefore, the design of a useful dry adhesive will include a method of facile detachment; the detachment method typically involves altering the load path and failure mode of the interface, or in the case of more recent dry adhesives created with “smart”, stimuli-responsive materials, the detachment is facilitated by a stimulus-assisted change in the adhesive’s material properties or morphology. When loaded or otherwise prepared in this way for easy detachment, we say the dry adhesive is in its “adhesion off” configuration, and the measured resistance to detachment may be called the adhesive’s “minimum” adhesion. As with the maximum adhesion, the minimum adhesion achieved by a dry adhesive varies greatly with the design of the adhesive and the properties of the adherend.

The ratio of maximum to minimum adhesion will be referred to as the adhesive’s “reversibility”, and is an important metric for dry adhesive design, particularly for very small-scale applications where surface forces dominate inertial forces, and for applications where speed and efficiency are of significant importance such as the motility of certain animals and robots. A climbing insect possessing footpads with poor adhesive reversibility, for example, would find locomotion to be challenging: either because the maximum adhesion would be too poor to allow adequate traction, or the minimum adhesion too great to allow for timely and versatile detachment of individual foot pads.

2.1.2 High Adhesion to Preload Ratio

It is generally desirable to minimize the necessary compressive force between adhesive and adherend necessary to create a strong bond. The ratio of an adhesive’s maximum adhesive force to the corresponding force, or preload, required to form the bond, is herein referred to as its adhesion to preload ratio. Though often given little attention in current artificial dry adhesive research, it is of great importance for most practical applications. A lizard attempting to climb a wall would tire quickly having

to exert itself against the wall with each step. Likewise, a person wishing to hang a television on their wall with a dry adhesive mount would rather not have to apply a force comparable with their television's weight against the wall, and a manufacturer utilizing dry adhesives to manipulate delicate structures will value a low-preload process both to protect their products and boost efficiency. In the ideal case, a dry adhesive will generate its full adhesive strength passively upon contact with its adherend.

2.1.3 Durability

A reusable dry adhesive must have a durable adhesive surface which is resistant to damage and fouling, each of which can degrade performance substantially. An adhesive surface often experiences significant cyclic stress and corresponding strain during a loading and unloading cycle, often in shifting and perhaps unpredictable directions requiring that the materials and surface structuring work together to form a mechanically robust surface. Fouling by means of particulate contamination is a significant concern for any reusable adhesive. It must be expected that the surface of any adherend will contain some particle debris which may be transferred to the adhesive. The challenge is to design the adhesive such that it will adhere to the adherend, but resist collecting particles, or having collected the particles the surface will remove them within a few attach and detach cycles or by flowing liquid or capillary action, a characteristic and process often referred to as “self-cleaning” [29]–[33]. The issue of surface fouling is particularly challenging and restricts the use of most current artificial dry adhesives to use with very clean adherends, lest their performance undergo substantial degradation.

2.2 Performance Metrics

The question of how to best measure a dry adhesive's performance is not a trivial one. In Section 2.1, I discussed several important desirable qualities which a practical dry adhesive should possess, namely controllable adhesion, high adhesion to preload ratio, and durability. Measuring how well a dry adhesive achieves these goals, however, is subject to significant variability between different researchers and different adhesive designs. In this section, the challenges of quantifying and comparing dry adhesive performance are discussed and examples of the most common test methods are provided.

The strength of an adhesive bond takes considerable effort to thoroughly quantify. Researchers investigating fundamental dry adhesive physics will generally employ more rigorous testing methods

than those primarily reporting novel fabrication techniques, but regardless of the primary motivation all authors seeking to produce useful quantification of their adhesive's performance face steep challenges. However, the term "strength" can vary remarkably in its interpretation depending upon the type of adhesive, the expected application, and the equipment and techniques available to the researchers. One may broadly classify adhesive strength measurements into ones of normal force, shear force, and work of adhesion. In this case, the work of adhesion should not be confused with the thermodynamic work of adhesion, but rather the actual energy required to separate two surfaces including dissipative effects. However, as alluded to in Section 2.4, the magnitude of force one may expect to measure from a given adhesive interface is strongly influenced by many factors, including the adhesive's size, apparatus geometry, load distribution, loading rate, ambient temperature and humidity, and the adherend's material composition, geometry, roughness and cleanliness. It is not unusual for even the same researcher performing identical tests twice to get dramatically different results, and thus quality results demand multiple tests at each condition to give statistically meaningful results.

The presence of normal forces to separate two surfaces is, in most cases, unambiguously caused by adhesive attraction. Most artificial dry adhesives are designed to rely on van der Waals interactions to generate the bulk of this force, although capillary contributions and even mechanical interlocking may play a significant role in some. There are relatively straightforward methods to obtain a quantifiable measure of normal adhesive force at many various length scales, though these different methods should not be assumed to provide directly comparable results. Shear adhesion is somewhat more challenging to measure without applying unwanted interfacial moments and normal forces, subject to the available test apparatus and adhesive geometry. Shear forces at an interface are sometimes described as a friction force, implying that maintaining a compressive normal force is necessary to support the shearing load and also suggesting that the amount of shearing load supported should scale positively with the applied compressive force. In either case, it is frequently shear strength that is of more relevance for dry adhesives used in locomotion both in nature and for artificial robotics. For this reason and others particular to the adhesive geometry and expected application, many dry adhesives are tested exclusively or primarily by quantifying shear force.

Whether reporting shear or normal forces, the reported force is generally the peak force at which uncontrolled failure occurs at the adhesive interface, and is commonly converted to a stress by dividing the force by adhesive area. The conversion of a force to a stress implies a linear relationship between adhesive area and failure load that is nearly always misleading. One can expect with confidence that, for a given set of environmental and loading conditions, adhesive stress as measured in this way will decrease with increasing adhesive area. The source of this relationship is two-fold: due to surface roughness, contaminants, and other defects, the proportion of the adhesive able to make intimate contact with the substrate generally decreases with increasing area, and it becomes increasingly challenging to uniformly distribute the load across the whole of the adhesive interface. Researchers often seek to improve the generality of their results by instead calculating work of adhesion, which when calculated properly will provide a quantifiable value which, in most cases, will better describe the inherent strength and stability of an adhesive interface for comparison across studies. Work of adhesion in this context is a measure of the energy dissipated by separating a unit area of the adhesive/adherend interface, as described in Section 2.4. It is commonly provided in units of J m^{-2} in the case of strong adhesives, and mJ m^{-2} for relatively weaker interfaces. Similar to fracture in solids, where a hard and unyielding material has far lower critical energy release rate than those able to deform and stretch, a tough dry adhesive interface is generally the product of a compliant and deformable adhesive and a strong adhesive may possess a fracture energy of several hundred J m^{-2} against a favorable adherend.

Other measures of performance, notably reversibility and durability, are often given only passing consideration in novel studies. For systems designed with reversibility in mind, the method of initiating adhesive reversal may vary significantly. Fibrillar structures most often rely on an adhesive directionality granted by the fiber orientation. Thus, the reversibility relies on a supporting structure capable of adequate motility to “pull” to adhere and “push” to detach. Even within this class of reversible adhesives, significant differences can exist between the necessary angles and magnitude of shear motion which must be achieved to create the best-case circumstances likely reported. Other researchers will claim reversibility simply by changing the location at which load is applied; an adhesive may offer tremendous shear strength but offer little resistance to peeling if a normal force is applied to one edge. Thus, when reporting and discussing reversibility, one must keep in mind the challenges and

individual level of interpretation which may go into a reported value. A recent article promotes the concept of a so-called “adhesion circle” method of measuring directionally variable dry adhesives, to characterize adhesive strength and reversibility in a more thorough and standardized way [34]. Despite the importance of durability for many dry adhesive applications including their use in robotics [35], it is frequently a low priority in fibrillar adhesive studies, which one may rightly suspect is related to the adhesives’ susceptibility to failure. Nonetheless, many researchers make a point of measuring adhesive performance over the course of several adhesive attachment and detachment cycles, though variations exist with regard to the particular source of performance degradation the researchers are measuring. Fibrillar structures in particular are subject to failure through various failure methods outlined in Section 3.2, but may also be subject to the issue of particulate fouling common to all dry adhesives. Except for adhesives specifically designed with self-cleaning or fouling resistance in mind, adhesive durability is virtually always tested against immaculately clean adherends and thus may provide results which are misleading for real world applications.

2.3 Test Methods

The method of testing the strength of a dry adhesive fundamentally involves stressing the interface to the limit at which the interface slips or separates and recording the relevant data. The specifics of the method chosen will depend upon the type and scale of the dry adhesive, the type and thoroughness of data sought by the investigation, and the equipment and expertise available to the researchers. Quantification of the adhesive strength is, in nearly all cases, performed by measuring force in a single linear direction at a time, although repeat tests may be performed to quantify performance for multiple directions relative to the adhesive interface. However, there has been recent work by researchers to develop more sophisticated mechanisms capable of sensing forces in multiple planes simultaneously at length scales and force magnitudes appropriate for many dry adhesive applications, potentially simplifying and enriching the process of data collection [36]. These sensors may be particularly important for the development of robots which utilize dry adhesives, where they are expected to enable real-time feedback to inform the robots’ motion [37]. It is additionally possible to collect valuable information from adhesive tests through the use of high resolution tactile sensors, which provide a two-dimensional map of force versus position across an adhesive interface [38].

When stressing the adhesive interface, the source of the applied load will generally be either a free-hanging weight, or a motorized or otherwise automated apparatus. Methods employing free-hanging weights are frequently chosen for their advantage of being a very low-cost testing method which is quick to implement, particularly when only a relatively small number of test cycles is needed, or when visual demonstrations are desired. Relatively large ($>1 \text{ cm}^2$) or highly adhesive samples are most suitable due to the need for researchers to directly handle the specimens and often to manually apply the weights to the system. Shear and normal adhesion are each relatively simple to measure in this way by orienting the adhesive interface appropriately [39], though most studies report just one or the other. Adding weight continuously via a liquid pump has the advantage of gradually increasing load at a steady rate, thus improving measurement precision. A number of researchers have chosen to characterize the shear strength of their fibrillar dry adhesives through either directly hanging weights [40]–[44], or by manual application of force using a spring scale for measurement [45]. A notable shortcoming of these methods is that only measurable quantity of relevance will be the force that occurs at the point of unstable interfacial failure. The lack of electronic force and displacement monitoring precludes more detailed data collection. However, in the absence of a complete set of force and displacement data, work of adhesion may still be possible to estimate using principles of fracture mechanics by making certain measurements or assumptions regarding the crack geometry. An interesting variation of this technique involves rolling a weighted cylinder coated in a dry adhesive surface down a slope, and using its rate of descent to estimate relevant adhesive properties [46].

Electronically controlled and actuated test apparatuses have a number of appealing features, and are very commonly used for quantitative studies of dry adhesive performance. Test conditions such as preload and loading rate are simple to control with most schemes, allowing researchers to apply a continuously increasing load. Force and displacement data are typically simple to collect with load cells and position sensors respectively, allowing in many cases for a direct calculation of energy dissipation from test data [5], [47]. Electronic control allows tests where displacement, rather than force, is controlled. Displacement controlled tests can offer a variety of investigative benefits for researchers, including the ability to observe crack growth behavior which would be difficult with unstable force controlled methods [48]. Interfacial adhesion is often tested in such setups using a cantilevered

arrangement, where the adherend is flexed to allow an interfacial crack to propagate [48], [49]. Atomic force microscopes (AFM), though not designed with dry adhesive research in mind, are frequently used by dry adhesive researchers in the testing of normal adhesive strength in very small and localized sample regions due to their electronic control and precise force-sensing capabilities. The method is most common with nanofibrillar dry adhesives [42], [50]–[52], though it was also notably used to measure the adhesive force of a gecko setae. [53] Similar microscale equipment, such as micro- and nano-indenters, are sometimes used [54], [55]. Investigators with much larger adhesive samples often choose material tensile testers, including various tensile testers [56]–[64], which like AFMs are pre-existing platforms capable of applying and measuring forces in a repeatable and easily-controlled manner. For those wishing to measure forces for adhesive areas either too large for AFM study, or too small or weak for material tensile testers, the options are somewhat more limited and frequently require the construction of custom test apparatuses. The most commonly used form involves a motorized stage moveable normal to the adhesive surface, and possessing a smooth, spherical or semi-spherical adherend [47], [65]–[71]. Measurements of shearing strength are likewise possible [70], [72]. For both shear and normal adhesion experiments, spherical adherends are frequently used to avoid potential misalignment issues which may occur with imperfectly oriented flat surfaces, thus intending to improve test consistency. Custom test equipment with flat adherends are nonetheless also used in many investigations of normal adhesive strength [73]–[77].

2.4 Fundamental Concepts for Creating a Dry Adhesive System

All dry adhesive systems must obey the same set of physics. The performance requirements of each system dictate the particulars of its design. This section summarizes the current understanding of the relevant design principles identified by researchers for reversible dry attachment to surfaces with varied surface chemistry and morphology.

2.4.1 Attractive Forces

An attractive force between two surfaces may be effected through numerous mechanisms including mechanical interlocking; long-range electrostatic interactions; short-range electrostatic interactions (van der Waals forces, hydrogen bonds); molecular bonding (ionic, covalent, metallic); magnetic forces;

capillary forces; and the Casimir–Polder force. Though among the weakest of these in terms of the maximum potential attractive force, the van der Waals forces are most frequently the dominant contributor to the performance of dry adhesive systems [1], [78]–[81]. The van der Waals forces arise from very short range (3–7 Å) [82] interactions between permanent and induced molecular dipoles, comprised of the Keesom, Debye, and London dispersion forces [83]. The forces arise spontaneously when two surfaces are brought into contact and are ubiquitous, occurring with varying extent for all neighboring molecules and mostly independent of other environmental factors. This means that a dry adhesive relying on van der Waals forces should be expected to perform similarly with chemically diverse adherends and with little intrinsic effect from temperature, pressure, humidity or external electromagnetic fields [84]. The relative weakness of the bonds may, in fact, be considered an advantage for a reversible dry adhesive because it allows for faster and more efficient detachment with virtually non-existent surface damage or fouling to either adhesive or adherend, each maintaining surface mechanical integrity through their much stronger covalent or ionic bonds.

The bond between two materials is frequently thought of and described in terms of surface energies. It is energetically favorable for solid materials to minimize their free surface area due to the summation of internal short range molecular forces, and the energy required to create the free surface is denoted γ (units of N m^{-1}). Two free surfaces, designated a and b , brought into contact will then require work to separate, referred to as their thermodynamic work of adhesion W_{ab} . The work of adhesion between surfaces a and b is related to their individual surface energies, and interfacial energy γ_{ab} , as [85]:

$$W_{ab} = \gamma_a + \gamma_b - \gamma_{ab} \quad \text{Eq. 2.1}$$

The value of γ_{ab} is possible to estimate using the work of Girifalco and Good as [86]:

$$\gamma_{ab} = \gamma_a + \gamma_b - 2\sqrt{\gamma_a\gamma_b} \quad \text{Eq. 2.2}$$

Combining Equations 2.1 and 2.2 gives the result that $W_{ab} \approx 2\sqrt{\gamma_a\gamma_b}$, which for the case of cleaving a single uniform material to create two new surfaces gives the sensible result that $W \approx 2\gamma$. In the case of strong covalent or ionic bonds, it may be expected that $2\gamma \approx 2 \text{ N m}^{-1}$ [87]. For van der Waals forces, those which dominate in the case of dry adhesion, a more typical value is $2\gamma \approx 0.05 \text{ N m}^{-1}$ [88]. A small number of artificial dry adhesive systems have been developed to enhance performance using long-

range electrostatic forces with high voltage power sources [89]–[93] as a supplement to van der Waals forces. Capillary forces are more often a significant or suspected contributor to adhesion, particularly for biological systems adapted to function in wet or humid environments [1], [53], [94]–[98]. However, cases where the presence of a liquid layer and meniscus are confirmed to be substantially important for the functioning of a reusable adhesive surface are still somewhat uncommon.

2.4.2 Controlling Elastic Energy

The short range of van der Waals interactions requires molecules to be essentially “touching”, in the molecular sense to generate an appreciable adhesive force between them. The sum of the van der Waals attractive force between two objects will scale with the intimate contact area between them, as proportionally more molecules are brought close enough to attract each other. Increasing this sub-nanometer contact is a basic goal for the design of a dry adhesive system when more adhesive strength is required, and adhesive strengths are frequently reported on a per-area basis with the rough assumption that adhesive strength will scale linearly with adhesive area. Classical contact mechanics, as developed by Heinrich Hertz, describes the contact between a spherical elastic body and an elastic half-space in terms of the compressive force between them F , the sphere radius R , contact radius a , and the system’s effective modulus E^* , which is a function of each material’s elastic modulus and Poisson ratio:

$$a^3 = 3FR/4E^* \quad \text{Eq. 2.3}$$

The Hertzian model accounts for the elastic restoring forces within the bodies to resist a compressive load, however the attractive surface forces are disregarded. An expanded model of elastic contact accounting for surface forces was put forth by Johnson, Kendall, and Roberts, and is consequently referred to as the JKR model of elastic contact [78]. The inclusion of the thermodynamic work of adhesion γ modifies the Hertzian equation as follows:

$$a^3 = \frac{3R}{4E^*} \left(F + 3\gamma\pi R + \sqrt{6\gamma\pi RF + (3\gamma\pi R)^2} \right) \quad \text{Eq. 2.4}$$

Attractive surface forces expand the contact area, as depicted in Figure 2.1a. The physics described by this relation has great significance for adhesive performance since real surfaces are seldom atomistically flat, but are instead rough, covered with asperities which inhibit contact. The asperities are analogous

to the elastic sphere compressed against the opposing half-space. For a given work of adhesion, typically in the range of 50 mJ m^{-2} , it is apparent that soft materials are necessary for conformal contact to occur. The reduced restoring force of the softer interface allows attractive surface forces to dominate, and the materials to deform and “flow” around asperities to increase surface area and therefore adhesion. In the common case of a rigid adherend, it is the duty of the adhesive to undergo the majority of this deformation (see Figure 2.1b), and an adhesive which performs this task adequately is referred to as being sticky, or in more technical terms as having “tack” [99], [100].

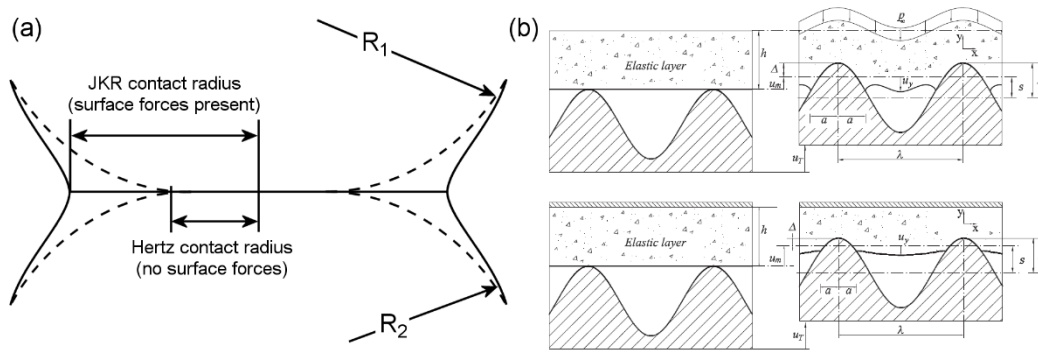


Figure 2.1 (a) The contact between two convex elastic bodies of radii R_1 and R_2 under a compressive normal load in the presence and absence of surface forces. (b) Elastic layers in contact with a rough or wavy surface assuming the layer is free (top) or confined (bottom) (reproduced with permission from [101]; published by Elsevier, 2016).

A tacky adhesive is one which, immediately upon contacting an adherend, will require a significant force to separate. A common rule of thumb for pressure sensitive adhesives (PSAs) is the Dahlquist Criterion, suggested by Carl Dahlquist in 1969, which roughly states that the elastic modulus must be below $3 \times 10^5 \text{ Pa}$ to exhibit tack against common surfaces. The exact value depends upon the nature and roughness of both the adhesive and the adherend. For a somewhat idealized surface modeled as a regular series of bumps with radius R and height $2h$, the critical elastic modulus E_c for a material to exhibit tack can be calculated as [102]:

$$E_c = W\sqrt{R/h^3} \quad \text{Eq. 2.5}$$

where W is the thermodynamic work of adhesion. In certain cases where this criterion is not strictly met, conformal contact may still be achieved through the application of compressive force, or preload,

to unite the two surfaces. Enhancing the compliance of an adhesive is not entirely “free” in terms of performance, however. Adhesive interfaces are strongest when loaded evenly, i.e., when the stress is well distributed. Compliant adhesive structures are less able to resist deformation, and therefore more susceptible to concentrated stresses [73], for example when peeled. Excessive strains reduce mechanical durability, and the tacky surface of a low-modulus adhesive is more susceptible to fouling through particle contamination.

A possible solution to the challenges of adhering to rough surfaces while minimizing the negative impact of excessively low modulus comes in the way of surface structuring. Researchers have long been aware that many small climbing animals and insects have evolved adhesive organs with complex morphology. In particular, their surfaces are frequently coated with relatively slender fibers or hairs, broadly referred to as fibrillar surfaces. Recent research has shed light on the mechanisms by which fibrillar structures enhance adhesion, and many attempts of artificial mimicry have been made. A well-established benefit of fibrillar surfaces is their enhanced surface compliance and ability to conform to a rough adherend even when composed of a relatively high-modulus material. Individual micro- and nano-scale fibers may bend and buckle, reaching past adherend asperities to contact the microscopic valleys between, as shown in Figure 2.2a. Fibers which are adequately long and flexible can form a similar level of contact quality for smooth and rough surfaces alike (Figure 2.2b). The JKR and similar models for adhesive contact additionally indicate that even for a flat and smooth adherend, a dense array of small contact points will provide better adhesion than a few larger contact points due to the reduction in the elastic deformation necessary to create a given contact area. The principle of increasing the

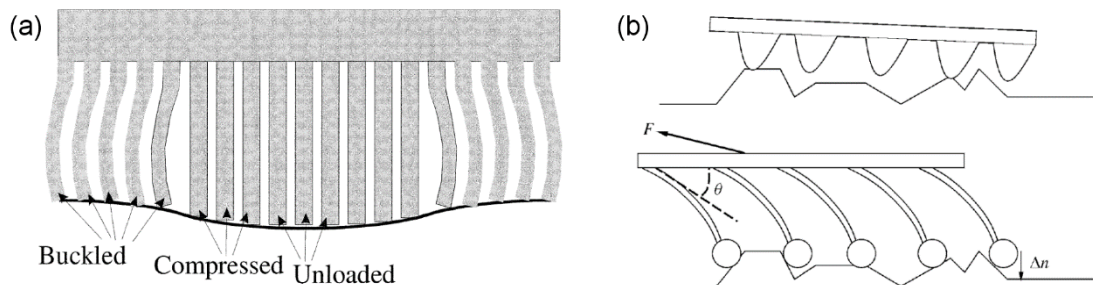


Figure 2.2 (a) Fibrillar surface loaded in compression against a rough or uneven surface (reproduced with permission from [103]; published by Oxford Academic, 2002). (b) Comparison between the conformal ability of low aspect ratio nanobumps and longer, more flexible nanohairs (reproduced with permission from [104]; published by Taylor and Francis, 2003).

number of contact points to enhance dry adhesive performance is well-established and referred to as contact splitting [105], though the extent to which contact splitting directly enhances fibrillar adhesion is not entirely clear [106].

Regardless of the method of forming an adhesive interface, a designer is naturally interested in understanding how its morphology affects its strength and performance during use. Fracture mechanics consists of a set of methods to predict the onset and propagation of cracks, considering both solid mechanics and surface forces [87], [107], [108]. Initially developed by Griffith to investigate brittle failure in homogeneous materials, and later expanded by Irwin and then Rice to include the effects of plastic dissipation as depicted in Figure 2.3a, it may easily be adapted to describe many adhesive interfaces. A typical linear analysis will first assume a material or adhesive interface possesses a pre-existing crack. Crack advance is determined by an energy balance comparing, for an infinitesimal advance of the crack, the energy release rate to the critical energy necessary to separate the surfaces, or “work of adhesion.” The energy release rate is the summation of the rate of change of internal strain energy and the work done by tractions on the system boundaries. If the energy released exceeds the energy required to create the new surfaces, then the crack will advance. Irwin’s treatment developed the concept of the crack stress intensity factor, K , which is calculated separately for each of three modes of failure as a function of the system’s geometry and loading conditions: Mode I tensile opening, Mode II in-plane shear, and Mode III out-of-plane shear. The values of K are calculated from the stress field near to the crack tip for Mode i :

$$K_i = \lim_{r \rightarrow 0} \sqrt{2\pi r} \sigma_{jk}(r, 0) \quad \text{Eq. 2.6}$$

where the subscripts j and k are placeholders describing relevant stress plane. The solution of Equation 2.6 gives a result for Mode I loading typically of the form:

$$K_I = C\sigma\sqrt{\pi a} \quad \text{Eq. 2.7}$$

where C is a constant particular to the crack geometry and loading conditions, a is the crack length, and σ is the applied tensile stress far from the crack. It is evident that longer cracks significantly increase the stress intensity factor, and therefore decrease the expected failure strength of the material or

interface. Modes I and II are most frequently dominant for adhesive interfaces, and are related to the energy release rate G as follows (plane strain):

$$G_i = \frac{(1 - \nu^2)}{E} K_i^2 \quad \text{Eq. 2.8}$$

where the material's elastic modulus E and Poisson's ratio ν are included. Using work of adhesion W_a as the failure criterion, where failure is predicted when $W_a < G$, it is apparent from Equation 2.8 that a greater elastic modulus should be expected to increase the adhesive's strength assuming that it is capable of forming intimate conformal contact to its adherend.

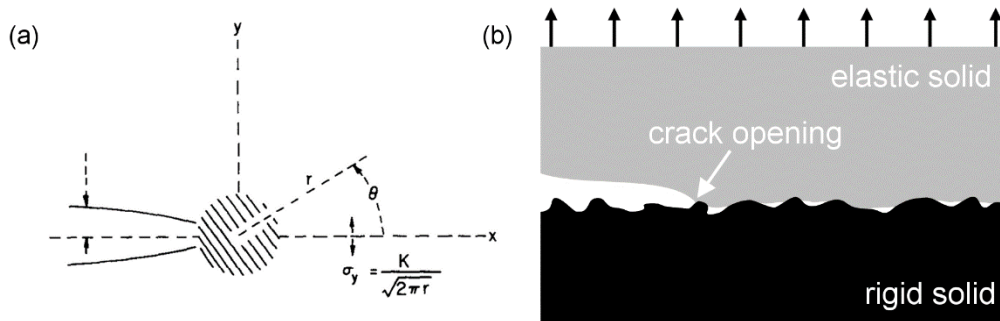


Figure 2.3 (a) Schematic view of the leading edge of a crack in an elastic body (reproduced with permission from [109]; published by Elsevier, 1968). (b) An opening of a crack in an adhesive interface during pull-off.

The approach above can provide useful predictive power for the strength of adhesive interfaces which meet the assumptions inherent in linear fracture mechanics. Its application can be less meaningful for non-ideal interfaces where an interface cannot be assumed continuous and homogeneous, such as the one shown in Figure 2.3b. A more general and simple framework to guide the mechanical design of dry adhesives is desirable. One such relation has been developed recently by Bartlett et al. using a simplified energy balance for an elastic body of arbitrary shape, assuming unstable interfacial separation will occur at a critical force F_c [56]. The critical force is proportional to interfacial surface area A , compliance C , and interfacial critical energy release rate G_c as:

$$F_c \sim \sqrt{G_c} \sqrt{A/C} \quad \text{Eq. 2.9}$$

The researchers experimentally tested their own composite adhesives comprising a variation of four orders of magnitude of $\sqrt{A/C}$, demonstrating general agreement with Equation 2.9 for bonds to a smooth adherend. Additional evidence indicating the broad applicability of this simple relation has been provided by subsequent experimental work [58], [61], [63], including an investigation for the relation's applicability for rough adherends where it was concluded that even subtle surface roughness dramatically impacts the expected adhesion due to elastic restoring forces, particularly for rigid adhesives [62]. The work highlights the importance of compliance control in a dry adhesive system, and reinforces that superior performance may be expected for an adhesive capable of displaying large compliance when conforming to an adherend, while remaining inextensible when loaded.

2.4.3 Enhancing Work of Adhesion Through Energy Dissipation and Absorption

The work of adhesion for a strong adhesive is on the order of 100–1000 J m⁻². This value is notably much larger than the thermodynamic work of adhesion for typical material pairs (~100 mJ m⁻²) and even much greater than ionic or covalent bond energies (~2 J m⁻²). The source of this discrepancy, and methods to enhance it, have been the subject of considerable research.

It has long been observed that the cohesive bond strength, or tear resistance, of rubbers is significantly greater than what should be predicted by the energy of their covalent bonds alone [110], [111]. Rubber and other polymeric materials are formed of covalently-bonded molecular chains which can move relative to each other under load, and in the process dissipate energy. The materials are described as viscoelastic, meaning they exhibit both reversible elastic and irreversible viscous responses when undergoing deformation. The molecular arrangement of a crack forming in a crystalline material is compared with that of a polymer in Figure 2.4, showing the less-ordered arrangement of polymer chains bridging the crack front. Viscous energy dissipation and crack-tip phenomena (crazing, blunting) have been identified as the primary causes of the impressive tear resistance in many soft polymers [88], [112]–[114]. Crack blunting is significant when a polymer's cohesive strength matches or exceeds its elastic modulus, and is the result of large nonlinear elastic deformations which act to reduce the stress at the crack tip [88]. Lake and Thomas posited that for the crack to advance, each polymer chain bridging the crack path must be broken, though for a single bond to be broken the entire chain must be stretched to near its breaking point [110]. The energy required to stretch the chain is then dissipated,

rather than elastically returned to the bulk material, thus enhancing the material's fracture strength. This is also thought to occur in the case where, instead of breaking, a polymer chain bridging the original fracture plane slides or “pulls-out” from the opposing side, as shown in Figure 2.4c [115]. Bulk viscoelastic processes dissipate energy throughout the material as it is loaded, the effect being especially pronounced for a polymeric material near its glass transition temperature and with relatively little molecular crosslinking [116], [117]. These internal molecular processes likewise serve to enhance the work of adhesion for an adhesive interface between a polymer and its adherend [111], [118], [119].

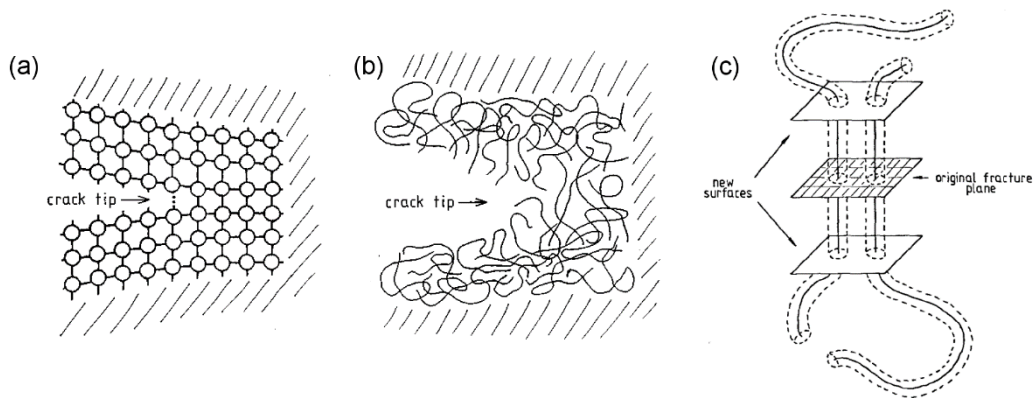


Figure 2.4 (a) A crack in a brittle atomic crystal, and (b) a crack in a brittle polymer (reproduced with permission from [120]; published by the American Institute of Physics, 1999). (C) Schematic representation of the “pull-out” process occurring during crack propagation within a polymer (reproduced with permission from [115]; published by Springer, 1985).

Researchers have additionally identified certain forms of surface geometry or structuring which enhance energy dissipation, and therefore adhesive strength. Chief among these are the fibrillar structures frequently found on climbing animals in nature, which have been suggested to dissipate energy in a process analogous to the molecular stretching of polymeric chains; an individual fiber will bend and elongate until its contact with the adherend breaks, at which point the energy invested in deforming the fiber is dissipated inelastically rather than returned to the bulk material [103], [119]. The smaller and more numerous contact points of a fibrillar adhesive enjoy the additional benefit of minimizing the crack length at each interface [6]. The benefit of this from a fracture mechanics standpoint is apparent from Equation 2.7. It has additionally been shown that inhomogeneous or partitioned surfaces can enhance the adhesive performance of thin films, in particular the interfacial fracture toughness [48], [121]. The incisions create many internal cracks which act as defects to disrupt and deflect the

continuous crack propagation which occurs in a smooth film, as depicted in Figure 2.5a. The thickness of the film was found to play a role, with thicker films producing greater energy dissipation as the taller segments are stretched further prior to delamination, and thus absorb and dissipate more elastic energy (Figure 2.5b). Engineering an adhesive surface such that energetic barriers to crack propagation exist is frequently referred to as “crack trapping”, and many researchers have used it to their advantage in the creation of film-terminated fibrillar dry adhesive surfaces (Figure 2.5c–e) [76], [122]–[126]. The fibrillar structure supporting the smooth film surface creates “trap” regions between the fibers where the film absorbs energy which would otherwise be applied toward crack propagation. Further separation may only occur as the stress beneath the fibers increase enough to spontaneously form new cracks, a circumstance requiring substantially more force and energy than for a corresponding flat and unstructured surface. Figure 2.5e depicts the situation in which separation between adhesive and

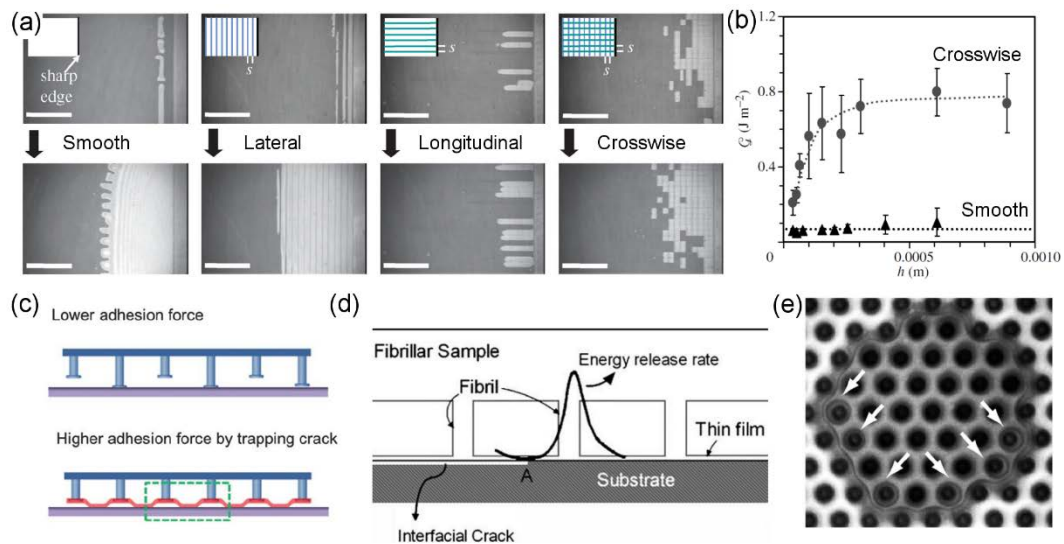


Figure 2.5 (a) The effect of discontinuities on interfacial crack propagation using differently incised polydimethylsiloxane (PDMS) films, and (b) the relationship between fracture energy and film thickness for smooth and crosswise incised films (reproduced with permission from [48]; published by Royal Society, 2005). (c) Illustrations of crack trapping for a film-terminated fibrillar adhesive pulled normal to the adherend (reproduced with permission from [76]; published by Royal Society of Chemistry, 2013), and (d) showing how the energy release rate varies depending upon the position of the crack front (reproduced with permission from [126]; published by Royal Society of Chemistry, 2008). (e) An optical image of a film-terminated fibrillar adhesive delaminating from an adherend, showing interfacial cavitation under several fibers (reproduced with permission from [122]; published by the National Academy of Sciences, 2007).

adherend occurs spontaneously below fibers rather than by continuous crack propagation between fibers.

Chapter 3. Existing Strategies for Creating a Successful Dry Adhesive

3.1 Observations of Natural Systems

It is common knowledge that insects, many frogs, and small lizards are impressively skilled at climbing on all manner of surfaces and in all orientations. These animals possess adhesive pads on their toes or legs which are capable of adhering to the surfaces in their natural environment, and just as importantly, are capable of detaching with relative ease. The sequential attachment, loading, and detachment are essential to effect locomotion. Modern investigation has determined that although no two species may possess exactly the same attachment organs, there are substantial similarities in form and function even between evolutionarily very distinct animals. The form of adhesive pads can generally be described as either smooth or hairy.

Smooth, when referring to adhesive organs, is a rather loosely used term because the organs often have some low-aspect ratio micro-scale structuring to them. Animals possessing smooth pads include crickets [2], [127], ants [3], [97], bees [3], [128], cockroaches [129]–[131], stick insects [132], aphids [4], [133], and tree frogs [134]–[137]. It is frequently unclear for biological systems to what extent the adhesion is truly “dry”, particularly in the case of smooth attachment pads. Many insects secrete emulsions such that the pads are continually coated in a wet or oily substance. Study of stick insects has determined that a substantial portion, perhaps the majority, of their adhesive strength from emulsions with non-Newtonian properties to resist shear forces [132]. At least some species of aphids, which spend a great deal of their time walking along the wet and humid surface of leaves, rely primarily on surface tension of expelled fluid on their adhesive pads to scale smooth surfaces [4]. When scaling rough surfaces, they may eschew use of their adhesive pads altogether in favor of clinging with claws [133], a trait shared by insects of the Hymenoptera order including ants and bees [3]. The adhesive mechanisms of tree frogs are still not fully understood by researchers, though their hexagonally-patterned toe pads are wetted with watery mucus (Figure 3.1a). Theoretical and experimental research has suggested contributions to their clinging ability from capillary, friction, viscous, and even suction forces [135].

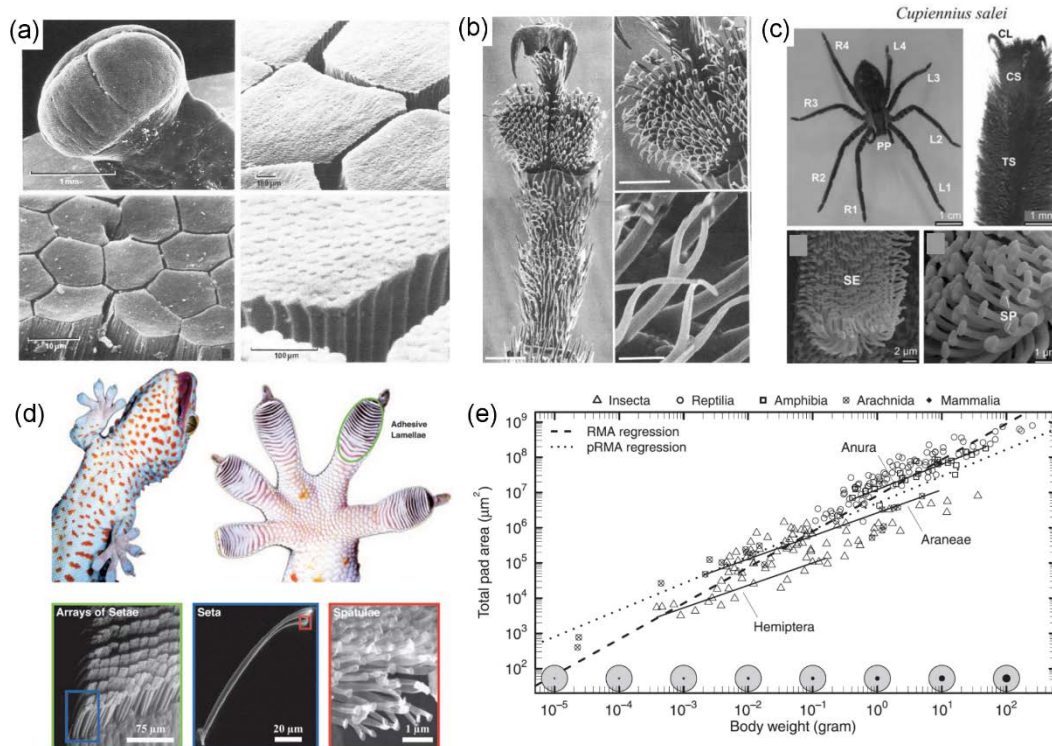


Figure 3.1 (a) Images of the toe pad of a frog, showing individual epidermal cells and mucous glands (reproduced with permission from [138]; published originally by Wiley, 1980, copyright Oxford Academic). (b) Scanning electron microscope images of the tarsus of the bruchus atomarius beetle (reproduced with permission from [139]; published originally by Wiley, 1980, copyright Oxford Academic). (c) Images of a spider's adhesive organs (reproduced with permission from [140]; published by Springer, 2006). (d) the structural hierarchy of the gecko adhesive system (reproduced with permission from [79]; published by Oxford Academic, 2002). (e) The relationship between body mass and pad area for a variety of animal taxa (reproduced with permission from [141]; published by the National Academy of Sciences, 2016).

Animals with hairy, or “fibrillar”, adhesive organs include flies [142], beetles (Figure 3.1b) [139], [143], spiders (Figure 3.1c) [144], [145], skinks [8], [146], anoles, and geckos (Figure 3.1d) [5], [147], [148]. Evidence indicates that fibrillar adhesive organs evolved independently for many of the animals that possess them, including lizard species of skinks, anoles, and geckos [8]. The gecko toe pads are particularly exalted among dry adhesive researchers, due to their impressive performance and, unlike many insect species, do not appear to require capillary forces to generate large interfacial adhesion [7], though evidence has been presented suggesting it may provide an enhancement under some circumstances [98]. There is good reason for the gecko to evolve superior performance: it has unusually large body mass for a climbing animal which relies on adhesion. As length L of a creature increases, its

volume and therefore mass will increase as L^3 , but the area of its adhesive organs increase as L^2 . The result is that either their adhesive organs must become disproportionally larger (Figure 3.1e) or their intrinsic performance per unit area must increase to provide the same secure grip [141]. For this reason, the adhesion strategies employed by larger insects and lizards such as the gecko are especially interesting to researchers interested in developing practical macroscale dry adhesives.

The hairs or fibers of biological adhesive pads are collectively referred to as setae, and among their many benefits is their ability to improve conformation to rough, natural surfaces. Surface roughness varies considerably between surfaces from the nanometer to millimeter scales, and usually includes variations across a wide range of length scales even for a single material or surface type. While smooth and compliant pads can conform well to relatively large variations on a similar length scale as their own, elastic stresses prevent a continuous pad from deforming and flowing around small asperities, thus reducing real contact area for many adherends and, correspondingly, the adhesive strength. Animals, needing to climb on surfaces with all possible length scales of roughness, must possess adhesive organs that adapt appropriately. Fibrillar structures are able to bend and buckle to reach the microscopic pits and valleys that a flat surface cannot reach, effectively presenting a more compliant surface to the adherend [149]. Longer, more flexible fibers present a softer and more compliant interface and are thus more effective for conforming and adhering to the rough surfaces most often found in nature [7].

A positive correlation between the areal density of setae and body mass has been discovered by researchers across a range of six orders of magnitude of body mass, strongly suggesting that smaller, denser contacts can lead to enhanced performance [105]. This observation agrees well with predicted benefits from contact mechanics models, a concept referred to as contact splitting. Creating very small contact points, while maintaining adequate fiber length, presents a challenge as high aspect ratio hairs are susceptible to various forms of damage including stiction, entanglement, and fiber rupture through excessive elongation. Animals requiring very small contact points, such as the gecko, have resolved this problem, in part, through the use of hierarchy; a relatively thick hair or bundle of fibers splits and gives way to finer hairs, finally terminating in nano-scale spatulae which form the final attachment surface [1], [7], [47], [98]. Durability is further enhanced by forming the setae of relatively rigid material, allowing longer and more slender fibers. Gecko setae are formed of keratin, a relatively tough

and rigid material with an elastic modulus of approximately 2.5 GPa common to many biological systems including human hair and finger nails [53], [150]–[152]. The combination of material rigidity and hierarchy enables gecko setae to reach lengths in excess of 100 μm while having terminal contact points in the form of spatulae only 200 nm wide [8]. Even these long fibers are inadequate to conform to rough and rounded surfaces alone; geckos and other animals employing relatively large adhesive pads instead enjoy a complex deformable sub-structure underlying the thin fibrillar surface which adapts to roughness at larger length scales in addition to performing the complex motions involved in locomotion.

The structure and material properties of setae also play a role in their ability to remain free of contaminants. Cleanliness is essential for any dry adhesive system, since a buildup of particles on the adhesive surface can seriously impede contact to the adherend. Animals relying on adhesive attachment must therefore have methods for avoiding particulate buildup, regardless of attachment method [31]. The gecko's spatulae have paradoxically been shown to shed particles, and thus avoid contaminant buildup, despite their strong adhesion [7], [29]. This occurs in dry conditions, i.e., without the need for water or other fluid to carry the contaminants away from the setae. Though not fully understood, it appears evident that the material and nanostructure of the setae are optimized to ensure that particles will tend to adhere more strongly to the surfaces the gecko walks on than to their setal surface, a process referred to as self-cleaning [29]. The need to self-clean is also likely the primary reason setal structures such as those of the gecko are typically made of very low surface-energy materials, despite the fact that high surface-energy fibers would provide enhanced performance in the absence of cleanliness and durability considerations.

In addition to providing a stable attachment point, an animal's adhesive pads must be capable of easy and rapid detachment from their adhered surface for effective locomotion. The method of effecting this change, or reversibility, of adhesion in animals is generally one of mechanical manipulation of their limbs and attachment organs. Many insects with smooth pads (arolia) have passive and active methods of folding and unfolding each arolium as they walk, either preventing or initiating peel failure at the interface as necessary [97]. Animals of many size scales with widely varying adhesive morphologies and mechanisms alter their adhesion substantially by controlling the direction of surface shear they

apply; attachment is maximized by pulling adhesive pads towards the body, while detachment occurs in the opposite direction [3], [97], [152], [153]. Of these, I will again use geckos as an important and oft-cited example in which directionality is a result of the mechanics of their setal microstructure [5], [7], [53], [152]. Gecko setal arrays extend from their substructure at an angle, a feature which strongly affects their adhesive characteristics. The tilted angle presents a more compliant surface, with fibers that bend in predictable directions rather than chaotically buckle, helping to prevent entanglement and interference between setae even under significant and varying deformation while conforming to rough natural surfaces. The setae are engaged with a surface through a short proximal dragging motion, in which the orientation is of critical importance [152]. Once engaged, the angle a gecko setal array is loaded has a dramatic effect on its adhesive strength, with detachment reliably occurring near a critical angle [53], [152]. Measurement of the setal work of adhesion has found that for a range of distal motion angles associated with adhesive detachment the work necessary becomes negative, indicating a net return of energy in contrast to the large dissipation normally associated with a strong adhesive [5]. The complex supporting structure and coordination of the gecko's motions enable it to take full advantage of the directional benefits afforded by its setal microstructure, able to attach and detach their adhesive toes in milliseconds while running vertically on nearly any surface at speeds comparable to terrestrial animals running on level ground.

3.2 Biomimetic Artificial Fibrillar Dry Adhesives

The study and development of artificial dry adhesive systems has overwhelmingly involved designs incorporating fibrillar structures. There is good reason for this, as the most celebrated natural dry adhesives utilize complex arrangements of fibers. To date, despite substantial effort and variety in approach, researchers have yet to produce an artificial adhesive which could fairly be called a practical fibrillar adhesive on par with a gecko's performance in terms of adhesion, reversibility, and durability. The fibrillar prototypes produced and associated performance testing have nonetheless advanced our collective understanding of dry adhesion and provided adhesives which do in fact out-perform geckos and other natural systems in certain circumstances, though usually at small (<1 mm) length scales. In this section, I discuss the expected benefits and associated challenges of producing artificial fibrillar structures and give examples of surfaces developed to investigate and exploit these benefits.

3.2.1 Benefits and Challenges of Artificial Fibrillar Designs

Solid surfaces that are atomically smooth are essentially non-existent in the world around us. Instead, all surfaces have some degree of roughness that inhibits adhesive contact between solids, and a successful dry adhesive must account for this in its design as explained in Section 2.4.2. As observed from biological systems, an adhesive surface coated with long and slender fibers is able to conform more easily to surfaces with roughness on a similar length scale as the fibers may bend and buckle as necessary to reduce the force and elastic energy required compared with a smooth adhesive surface. Thus, the enhanced compliance can improve adhesion both by increasing contact area to rough adherends and by increasing the critical energy release rate of the interface. Reducing the effective fiber modulus by increasing its length, for example, was determined in one recent study to increase the inelastic energy dissipation more effectively thus improving the interfacial work of adhesion [154].

Researchers have identified that the shape of a fiber's tip can affect the adhesion substantially [67], and furthermore that flared or mushroom-like fibers provide superior adhesive strength over competing designs. The performance enhancement of mushroom fibers is most readily explained by the fact that as the fiber is pulled in tension, stresses near the outside edge are reduced due to the greater compliance of the thin spatular membrane, which deforms rather than forming stress concentrations at the interface. The enhanced ability to deform in response to loads near the outer edge reduces stress concentrations, and thus stress is more evenly distributed across the interface compared with flat punch contacts. Fibrillar dry adhesive researchers have consequently focused substantial effort on creating designs which incorporate mushroom fibers [65], [68], [72]–[74], or the closely related film-terminated fibers which are frequently described as crack-trapping [76], [122], [123], [125], [126].

Fibrillar designs do not inherently confer reversibility to an adhesive surface. Rather, one must include specific design features to enable this quality. A common strategy directly mimics the adhesive pads of geckos by tilting the fiber, such that adhesion is maximized by shearing in one direction, and detachment occurs in the opposite direction as depicted in Figure 3.2. Several examples of polymeric fibrillar dry adhesives utilizing tilted fibers have been developed by researchers, indicating adhesive reversibility of up to a factor of 10 [40], [41], [68], [72]. The observation that gecko setae engage with a surface through a short drag distance has inspired the development of adhesives with microfabricated wedge-shaped

features [37], [155]. Arrays of microwedges were shown to successfully mimic some important aspects of gecko setae, including directionality, an impressive load-to-preload ratio, the ability to quickly and easily detach upon the removal of an engaging shear load, and resistance to damage, maintaining at least 67% of their initial performance after 30,000 cycles. Considering the direct influence of gecko observations, it is no surprise that this set of attributes appears specifically well suited for use in climbing robotics [20]. As an alternative to the directionally-dependent adhesion of angled fibers, researchers have additionally created fibers using stimuli-responsive materials in order to reverse adhesion on demand. A thermally sensitive fibrillar array composed of shape memory polymer was used as a structural layer for a thin tacky polymer film, possessing adequate compliance to adhere well to glass surfaces and showing a significant change to reversibility by simply altering the adhesive's temperature [156].

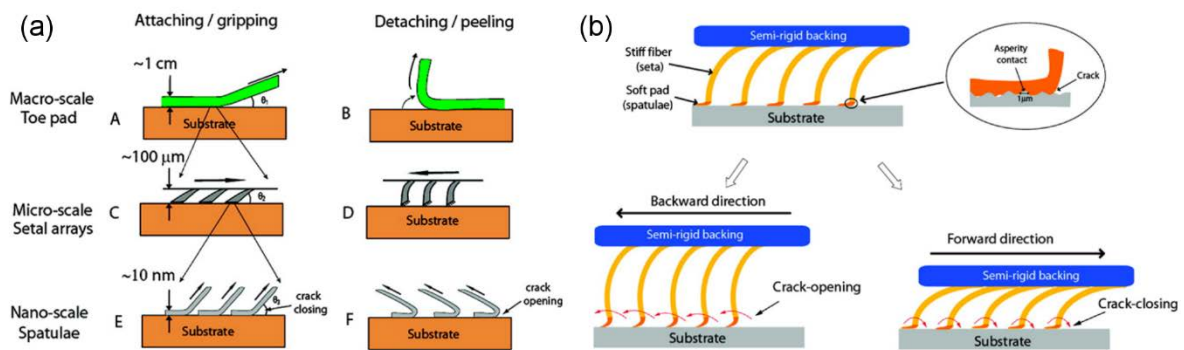


Figure 3.2 (a) Illustrations of gecko feet articulations at the foot, seta, and spatular levels. (b) Schematic and actuation of a gecko-inspired synthetic adhesive surface with directional adhesion. (reprinted with permission from [157]; copyright 2009, American Chemical Society).

Unlike dry adhesives found in biological systems, many biomimetic fibrillar designs are composed of relatively soft polymeric materials including polyurethane, poly(urethane acrylate) and polydimethylsiloxane (PDMS). The low elastic modulus of these materials enhances tack, and thus improves their ability to adhere to substrates, but also increases their susceptibility to particulate fouling. In most cases, this issue is outside the scope of the researchers' efforts and thus is given little or no attention. It is however a fundamental concern for the development of a truly robust and practical dry adhesive, and thus some researchers have given the issue special attention. Generally, the hydrophobicity of the surface is cited as an important factor in whether a surface is proficient in the

shedding of particles in either wet or dry conditions [25,98,99]. Hydrophobic surfaces are generally made of low-surface energy materials and may be made superhydrophobic through careful use of nanoscale structuring. Figure 3.3a–c provides examples of natural and artificial surfaces for which the benefits of hydrophobicity for self-cleaning are demonstrated. Figure 3.3d depicts an example of self-cleaning of a fibrillar adhesive in dry conditions. In this case, the researchers explain that for particles in a certain size range, the fibers make little contact with the particles and surface forces as predicted by the JKR theory are adequate to remove the particles from the fibrillar surface [43].

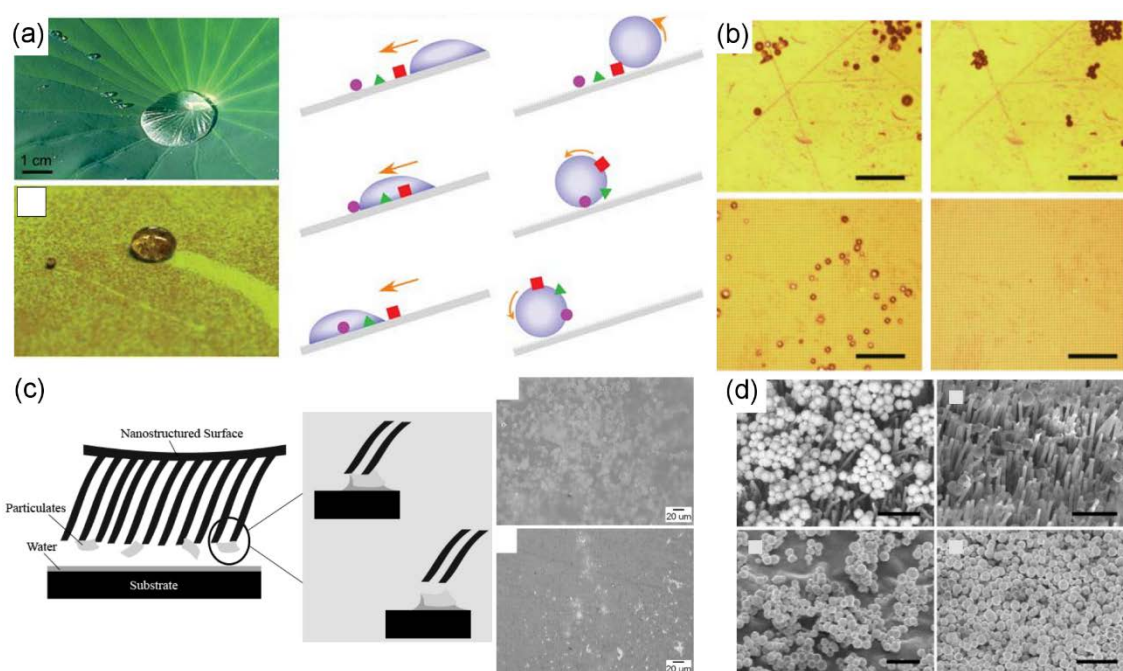


Figure 3.3 (a) Photographs and illustrations of the benefits of hydrophobicity for the removal of surface particles by water droplets (reproduced with permission from [158]; published by Cambridge University Press, 2008). (b) Comparison images of a flat (top) and artificial microfiber (bottom) polyurethane surfaces contaminated with silica spheres before (left) and after (right) rinsing with water, showing self-cleaning properties of the fibrillar adhesive (reprinted with permission from [33]; copyright 2009, American Chemical Society). (c) A proposed method of self-cleaning, whereby a thin surface layer of water pulls particles from a hydrophobic nanostructured adhesive surface (reproduced with permission from [51]; published by Wiley, 2007). (d) Images of a polypropylene fibrillar adhesive (top) and pressure sensitive adhesive (PSA) (bottom) first contaminated with gold microspheres and then after 30 simulated steps on a clean glass substrate (reprinted with permission from [43]; copyright 2008, American Chemical Society).

There is substantial evidence that adhesive performance correlates positively with increased fiber density and correspondingly smaller fiber contact points. Researchers face significant challenges when attempting to create dry adhesives utilizing very slender fibers however, due to both the inherent difficulties in manufacture and fundamental physical limitations that occur as fibers are scaled down in size. The theoretical limits of fibrillar structures are well-studied in the form of “adhesion design maps” [159], [160]. These maps are based upon a mathematical description of the various forms of failure which high-aspect ratio fibers may fail (fiber fracture and condensation), compared against the fibers’ requirement to form adequate surface contact (contact adaptability). A given adhesion map is produced given a particular set of assumptions regarding the properties of the interface and adhesive material, and provides a parameter space for an effective fibrillar adhesive system. An example map is provided in Figure 3.4a for fibers with spherical tips. In general, fiber fracture is expected to become problematic as fiber size decreases and material compliance increases, leading to greater elongation during loading. Fiber condensation, or the sticking-together of neighboring fibers to form a tangle or mat, is an issue inherent in particularly slender fiber arrays and have been often experimentally observed by researchers (Figure 3.4b,c) [66], [154]. Dimensionally smaller fibers created from stiffer materials may enhance adhesion while avoiding condensation related issues assuming contact adaptability remains satisfied.

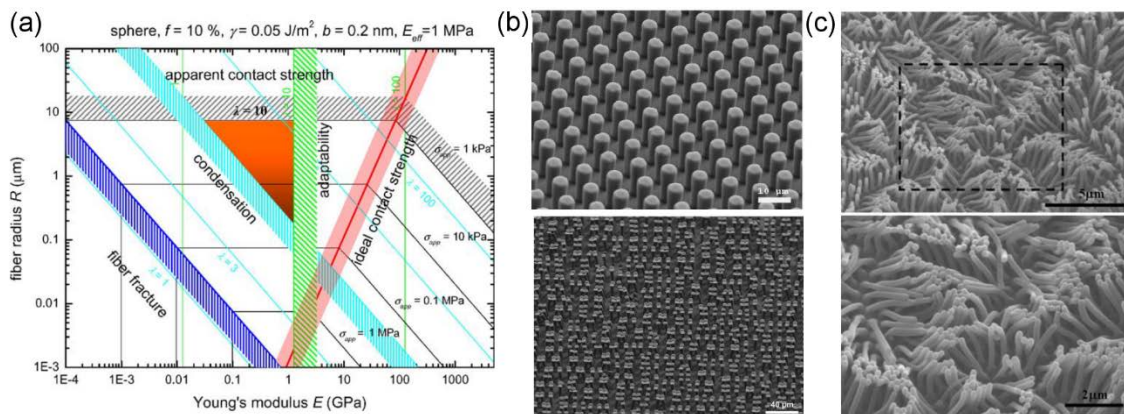


Figure 3.4 (a) Adhesion map for a fibrillar adhesive with spherical tips, given the parameters labeled a long the top of the map (reproduced with permission from [159]; published by Elsevier, 2005). Arrays of synthetic pillars showing (b) mild condensation by tip contact (reprinted with permission from [66]; copyright 2007, American Chemical Society), and (c) more severe condensation for higher aspect-ratio fibers (reproduced with permission from [50]; published by Springer, 2007).

3.2.2 Fabrication Techniques and Scaling Issues

The artificial dry adhesive systems described herein vary substantially in function and composition, and correspondingly require diverse fabrication methods. The method and complexity of fabrication strongly influences the practical size of the adhesive surface. Smaller, higher aspect-ratio surface features with 3D tip shapes and hierarchy have been shown to improve performance in many cases, but add fabrication complexity. Correspondingly, fibrillar structures are generally more challenging to scale up to create large adhesive surfaces than flat or simply-patterned surfaces.

Microscale fibrillar structures, those with fiber diameters greater than a micron, are most frequently composed of relatively soft polymers such as PDMS or polyurethane (PU) and have features defined by a mold created from traditional photolithographic techniques. A relatively simple approach involves the patterning of a negative-tone photoresist such as SU-8 to create a negative mold. Liquid polymer precursor fills the mold through capillary action, and subsequent curing and demolding give the resulting structure. Variations in this scheme have been used to produce a wide variety of fiber shapes and sizes, and have varying levels of corresponding complexity. Relatively simple vertically-aligned fibers with diameters of a few microns and varying lengths, up to several tens of microns, are straightforward to produce [66]. Producing tilted fibers is accomplished by illuminating the photoresist at an oblique angle when creating the SU-8 mold [68], [72]. Using multiple exposures at varying angles, fiber shape may be further influenced to produce wedge-shaped fibers which have broad bases and relatively slender but broad tips [155], [161]. A micromachining process to produce a mold with similar wedge features has been demonstrated, where a wedge indenter cuts the features into the mold's surface [162]. This process is described by its authors as cheaper, faster, and more versatile than the photolithographic method where the resulting wedge quality is highly sensitive to small variations in procedure and equipment quality. Various 3D tip shapes may be produced by dipping the fibrillar polymer surface onto a very thin film of precursor, and then manipulating the cure conditions of the wetted fibers accordingly [72]. Spatula, or "mushroom", tips may also be created by selectively etching a thin layer of photoresist below the SU-8, creating undercut features [163]. A variation on this approach uses SU-8 as a masking layer for an acrylic substrate which is then etched to produce mushroom-tipped acrylic and SU-8 fibers, from which negative silicone molds may be repeatedly produced [69]. The

advantage of this process is the larger size and reduced cost of the acrylic substrates versus the silicon generally used with other SU-8 processes.

Despite its cost, etching fibrillar cavities directly into a silicon, or silicon on insulator (SOI) wafer is a common approach due to the ubiquity of silicon processing equipment and technologies. High-aspect ratio features may be produced through deep reactive ion etching (DRIE) of silicon with a suitable masking layer [47], [76], [122], [126], [164]. An early example of a synthetic fibrillar adhesive using mushroom or spatula tips which demonstrated enhanced performance over a flat adhesive was created by casting a polymer in a mold produced through DRIE etching of the top silicon layer of an SOI wafer [65]. The buried oxide layer acts as an etching barrier, leading to lateral etching in a thin layer at its surface due to the notching effect from ion scatter, and is a process since adopted by other researchers [74], [75]. An interesting alternative approach involves using a silicon master to hot emboss low-aspect ratio features in a PMMA surface which are then drawn upwards at elevated temperature using an electric field. The fibers flatten and spread by electrowetting upon contact with the opposing electrode to form relatively slender, mushroom tipped fibers [165]. Film-terminated fibrillar surfaces have been created by first producing a micro-fibrillar surface through soft molding of a silicon master, then dipping the fibers in a thin film of polymer precursor to be cured [76], [122], [123], [125], [126]. Hierarchy may be added through successive molding steps, though this adds considerable complexity and cost to the process. A three-tiered fibrillar surface with spatula tips at each tier was produced by first creating 3D-printed molds for large stalks, which may be produced with straight or curved structure [47]. Smaller fibers are formed through successive soft molding against photolithographically-produced silicon masters in a process destructive to the silicon molds. Researchers interested in reducing cost and expanding the possible fibrillar materials beyond soft polymers have shown that a variety of fibrillar adhesive structures with complex shapes may be produced directly through 3D laser writing using an acrylic-based negative tone resist [166]. This process was shown to reproduce sub-micron features in hierarchical fibrillar arrays.

The theoretical and practical benefits of creating smaller contact points, and therefore fibers, has been well established. As feature size diminishes below the sub-micron scale into the nanoscale, traditional photolithographic techniques become increasingly challenging and ultimately impractical below

diameters of several hundreds of nanometers [40], [41], though other creative solutions have been developed and utilized to produce dry adhesives of varying practicality. Fibers in the 100 nm range have been produced from polyimide film with electron beam lithography in a process analogous to traditional photolithographic techniques [167], though fiber density and durability were somewhat limited. A more dense though more irregular forest of similarly sized nanohairs was formed using a self-assembling colloidal monolayer as a mask for chrome deposition on silicon, and ultimately DRIE to form the fibrillar negative mold. The researchers then deposited a layer of parylene, a hydrophobic and relatively rigid material with an elastic modulus of about 2.8 GPa meant to simulate the material properties of gecko foot hairs. The release process destroys the silicon mold. Similarly stiff fibers made of olefin of a half-micron diameter have been produced from polycarbonate membranes with nanoholes, without the need for special photolithographic techniques [42]. Additional methods include wax indentation [104], and electrospinning which can create a soft hierarchical surface, though with fibers in a somewhat unorthodox lateral orientation [55], [57]. Germanium (Ge) nanowires coated in parylene have been fabricated by first chemical vapor deposition (CVD) of the Ge followed by parylene deposition, producing a highly hydrophobic and adhesive surface. Carbon nanotubes are frequently used by researchers desiring the smallest possible fiber diameter, capable of creating contact points truly on the scale of nanometers [39], [45], [70]. The nanotubes are thermally grown at high temperature on a specially prepared surface through chemical vapor deposition, but may be transferred via gluing to microscale fibrillar structures to create a hierarchical structure to further enhance surface compliance [70].

3.3 Alternative Strategies for Enhancing Artificial Dry Adhesive Performance

The difficulties of creating effective fibrillar designs have, in part, inspired work on alternative designs and methods which may prove to be more easily scalable. The alternative designs described herein may be grouped into one of two categories: those which employ passive compliance control determined by their construction and loading direction, and those featuring active compliance control through the use of stimuli-responsive materials.

The term passive compliance control is used here to describe adhesives which are designed such that the compliance changed substantially depending on the direction of loading. The compliance should be

large in the direction necessary for conformal bonding to an adherend, but relatively small in the direction of loading to effectively control elastic energy storage and release, similarly to many tilted fibrillar structures. A method of accomplishing this feat is by fabricating an elastomeric composite comprised of a thin, compliant polymer sheet with a relatively inextensible fabric within [56]. The thin and compliant polymer may conform to curved or bumpy surfaces, while the embedded fabric prevents excessive deformation of the polymer when loaded, reducing stress concentrations and enhancing effective adhesive strength. Selecting the point of loading is additionally important; the researchers discovered loading the adhesive sheet from its center via a “tendon” improves adhesive strength in tension, in much the same way that a spatula or “mushroom” cap enhances fibrillar adhesion. Removal of the dry adhesive is easily performed by peeling from its edge, such that the fabric does little to limit the concentration of stress. Multiple recent studies have continued developing this method of creating a practical, scalable dry adhesive. Issues addressed include adhesion enhancement through surface patterning [64], the effect of surface roughness on adhesive performance [62], the importance of the composite properties and geometry [61], and environmental sustainability [63]. A structurally distinct adhesive system for climbing robotic applications has been developed making use of strikingly similar mechanical principles [20]. Several smaller, but more rigid, panels are coated with a microstructured adhesive layer and supported by a compliant structure, with load transferred from each panel to its supporting arm via an inextensible tendon attached to the panel’s center. The effect is a system which behaves as a compliant surface when contacting its adherend, but effectively distributes load across its adhesive interface by virtue of its selectively rigid features. Reversibility is provided by its surface microstructuring, rather than through edge-peeling.

Active compliance control requires a means of actuating, or otherwise stimulating, the adhesive material to alter its mechanical compliance. The potential advantage over passive compliance control is that loading and release motions must no longer be pre-defined or different from each other, simplifying mechanical support and control schemes. The special relevance of this advantage for very small scale adhesives, where developing complex support and actuation systems is particularly challenging, will become apparent in the following chapter. A relatively simple method of active compliance control for an adhesive application was explored wherein mechanical compression was applied to a polymer film

a short distance from its adhesive region with the intent to reduce the system's overall compliance in the direction of loading [58], showing modest but measurable gains in performance. A composite polymer with magnetic powder was used as a supporting structure in another work [168]. Applying a magnetic field to the composite induced strains which affected compliance according to the orientation of the field. Though this example produced only a minor effect on adhesive performance, magnetic actuation of a material has a strong advantage over many competing methods of active compliance control in terms of speed and the ability to place the energy delivery device relatively far from the active material. A better approach is needed to achieve the potential benefits of active compliance control adhesives.

3.4 The Use of Shape Memory Polymers in Dry Adhesive Systems

A robust and attractive method for compliance control comes in the form of stimulus-responsive polymeric materials, referred to as shape memory polymers (SMPs). An SMP is one which has an original “permanent” shape, which may then be deformed and under certain conditions, fixed into a “temporary” shape, as shown in Figure 3.5a. Under the influence of a stimulus, usually by heating, the elastic stresses fixed within the deformed polymer are released and it returns to its permanent shape. Over the past decades, researchers have developed many varieties of SMP, with widely varying mechanical properties and mechanisms for producing their shape memory effect [169]–[171]. Chemically crosslinked SMPs that function by undergoing a thermal glass transition are generally the most desirable for dry adhesive applications, due to their chemical, thermal, and mechanical stability. These SMPs tend to be especially rigid below their glass transition temperature (T_g), but soften substantially when heated, changing their compliance by a factor of one hundred or more. The capability of dynamically controlling the compliance, and fixing or “freezing” imposed strains in place to temporarily remove restoring forces, are substantial advantages in terms of allowing the dry adhesive system to control its mechanical behavior. A typical bond/de-bond cycle for an SMP-based dry adhesive involves:

1. A bond phase, wherein the SMP is heated above its T_g to increase its compliance, allowing thorough conformation to the opposing substrate,

2. A cooling and unloading phase, wherein the SMP is cooled below its T_g to reduce compliance and fix its shape, at which point it has maximized its adhesive bond strength,
3. A removal phase, wherein the SMP is re-heated above its T_g , increasing its compliance and releasing stored strains so that it may be removed easily.

There exist previously published works in which SMPs were used as a structural component of dry adhesive systems. In these cases an additional “adhesive” layer was added to make direct surface contact, with one such example shown in Figure 3.5b. The adhesive layer is chemically similar to the SMP, modified so that its glass transition temperature (T_g) is below the room temperature, and thus the polymer is soft and tacky in normal conditions. Relatively large and simple to produce adhesives using this strategy were developed, where bonding and removal were initiated through heating the SMP above its T_g [59], [172]. The reversibility of the adhesives relies on thermal mismatch between the SMP and adhesive polymer to create a “self-peeling” effect when heated. A somewhat more complex design incorporating microscale SMP fibrillar structures terminated with a continuous thin adhesive polymer layer was also developed, with the intention of improving the surface compliance during bonding and thus improving adhesion to more rough an uneven surfaces [156].

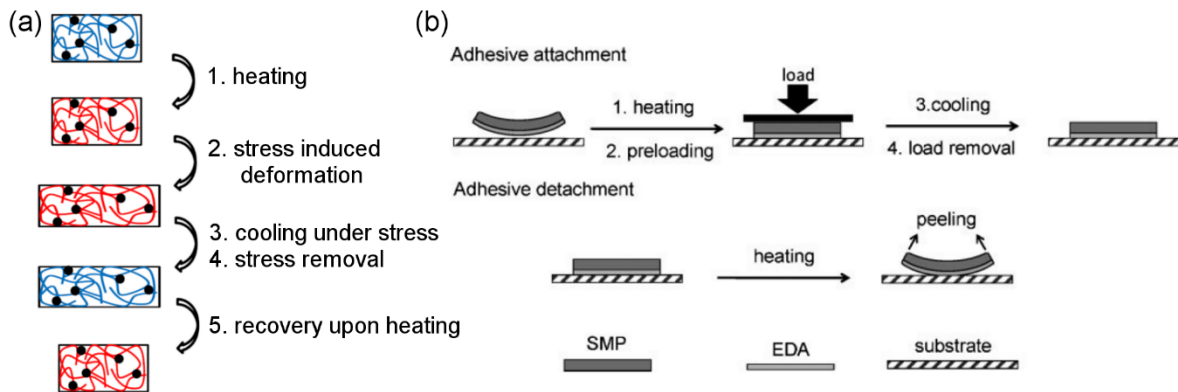


Figure 3.5 (a) The molecular mechanisms of the polymeric shape memory effect, for a thermo-sensitive shape memory polymer (SMP) (reproduced with permission from [169]; published by Elsevier, 2011). (b) The bonding and debonding process for a bilayer SMP adhesive (reproduced with permission from [59]; published by Wiley, 2010).

These bilayer designs demonstrated impressive adhesive strength and release capabilities, well beyond what is expected from similarly structured systems which do not utilize active or shape memorizing materials. However, the presence of the tacky adhesive layer presents some potential issues in an SMP-based dry adhesive system which may be alleviated in a system where the SMP comprises both the structural layer and the contact surface. First, adding a continuous film to the surface of the SMP substructure represents an additional manufacturing step adding to the production cost. Although the example of Reference [156] demonstrates it is possible to apply a continuous film atop an array of SMP micropillars, this is not necessarily the case for arbitrary substructure designs, nor will continuous films be desirable for every purpose. If the adhesive layer may be eschewed, the design of the adhesive surface may only be constrained by one's ability to produce and release the SMP from a mold. By removing the intervening adhesive layer, the effect of the SMP's changing compliance and shape fixing properties are both enhanced, potentially improving the adhesive's reversibility. This is particularly important in cases where the adhesive's maximum strength is of secondary importance to its minimum strength, a typical circumstance in microscale applications including transfer printing operations. Additionally, the tacky adhesive layer is susceptible to fouling, while a bare SMP surface has greater resistance to particulate accumulation while stored or between use cycles due to its increased rigidity at room temperature.

The remainder of this dissertation describes the design, operation and performance of a variety of direct-contact SMP dry adhesives that I have developed. Microscale SMP-based dry adhesive systems for transfer printing are described in Chapter 4, highlighting several of their unique strengths over previously demonstrated systems for both serial and parallel printing operations. Previously-established release mechanisms for polymer stamps are shown to compliment the shape fixing nature of SMP with excellent results, and multiple methods of locally and rapidly heating the SMP to activate its bond and/or release mechanism are demonstrated. Larger SMP-based adhesives for general use are developed in Chapter 5, demonstrating that the strong microscale performance translates well as linear scale increases. Finally, several variations on the prior SMP formulation are tested in Chapter 6 where they are shown to significantly improve adhesive performance in several respects, indicating that further exploration of alternative SMP formulations would likely prove fruitful.

Chapter 4. The Use of Shape Memory Polymers for Transfer Printing

Fabricating microsystems presents a set of challenges distinct from those that exist for manufacturing macroscale devices. Chief among these challenges is the difficulty of manipulating individual objects due to vanishing body forces compared with surface forces. Owing to these challenges, monolithic microfabrication, i.e. layer-by-layer in-situ fabrication of all components using electrochemical processes, is commonly used to fabricate microsystems [173]. However, this approach has substantial drawbacks for the fabrication of non-planar structures, particularly when the integration of heterogeneous materials is desired, necessitating the development of complex and lengthy process steps to selectively and precisely deposit and etch materials without damaging those already in place. Even with well-crafted recipes, such fabrication methods have severe limitations in terms of producible geometries and compositions. It is relatively simple, using traditional microfabrication, to fabricate large arrays of simple structures composed of one or a few compatible materials. Pick-and-place microassembly techniques relying on probe tips or microgrippers are capable of assembling separately-fabricated components into microsystems with high flexibility and precision, representing an approach to constructing microsystems that are impossible with monolithic microfabrication [174]. There is a lower limit for these processes below which the release of a retrieved microcomponent becomes excessively challenging, which has lead researchers to develop additional complimentary strategies including rolling [175], vibrating [176], mating [177], and relying on electrostatic interaction [178] or tacky adhesives [179].

An arguably more versatile set of solutions to this problem tackles the issue by investigating means of directly controlling surface forces. The term transfer printing describes this set of assembly techniques which have experienced growing utility and popularity in recent years, offering unique capabilities in integration, assembly and fabrication of micro/nanomaterials. Three distinct categories of transfer may be defined: additive, subtractive, and deterministic assembly [180]; the last of these methods is particularly powerful due to its natural compatibility with high performance, single crystalline semiconductor materials (such as Si, GaAs, GaN, InP, etc.), and is accordingly the focus of the work presented in this chapter. In general terms, deterministic assembly by transfer printing refers to a diverse set of protocols for the assembly of pre-fabricated solid components, referred to as "inks" arrayed on a

donor substrate, onto a separate receiver substrate to produce one or many functional devices. Inks may be prepared in many physical forms (block, membrane, sphere, etc.), and may be composed of nearly any class of material including inorganic semiconductors, metals, carbon, colloids, organic and biological materials. Semiconductor and metallic inks may be bonded together through thermal processes in a process termed micro-LEGO, or micro-masonry, to form a final device with secure mechanical and electrical bonds between printed components [181], [182]. Possible substrates are as diverse as the set of inks, with semiconductors and flexible polymers being the most commonly used in the assembly of microsystems; the former is heavily used due to its well-established compatibility in the microelectromechanical systems (MEMS) industry, while the latter enables the fabrication of novel flexible devices with potentially revolutionary applications particularly in the fields of health care [183], [184], sensing [185], and optoelectronics [186]. The majority of transfer printing-based assembly techniques make use of an elastomer, usually polydimethylsiloxane (PDMS), as a stamp material to first retrieve inks from the donor substrate and to then print the inks on a receiving substrate. The core challenge of transfer printing via PDMS or any alternative material is the control of adhesion and interfacial crack behavior between the stamps, inks, and substrates involved. Improving the performance of a transfer printing process therefore fundamentally focuses on better control of the adhesive forces between stamp and ink, particularly where receiver surface modification to improve printing yield is not desirable.

Though much success has been achieved using PDMS as the functional material, its performance is fundamentally limited due to its reliance on time-sensitive viscoelastic-based, or kinetic, adhesion control. A simple flat-surfaced PDMS stamp moving perpendicular to an ink surface can achieve a ratio of adhesion reversibility of approximately 3 to 1 purely by modulating retraction velocity [187]. This degree of reversibility is inadequate for all but the most ideal printing situations, typically because the minimum adhesion is too great to allow for release of the ink. For this reason, several advanced transfer printing techniques have been developed to reduce the minimum adhesion during printing utilizing shearing forces [46], [188], laser heating [189], stamp inflation [190], or microstructured stamp surfaces [187]. Of these methods, microstructuring of the stamp surface is particularly versatile and simple to

implement due to its passive operation, allowing for an adhesion reversibility ratio of over 1000 to 1 for any ink material and without requiring high temperatures or shearing stresses on printed structures.

The microstructured surface is designed such that it flattens under compression to transiently generate large adhesive area during ink pickup, and elastically reconstitutes its original, unflattened shape after pickup has been achieved thereby contacting the ink at only a few small points to minimize adhesion for printing. However, the time sensitive nature of the stamp reconstitution imposes limits on the designs of both the stamps and inks that may be used. Though PDMS stamps can conform well to inks of complex 3D geometry while compressively loaded, they are inherently unable to maintain conformal contact throughout ink retrieval and printing due to their rapid elastic reconstitution upon the removal of compressive preload. Consequently, the undeformed shape of the stamp must adequately fulfill multiple roles with opposing requirements; the ink must be securely held in a favorable orientation during transport to the receiving substrate, but must also be easily released during printing. Incompatible stamp-ink designs may result in prematurely dropped inks or misalignments during printing due to tilting and shifting of the ink during stamp reconstitution. Likewise, stamps designed to retrieve and transport heavy or complexly-shaped inks incur significant penalties to printing performance, such that these inks are generally infeasible to use in PDMS-based transfer printing. Finally, though most research has focused on the challenge of enhancing ink release, ensuring pickup is no less important. The maximum adhesion attainable with a PDMS stamp is relatively low at around 0.1 MPa, requiring careful design of inks in order to allow pickup to reliably occur. The design typically requires a large flat and level area on the top of the ink to provide an ideal interface with the stamp, and a delicate supporting structure underneath the ink that will easily separate from the ink during pickup [191]. Larger inks with fragile designs and non-uniform surfaces also represent a special challenge during pickup due to the relatively poor adhesion and compliant, viscoelastic nature of PDMS. It is common for some portions of a complex ink to break free of the substrate before others during the rapid retraction phase, potentially causing ink fracture even when pickup is otherwise successful.

4.1 Single-Unit Transfer Printing Using SMP

The initial theoretical and experimental investigation regarding the use of SMP as a transfer printing tool focuses on single-unit printing, i.e. using a single stamp to manipulate a single ink for each print

cycle. The SMP chosen for this task is the formula NGDE2 described in Appendix A, which has several highly desirable properties including being simple to produce, excellent feature reproduction when molded, a very high degree of optical transparency, good chemical and thermal stability, exceptional shape fixity and recovery factors (>98%), a convenient T_g (~40 °C), and a large compliance change across its narrow T_g transition range. The preceding chapters have established that adhesive performance enhancements should be expected for a microscale SMP stamp owing to its active compliance control and shape fixing abilities. In this section I attempt to estimate the expected performance gains according to theoretical predictions based on linear fracture mechanics and compare these estimates against actual test results using SMP stamps of the same dimensions. Relief features are added to the stamp surface to further enhance printing performance, and methods of heating are developed and discussed. Several configurations of inks which are challenging to print by more traditional transfer printing techniques are finally assembled.

4.1.1 Microscale Adhesion Performance

Consider an SMP stamp with a flat surface which forms intimate and uninterrupted surface contact with an opposing substrate. As an approximation to predict the effect of stamp rigidity on adhesive performance, linear elastic fracture theory is employed. It is assumed a small crack exists at the edge of the interface. The energy release rate G for a propagating crack in a homogeneous isotropic material for plane stress conditions is given as

$$G = \frac{K_I^2}{E} \quad \text{Eq. 4.1}$$

where K_I is the mode-I stress intensity factor and E is the material's elastic modulus, for which storage modulus may be substituted for analysis of SMP. In the case of fracture between the stamp-substrate interface, the mismatch between the elastic moduli of the two materials must be accounted for. The effect of the mismatch on energy release rate has been previously investigated [192], and recognizing that the elastic modulus of SMP is very small compared with that of the silicon substrate, it is sufficient to treat the bimaterial interface as a homogeneous interface with double the elastic modulus of the SMP. In this case, the energy release rate becomes

$$G = \frac{K_I^2}{2E_{SMP}} \quad \text{Eq. 4.2}$$

The mode-I stress intensity factor for an edge crack of length a in a semi-infinite material subject to an evenly distributed stress σ is given by [193]

$$K_I = 1.1215\sigma\sqrt{\pi a} \quad \text{Eq. 4.3}$$

To derive the expected pull-off force, it is assumed that the crack will begin to propagate when the energy release rate reaches the SMP-substrate work of adhesion γ_o . It is further assumed that an initial crack length of 1 μm exists at the edge of the interface, giving an a/L ratio of 0.01 for the square stamps of 100 μm width under investigation, where L is the width of the stamp. Inserting Equation 4.3 into Equation 4.2 and rearranging, recognizing that $\sigma = F/A = F/L^2$, yields

$$F_{\text{pulloff}} = \sqrt{25.31\gamma_o(2E_{SMP})}L^3 \quad \text{Eq. 4.4}$$

An Abaqus finite element analysis (FEA) was performed in Reference [194] using analogous assumptions where it confirmed the validity of the analytical solution of Equation 4.4 which is plotted in Figure 4.1b using a thermodynamic work of adhesion between SMP and silicon estimated to be 46 mJ m^{-2} (see Appendix A.7).

Using test procedures similar to those used previously for similar PDMS stamps [187], the preceding predictions may be tested using an SMP stamp and a silicon substrate. Fabrication of the SMP stamps is described in Appendix B.1. Fully utilizing the shape-memory properties of SMP requires the retraction step to occur at a temperature below the glass transition zone, corresponding to a stamp rigidity greater than 3 GPa, occurring when the SMP temperature is below 40 °C. However, in order to better investigate the role of the stamp's rigidity on its adhesive performance, the stamp is also tested at intermediate temperatures within its glass transition zone. The essential steps of the testing procedure are illustrated in Figure 4.1a, showing how a bond is formed and adhesion is tested for SMP stamps at varied retraction temperatures, and thus at varying values of stamp rigidity, or storage modulus. More complete details are provided in Appendix B.3.

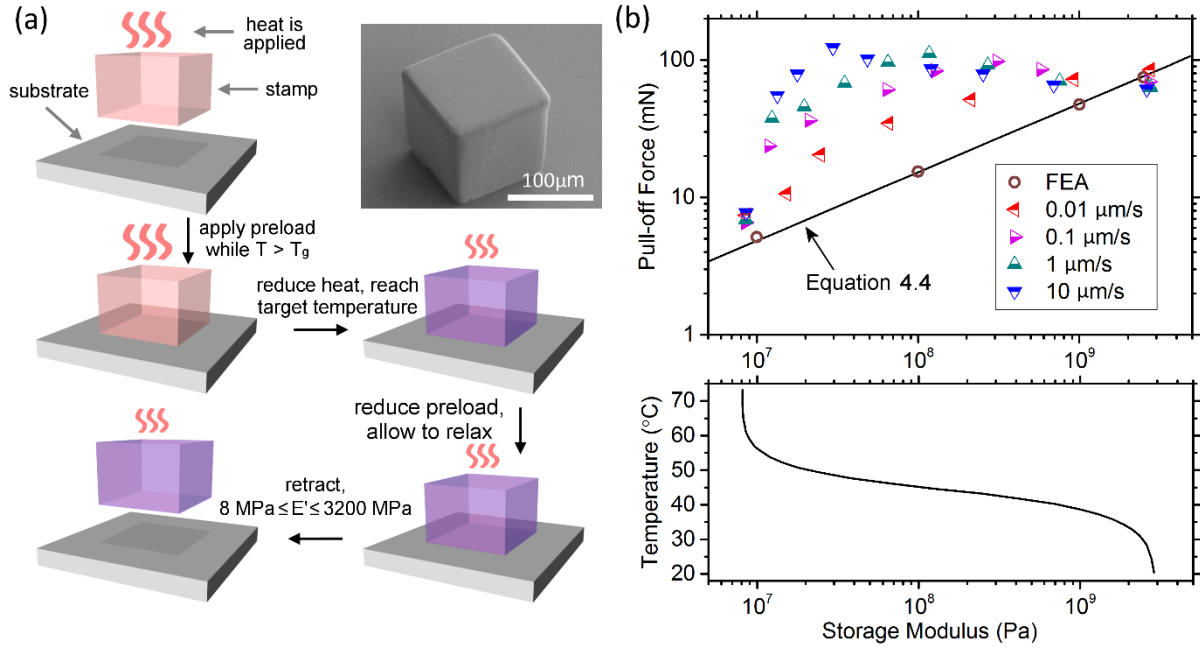


Figure 4.1. (a) An adhesion test schematic for a flat SMP stamp, showing the steps for testing with varying stamp storage modulus. (b) Pull-off force versus storage modulus for a 100 μm x 100 μm flat post stamp for various retraction speeds. The analytical solution of Equation 4.4 and linear elastic finite element results are compared. The temperature corresponding to each value of storage modulus, spanning the SMP glass transition zone, is shown.

Adhesion data was collected for a range of temperatures and retraction speeds using a 100 μm \times 100 μm flat SMP stamp. When compared to the linear elasticity-based analysis, the adhesion data shows more complex behavior. The adhesive strength of the interface is highly dependent upon retraction speed, indicating a strong viscoelastic effect within the glass transition zone. The effect of polymeric viscoelasticity on adhesion has previously been studied [195]–[198]. The adhesive strength of polymers may be more thoroughly described by accounting for viscoelasticity using an equation of the form given in [195],

$$\gamma_{eff}(\nu, T) = \gamma_0 [1 + f(\nu, T)] \quad \text{Eq. 4.5}$$

Where γ_{eff} is the amount of energy required to advance the crack tip by one unit area, γ_0 is the energy required to break the interfacial polymer-substrate bonds at extremely low crack velocities, and $f(\nu, T)$ describes the bulk viscoelastic energy dissipation in front of the crack tip as a function of crack tip velocity and temperature. The viscoelastic dissipation term vanishes as crack tip velocity approaches zero.

The collected adhesion data in Figure 4.1b is in agreement with this expectation, with adhesion increasing as retraction velocity is increased. The effect of velocity is greatest near to the "center" of the glass transition zone where the loss modulus, a measure of viscous dissipation within the polymer, reaches a maximum. At the tail ends of the glass transition region, where the loss modulus is very small compared with the elastic modulus, the adhesion is relatively unaffected by retraction velocity. As the retraction speed is reduced, the adhesion approaches the linear elastic result predicted by Equation 4.4 due to the diminishing contribution from viscous dissipation. Since typical operation of the SMP stamp requires that pickup and print events occur below and above the glass transition zone, respectively, to take advantage of the shape memory effect, the stamps are relatively insensitive to the retraction speed in practice. Since a polymer's work of adhesion is not significantly affected by small temperature variations, it is concluded that the primary factor affecting the change in adhesion between the hot ($T > T_g$) and cold ($T < T_g$) states of the SMP stamps is the change in storage modulus. The SMP at room temperature is three orders of magnitude more rigid than PDMS, corresponding to a factor of 30 expected increase in maximum adhesion assuming similar surface energies. Accordingly, our experimental results show SMP stamp cold-state adhesion is in excess of 5 MPa (50 mN for $100\text{ }\mu\text{m} \times 100\text{ }\mu\text{m}$ stamp), which compares with 0.15 MPa previously demonstrated for equivalent PDMS stamps [187].

From these results it is surmised that the performance of a flat-surfaced stamp benefits from the ability to control the SMP's elastic modulus, but experiences little benefit from the shape-fixing and recovery aspect of the material since its shape experiences only minor changes during a printing cycle. To fully realize the performance advantages which may be afforded by the SMP's shape fixing ability, the stamp surface may be microstructured to form a well defined "adhesion-off" state which has minimal contact area with an ink. The microstructures may be compressed during ink pickup to mimic the "adhesion-on" performance of a flat stamp, with the elastic energy stored during the stamp compression providing the energy required to resume its adhesion-off configuration when heated during printing. A well-established example of this is the pyramid "microtip" surface patterning previously developed and tested for use with PDMS stamps [187].

4.1.2 Microscale Relief Features Improve Adhesive Reversibility

A prototypical example of a transfer printing process using a microtip SMP stamp is illustrated in Figure 4.2a. During the process, the stamp assumes two shapes: a "permanent" adhesion-off shape as shown in Figure 4.2b, and a "temporary" adhesion-on shape as shown in Figure 4.2c. The permanent shape is defined by the curing of the SMP in a corresponding mold, while the temporary shape is programmed as shown in Figure 4.2a by a combination of heat and compressive preload between stamp and ink. Once cooled in this configuration, the adhesion-on state may be maintained throughout the lift, transport, and placement steps of the printing process. Only the application of heat is required to switch the stamp to its adhesion-off state where the adhesion is nearly eliminated to facilitate ink release. This is an important, but difficult-to-quantify benefit afforded by the SMP material since it allows one to maintain the orientation of the ink from the pickup to printing steps. Though the SMP microtip design reduces adhesion in the adhesion-off state substantially, further improvements are possible. The apex of each microtip has a small radius of curvature which is further flattened by local adhesive forces [187].

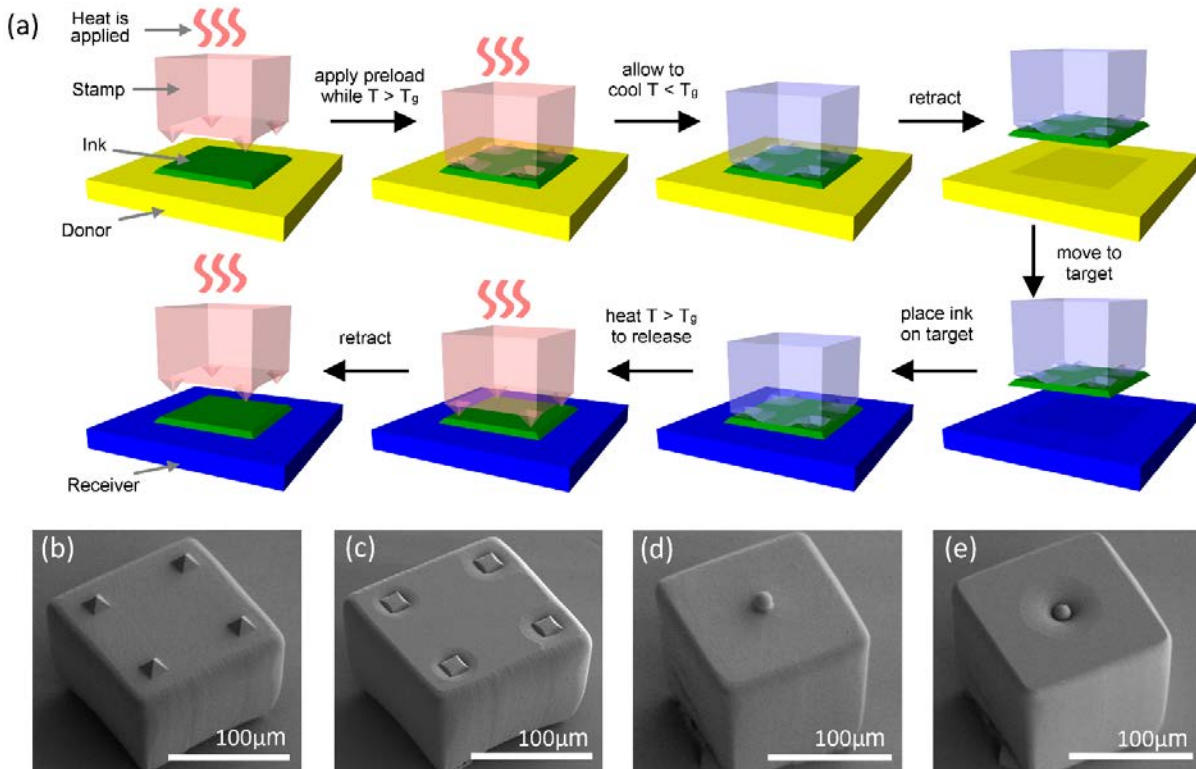


Figure 4.2. (a) Implementation of SMP microtip surface in a stamp for deterministic assembly by transfer printing. (b) Microtip stamp in permanent, "adhesion off" state. (c) Microtip stamp in temporary, "adhesion on" state. (d) Silica-sphere stamp in permanent, "adhesion off" state. (e) Silica-sphere stamp in temporary, "adhesion on" state. Scale bars are 100 μm .

Further reduction in adhesion is desirable when ink-to-substrate adhesion is especially low, and for this purpose it can be beneficial to replace the function of the microtips with a rigid material. One example of this is a stamp with one or more silica spheres positioned on its surface, as shown in its adhesion-off state in Figure 4.2d, and in its adhesion-on state in Figure 4.2e. The rigidity and surface roughness of the silica sphere provides a point of contact with exceptionally low adhesion to the ink during printing [199]. Fabrication details may be found in Appendix B.1.

Figure 4.3 demonstrates the improved printing performance of the advanced microtip and silica-sphere SMP stamps over a basic flat post stamp, using a silicon substrate to represent the standard ink material. Figures 4.4a,b show typical force versus time behavior during the tests for the flat post and microtip stamps, respectively. The plots begin with a relatively large 10 mN preload to fully compress the stamps

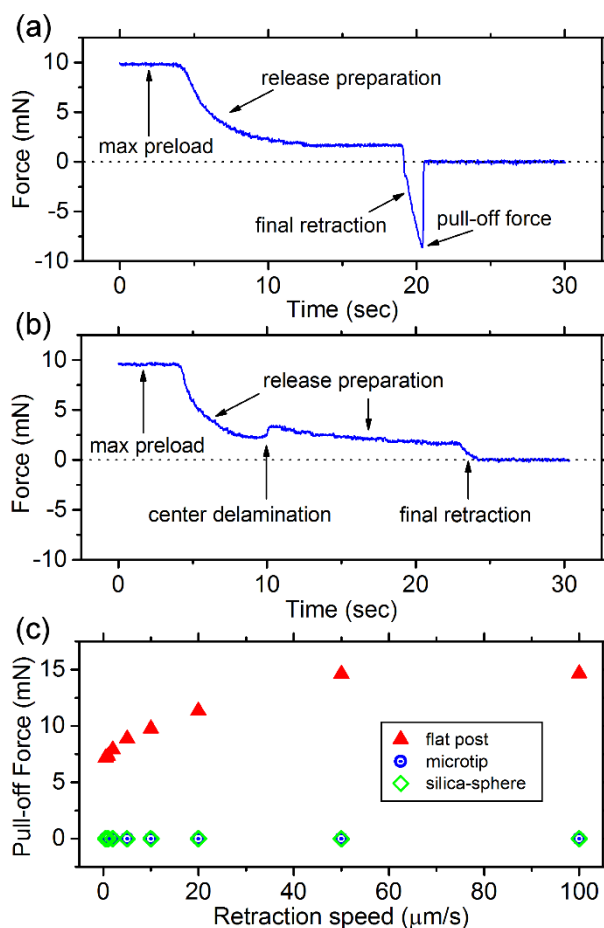


Figure 4.3. Measured-force versus time curves for a flat post SMP stamp (a) and a microtip SMP stamp (b). (c) Pull-off force versus retraction speed for three SMP stamp designs. Tests are performed while heated above T_g (“adhesion off”), and show the superior release characteristics of the microtip and silica-sphere stamps.

to make full contact with the substrate surface, followed by a release preparation step where the preload is reduced to approximately 1.5 mN. This step was included to ensure that the stamps assumed their adhesion-off state prior to measuring their net adhesion, referred to as the pull-off force. In the final step, the stamp is retracted from the substrate while heated above T_g . The pull-off force is the peak adhesive force generated as the stamp separates from the substrate and is shown in Figure 4c for several retraction speeds ranging from 0.5 to 100 $\mu\text{m s}^{-1}$. The flat post stamp shows significant adhesion for all speeds, increasing with increasing retraction speed. This behavior is characteristic of viscoelastic polymer stamps, including PDMS [187]. The advanced stamps demonstrate adhesion below the noise threshold of our load cells (<0.2 mN), and are taken to be nearly zero at all velocities thus demonstrating their suitability for printing inks. This improvement in adhesion-off performance is achieved with only a minor penalty to adhesion-on performance. Experimental results show that our advanced SMP stamp designs maintain at least 80% of the "adhesion on" strength of a comparably sized flat-post stamp, roughly corresponding to the reduction in adhesive area caused by the surface relief features. A quantitative comparison of adhesive performance between a variety of stamps created for the purpose of microassembly, including flat and microtipped SMP stamps, is shown in Table 4.1. It may be seen that microstructured SMP stamps combine superior adhesive strength and reversibility, due to the material's compliance-modulation and shape memory effect in combination with advanced surface microstructure design.

Table 4.1 Comparison of adhesive strength and reversibility for various stamps available in literature and SMP stamps

Material	Stamp surface geometry	Max adhesion (kPa)	Reversibility (max:min)	Adhesion control	Ref.
PDMS	flat ^a	50	50:1	inflation	[190]
		85	>10:1	shear motion	[188]
		150	3:1	kinetic	[187]
	flat ^b	100	100:1	shear motion	[46]
	microtip ^a	80	>1000:1	contact area change	[187]
	pedestal ^a	1600	2:1	kinetic	[200]
			∞ :1	laser-heating	
ST-1087	flat ^b	1450	39:1	buckling	[201]
SMP	flat ^a	3200	6:1	rigidity change	this work
	microtip ^a	2800	>1000:1	rigidity & contact area change	

^a vertical sidewalls

^b angled sidewalls

4.1.3 A Resistive Method of Rapid Localized Heating

The heat source used to trigger thermal transition in the SMP may take many forms. Centimeter-scale resistive heaters may be used to bring the substrate, stamp, and surroundings to an isothermal state, as was done to collect the adhesion data presented in the previous section. There are two significant drawbacks to using a heat source of this size. Thermal cycle time is prohibitively long, and thermal expansion of materials above and below the stamp during the cooling phase of the bonding process means active displacement control of the stamp is necessary to maintain the proper preload and assure a proper bond is made. Both of these difficulties are effectively eliminated by using a more localized heat source.

The thermal response time of a system is proportional to the square of the length scale, by inspection of the Fourier number. By shrinking the heated region to a scale comparable to the SMP stamp, the response time is reduced to the order of one second or less. In addition, the reduced size of the heated region greatly reduces the total thermal expansion of the system, eliminating the need for active control

of stamp position during cooling. The simplest method of generating heat at this scale is to fabricate the stamp over a small resistive heat source, with cooling accomplished passively by turning the heating element off. Two such resistive heaters have been designed and used to demonstrate this method of operation; one heater design made of sputtered NiCr wire (Figure 4.4a), and the other from transparent indium tin oxide (ITO) (Figure 4.4b).

The NiCr heater demonstrated particularly rapid thermal response time, due to its small size. Shape

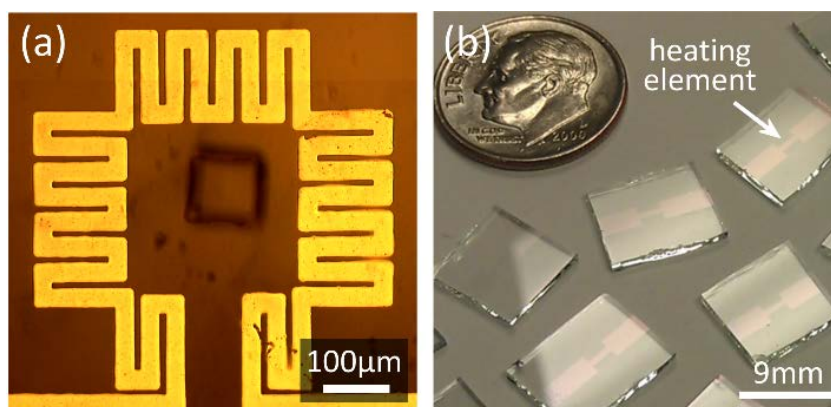


Fig. 4.4. Two resistive microheater designs have been fabricated for use with SMP stamps; a serpentine design (shown with integrated 100 μm by 100 μm square flat post SMP stamp) made of sputtered NiCr in (a), and a transparent ITO design in (b).

recovery of a deformed stamp is nearly instantaneous (< 1 second) upon application of power to the heater. Cooling occurs on the same time scale. The use of NiCr necessitates a "window" design, as shown in Figure 4.4a, where the heater wraps around the periphery of the stamp to allow vision of the stamp during the printing process. This reduces vision of the substrate, and creates hot-spots in the SMP layer directly above the NiCr heater coils, since the temperature there is necessarily greater than the temperature of the stamp. Excessive heating (>275 $^{\circ}\text{C}$, see Appendix A.5) of the SMP can lead to degradation and outgassing, potentially contaminating the opposing substrate and inks with polymeric material. Variability of the position of the stamp within the central window leads to undesirable variability in the final stamp performance for this heater design, as well.

To alleviate these issues, an alternative heater was designed using ITO as a transparent, conductive layer. ITO is more resistive than NiCr, and therefore an appropriate resistance was achieved using a simple straight band design as shown in Figure 4.4b. The band design provides a relatively large area

of uniform heating over which the stamp may be placed, where modest variations in position result in negligible changes in stamp temperature. The ITO layer has greater than 90% visible light transmittance, allowing for a clear view of the printing process. These heaters were used in conjunction with advanced SMP stamp designs to fabricate several silicon microstructures in Reference [194]. The demonstrations highlight the advantages offered by the SMP stamps regarding adhesive strength, reversibility, and the time-insensitive nature of the release mechanism. Though impressive, these structures represent only basic examples of new ink and substrate geometries which may be assembled by using shape memory polymers.

The most direct and obvious benefits of an SMP-based approach to transfer printing have been thus far described. A single-unit method of printing inks is, however, only suitable for production of very small numbers of devices. Commercial production of many thousands or millions of devices require greater throughput. For this reason, the ability to manipulate many inks in parallel is explored in the following section where it is again shown that the unique material properties of the chosen SMP may be used to excellent effect, enabling rapid and reliable transfer of arbitrary ink patterns across a two-dimensional array.

4.2 Multi-Unit Transfer Printing Using SMP

A multi-unit printing process entails the transfer of two or more inks during the course of a single printing cycle, beginning with the lifting of the inks from their donor substrate. The goal of such a scheme is to improve throughput, which may be increased by a factor equal to the number of inks printed per cycle in an efficient process. In the most basic multi-unit printing process, an array of inks is retrieved and printed together in a pattern determined by the physical configurations of the stamp and substrates. This method will be referred to as parallel printing, and is well suited for large scale manufacture where ordered arrays of inks are simultaneously printed in a pre-defined format. A fundamental drawback to this method of printing is its intolerance of defects in the printing process due to missed retrievals, missed prints, or defects in the inks themselves. The process also necessitates the production of a unique stamp and/or ink pattern for every variation of desired print. In addition, retaining precise registration of inks during a parallel print process is difficult and requires special consideration when using an easily-deformable elastomeric stamp [202].

A more general and powerful method combines the ability to print several inks in a single cycle, but selectively such that the transferred pattern may be determined uniquely for each cycle. A print cycle will generally proceed as follows: inks are first retrieved in an array, as with parallel-printing, and for each ink that is to be printed the stamp is activated, thus preparing that ink to be printed while retaining all non-activated inks during the print cycle. With elastomer-based stamps, for which adhesive control is based on time-sensitive kinetics, realization of this printing method requires an addressable system of physically actuating the stamp. Two examples have been previously published: a pneumatic method in which pressurized air inflates the stamp beneath each ink to be printed [190], and a lead zirconate titanate (PZT)-based method in which each ink site on the PDMS stamp may be vertically actuated a short distance [203]. These methods were demonstrated using one-dimensional arrays of PDMS posts, where between four and six inks could be retrieved in parallel and selectively printed. These represent valuable proof of concepts, although each method has drawbacks concerning packing density and ease of manufacturing the stamps. In the case of pneumatic actuation, the space required to run air lines to each actuation site through the stamp limits the practicality of working with two-dimensional arrays. PZT-based solutions require significant external space for electrical leads and connections, while each actuating cantilever must be of significant length to enable the necessary vertical travel distance, again limiting practical use to one or perhaps two rows of inks simultaneously.

In this section I present a method of achieving selective-printing in a large 2D array format, with little fundamental restriction on ink packing density and a high speed of activation. The method is made possible by the use of an SMP as the functional stamp material. NGDE2 remains the SMP of choice for this application (see Appendix A.1). Its narrow glass transition region near but above room temperature enables rapid thermal activation of the SMP, requires only passive cooling, and minimizes the negative effects of temperature rise in the system including possible damage to inks and thermal expansion of the stamp and surrounding structures. The resistive heaters presented in Section 4.1.3 are effective for use in single-unit print systems, but present several issues when applied to multi-print systems. Since the resistive elements must generally be placed some distance from the active SMP interface, localizing heat to activate one stamp without affecting its neighbors becomes problematic, thereby negatively impacting stamp and ink packing density. Though this issue may be alleviated to some extent through

careful system design and fabrication, integrating addressable resistive elements as part of the stamp array necessarily increases the complexity and cost of their fabrication and use. This is particularly undesirable for a manufacturing process in which the stamps may need to be replaced in the event of damage, or may need to be exchanged between steps in the process to print differently configured inks.

The solution demonstrated here is to locally heat SMP stamps using near infrared (NIR) laser illumination to deliver the heating necessary for stamp activation, and thus selective-printing of inks. The SMP is highly transparent to the portion of the NIR spectrum used in the present study (peak 807 nm wavelength) and so absorption is handled by embedding carbon black particles within the stamp surface near to where it contacts the ink, forming a composite carbon black-SMP (CBSMP). Carbon black (see Appendix A.3) is chosen as the absorbing agent due to its strong NIR absorption, and its common use as an additive in polymer composites [204]–[206]. Absorbing the laser energy within the stamp enables operation irrespective of ink material and geometry, and ensures that heat is confined to the desired active regions of the stamp. Laser-assisted printing has been previously demonstrated for a PDMS-based single-unit print system [189], [207], [208]. The operating principle of this previous work is fundamentally different from the present SMP-based system[207][206][207][200][201][200][201][200][201][200]. The ink release in the PDMS-based system relies on high-intensity (3 to 30 W mm⁻²) laser illumination which is absorbed by the ink to briefly heat the surface of the stamp to very high temperatures (350 °C to 600 °C), inducing rapid thermal expansion within the stamp to rapidly propagate stamp-ink interfacial cracks. The present SMP-based system, in contrast, does not rely on NIR-absorbing ink material, operates within a relatively mild temperature range (60 °C to 120 °C) thus protecting both stamp and ink, and in general is insensitive to heating rate allowing for greatly reduced laser power (~0.3 W mm⁻²).

4.2.1 Design and Fabrication of Laser-Activated CBSMP Print System

Figure 4.5 depicts the configuration of and fabrication process for a microstructured CBSMP stamp array. Full fabrication details are provided in Appendix C.1. The CBSMP stamps possess a

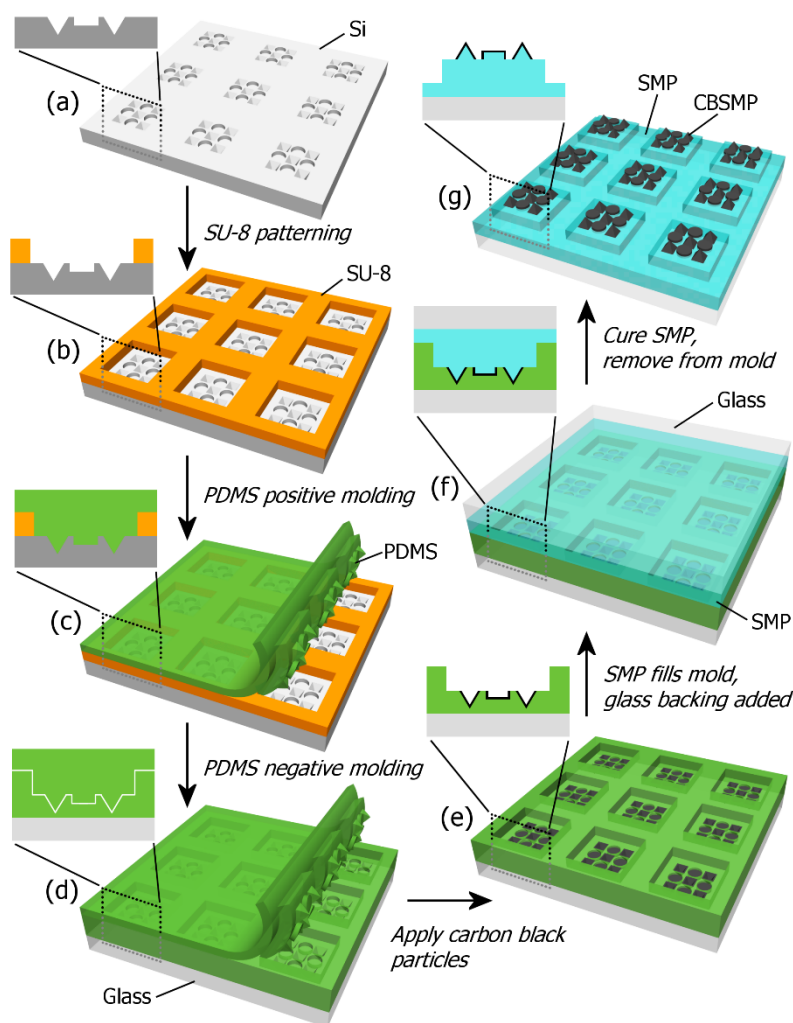


Figure 4.5 – Manufacture of CBSMP composite stamps. Drum and microtip pits are etched in silicon (a), and the stamp edges defined by patterned SU-8 photoresist to complete the negative silicon/SU-8 mold. Two PDMS castings produce a negative PDMS mold (c,d), which is then selectively filled with carbon black particles (e). SMP precursor poured into the mold, covered with glass (f), is cured and removed to form the final stamp array (g).

microstructuring similar to the single-unit stamps presented in Section 4.1, but with the addition of raised cylinders termed "drums," which provide a flat adhesive surface to firmly bond to the ink when the stamp is in its adhesion-on state. These microstructures provide a simple means to deposit NIR-absorbing carbon black within the discrete regions of the stamp which require heating, while maintaining optical transparency through the rest of the stamp to aid observation of the printing process. The microtips are sized to allow delamination from the ink surface upon heating, while drums are sized to balance visibility between the opaque microstructures with adhesive area.

The full selective-print cycle is shown in Figure 4.6 for a 3x3 ink array. The microstructuring serves the dual purpose of providing a controllable means of adhesion reversal, and a means of localizing NIR-absorbing carbon particles within the principally deformed region of the stamp without significantly impeding visibility through the stamp. First, a stamp is positioned above an ink array (Figure 4.6a). The stamp is simultaneously heated via an attached resistive heat source and each microstructured post is deformed to its adhesion-on state by pressing it against the inks (Figure 4.6b). The stamps are then cooled to fix their shapes, and retrieval is achieved (Figure 4.6c). After positioning the inks above the receiving substrate (Figure 4.6d), a brief laser pulse is directed locally to the stamp directly attached to an individual ink (Figure 4.6e). The laser illumination is absorbed by the CBSMP, heating it and adjacent SMP to initiate shape reconstitution to its original adhesion-off state. This step is repeated for each ink to be printed (Figure 4.6f) and then brought to contact with the receiving substrate (Figure 4.6g) before retracting to leave the desired ink pattern (Figure 4.6h). Insets in Figures 4.9c,f highlight two stamps which represent adhesion-on and adhesion-off states with different ink-stamp interfacial contact areas. Scanning electron microscope (SEM) images of a representative CBSMP stamp array are shown in Figure 4.7. A stamp is shown in its adhesion-on state in Figure 4.7d-g, including images with a 3 μm -thick, 500 μm square silicon ink attached corresponding to the step in Figure 4.6c, and with the

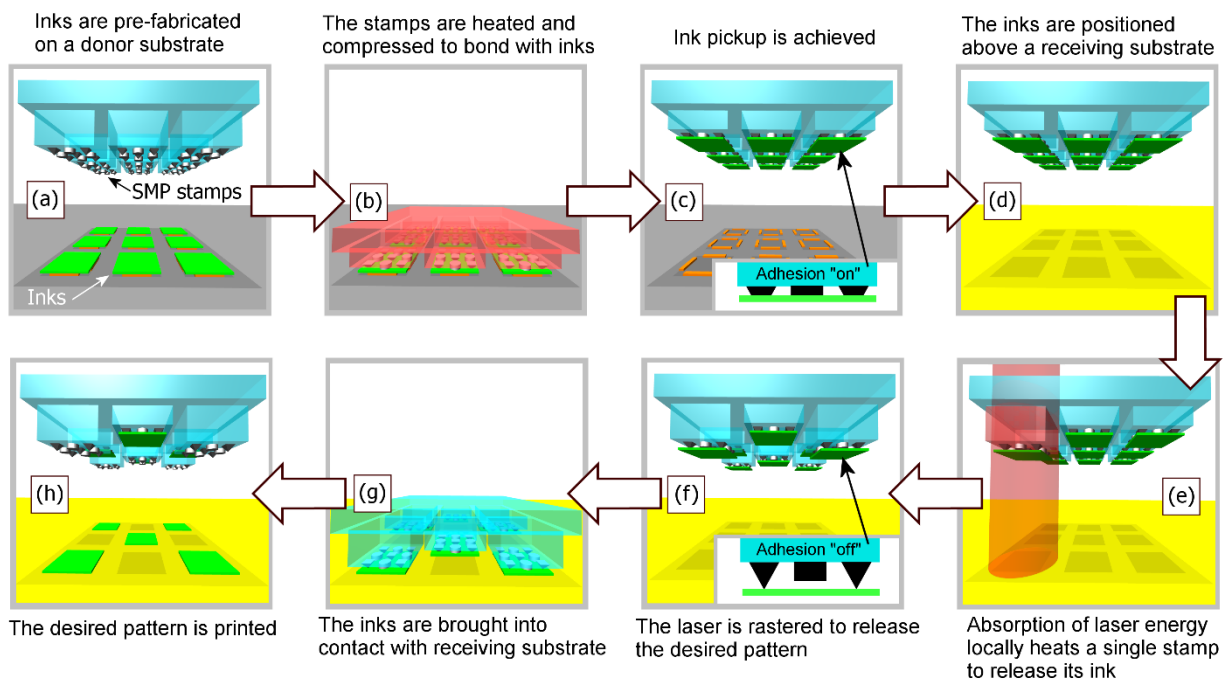


Figure 4.6 – The operation of the laser-driven CBSMP printing process is depicted.

ink removed to show the fixed, deformed shape of the microstructures. A stamp is also shown with a silicon ink attached to the stamp in its ready-to-print configuration in Figure 4.7c, corresponding to the step in Figure 4.6f.

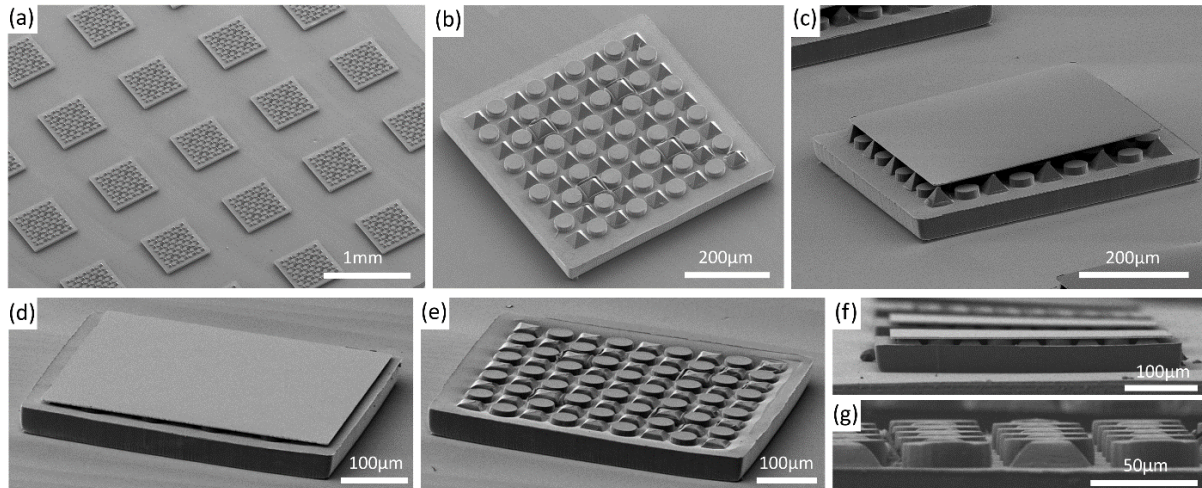


Figure 4.7 – CBSMP stamps are shown in an array (a), and in detail (b). A 3 μm -thick silicon ink is shown on a stamp, after thermally-induced SMP shape reconstitution (c). A stamp is shown in its adhesion on state with an ink attached (d), and with the ink removed (e). Side-views are shown in (f) and (g).

4.2.2 Modeling and Characterization

The transfer printing machine used for this work is depicted in Figure 4.8, and includes an integrated laser source. The equipment was previously described, and is used with trivial modification from this prior description [207]. Power delivery to the CBSMP during an incident laser pulse is a function of the laser's intensity and the absorbance of the CBSMP material. Measuring the proportion of incident laser power absorbed by the CBSMP structures is therefore essential to properly predict the response of the stamps under laser illumination. This measurement is performed using a photo-diode power meter (Thorlabs S142C). Arrays of microtips and drums are fabricated out of SMP with and without the added CB. In both cases, the microstructures are formed onto the surface of a thin (50 to 100 μm) SMP layer. Much of the light passing through the microstructures is refracted in various directions, particularly in the case of the microtips where nearly all incident light is refracted away from the original beam path. To measure the proportion absorbed, this refracted light must be collected. This is accomplished by lowering the SMP samples slightly into the integrating sphere detector as depicted in Figure 4.8b, such

that the great majority of refracted light remains within the sphere. Further experimental details are provided in Appendix C.3.

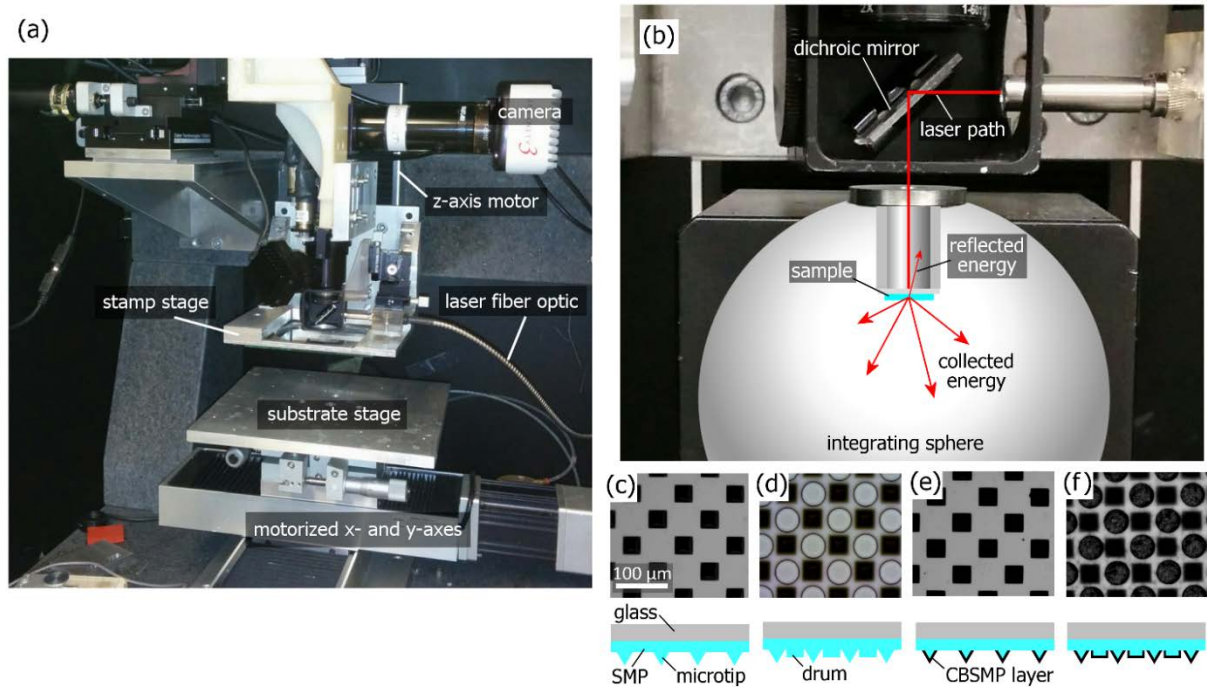


Figure 4.8 – The automated micro-transfer printer used for performance and demonstration of the CBSMP laser-driven printing system (a). Laser absorption measurements were made using an integrating sphere power sensor (b). The laser power transmitted through a baseline glass sample was compared with that for SMP microtips (c), SMP microtips with drums (d), CBSMP microtips (e), and CBSMP microtips with drums (f). Images (c) through (f) share a common scale.

Six separate sample configurations were prepared, each being tested at three distinct locations to ensure repeatability. The stamps exist as a thin layer mounted on a 1 mm thick piece of plain microscope glass. Therefore, the attenuation of the other samples is measured against the power transmitted through a similar piece of glass. The power attenuated by a featureless, thin layer of SMP is additionally tested and was found to be approximately 1%. The other four samples consist of: plain SMP with microtips only (Figure 4.8c), plain SMP with microtips and drums (Figure 4.8d), CBSMP with microtips only (Figure 4.8e), and CBSMP with microtips and drums (Figure 4.8f). The projection area of the microtips and drums in the beam path are calculated to be 25% and 33% of the total area, respectively. Attenuation for each sample relative to the glass-only baseline sample is calculated by comparing the detectable power transmitted through each sample from an incident beam of constant intensity. Results are shown in Table 4.2. The small degree of attenuation with the regular SMP samples indicates nearly all of the

light incident on the microstructures passes through with little absorption. The minor attenuation measured is likely due in small part to absorption within the SMP, and in larger part to internal reflections and refractions within the microtips which direct some energy back out of the detector. For CBSMP samples the attenuation increases to be approximately equal to the projection area of the CBSMP microstructures. The minor discrepancy is likely attributable to the scattered presence of CB particles between microstructures, since energy entering the microstructures is anticipated to be absorbed leaving little to be reflected upwards. The conclusion from these experiments is that essentially all of the NIR illumination incident on the CBSMP microstructures is absorbed by the embedded CB particles, thus providing the heat necessary for the SMP's function.

Table 4.2 - Results of absorption testing, showing the effectiveness of the CB for absorbing NIR laser energy.

Sample Type	Transmitted Power [mW]	total % attenuation	microtip area	drum area	total structure area	% attenuation attributed to CB in microstructures
Glass slide	208	---	---	---	---	---
Flat SMP	206	1%	---	---	---	---
Microtips only	202	3%	25%	---	25%	---
Microtips & drums	202	3%	25%	33%	58%	---
CB Microtips only	149	28%	25%	---	25%	25%
CB Microtips & drums	80	61%	25%	33%	58%	58%

A symmetry-based thermal finite element model (FEM) is developed to understand the thermal behavior within the SMP during and following laser illumination using Comsol Multiphysics, shown in Figure 4.9a. It is of particular interest to know the power required to adequately heat the deformed SMP, the speed at which this heating occurs, and assuring that heat is distributed adequately to effect the necessary shape reconstitution throughout the stamp while avoiding hot spots which could lead to thermal degradation. During fabrication, CB particles are concentrated near to the PDMS mold surface as the SMP precursor is poured in. Though some degree of mixing with the precursor occurs, the distribution of CB is not uniform throughout the microstructures and is instead more heavily

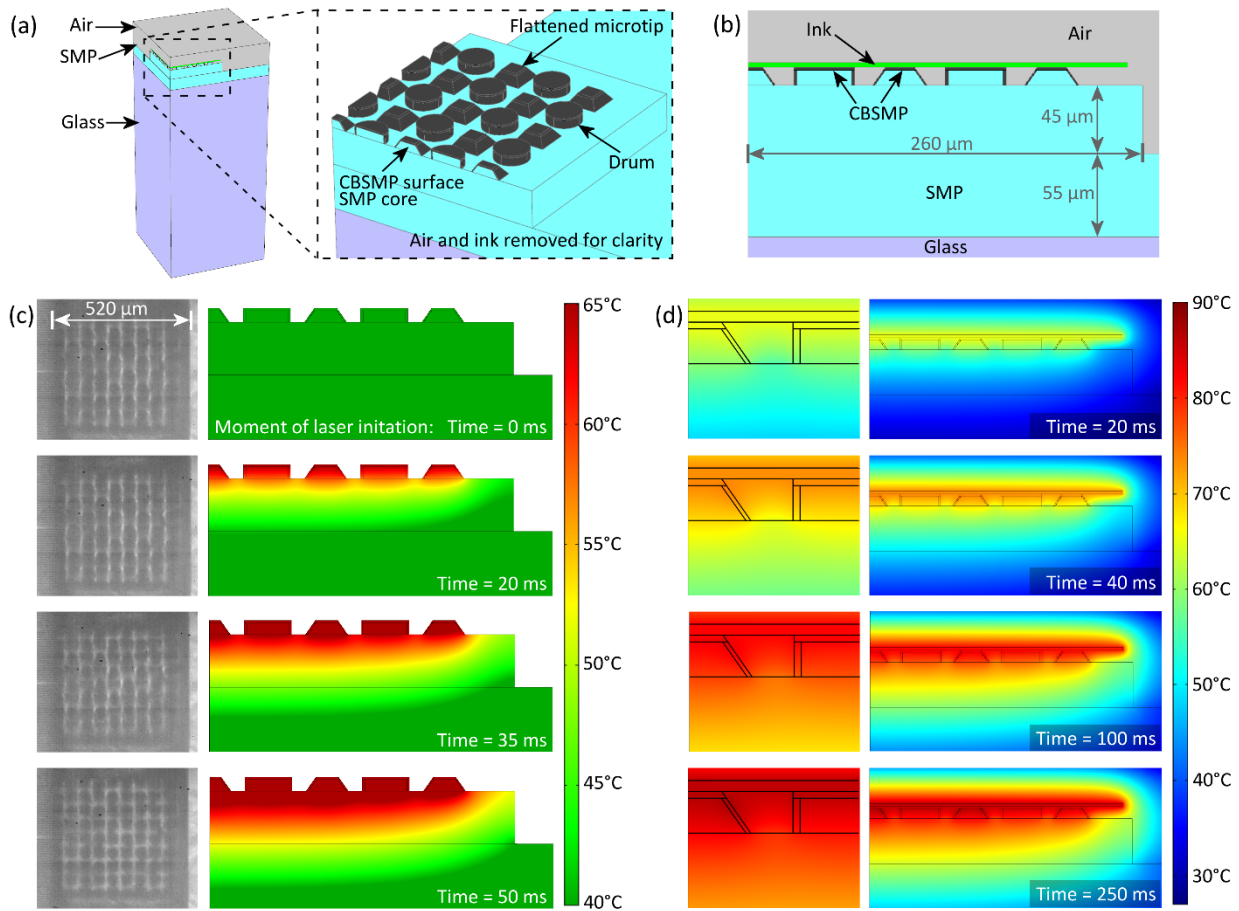


Figure 4.9. A symmetry-based 3D finite element model is developed, with laser absorption occurring within a thin 2 μm CBSMP layer (a). A 2D cross sectional view is shown in (b). High-speed footage of the CBSMP stamp during continuous laser illumination is compared with the corresponding FEA temperature profile in (c) for times counting from the moment of laser initiation. The temperature profile in the stamp/ink system during a print is predicted in (d), including detail of the central microstructures.

concentrated near to the surface. The nature of CB particle distribution was investigated by using an oxygen plasma to etch away the surface of a stamp in stages, revealing the changes in light transmission as material was removed. Representative images are shown in Figure 4.10, where light transmission through the drums is shown to increase as embedded CB particles are removed along with SMP matrix. As expected, the CB concentration is greatest close to the surface and gradually tapers for several microns into the stamp. To represent this CB distribution appropriately with regard to simulation of surface hot-spots, a 2 μm absorption layer was incorporated in the FEM.

A side-view, corresponding to a cross section through the center-line of the stamp, is shown in Figure 4.9b. Heat generation rates within the CBSMP layer are calculated based on the data shown in Table

4.2 indicating that virtually 100% of the incident laser energy is absorbed while passing through the microstructures. The thermal properties of the particular SMP in use have not been thoroughly investigated, although it is reasonable to expect close agreement with other similarly structured epoxy-based polymers which have been more extensively studied [209]. Polycarbonate is found to be a well-defined material which very closely matches the thermal properties for similar epoxy polymers, and is therefore used to represent SMP in the Comsol models.

High speed images of a CBSMP stamp undergoing laser-driven shape reconstitution to release a 3 μm thick silicon ink are compared with FEM results in Figure 4.9c. The results were obtained using a beam power of 93 mW, corresponding to an intensity of 330 mW mm⁻² for the 600 μm diameter beam. Times listed in Figure 4.9c,d count up from the initiation of the NIR laser illumination. The high speed images are taken looking down through the stamp during the event using a Phantom v7.3 camera, and show within the stamp edges a 9×9 grid of deformed drums and microtips which appear as dark spots, reconstituting their shape as their temperature increases. The reconstitution is visible as a subtle change in the microstructures' appearance from somewhat blurred together in their initial, compressed state, to

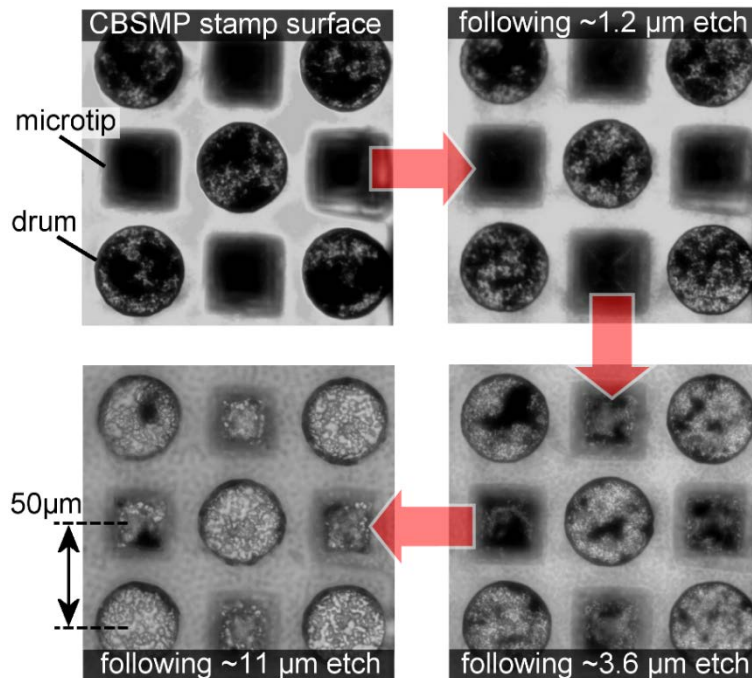


Figure 4.10. Optical transmission images indicating the extent of surface concentration of CB within the SMP microstructures as the surface material is etched away in stages. Extended etching produces noticeable surface roughness.

fully distinct features at 50 ms. Corresponding FEM results are collected using the full model as shown in Figure 4.9b, but only the temperatures for the SMP material are shown for clarity. Heat generation within the Si ink is calculated based on previously published absorption data, collected with the same laser printing system used in the present work, showing a silicon ink of 3 μm thickness experiences a power density of $5 \times 10^{11} \text{ W m}^{-3}$ for a laser input power of 3.268 W [208]. From this, a linear relationship is derived in which power absorption within the silicon ink is $1.53 \times 10^{11} \text{ W m}^{-3}$ per 1 W of incident laser power. The energy first absorbed by the CBSMP features is accounted for when calculating incident laser power on the ink. The color bar corresponds to the glass transition of the SMP to illustrate the regions of the SMP stamp which are hot enough to undergo shape reconstitution. Note that the initial temperature of the system is 27 $^{\circ}\text{C}$, which is below the range of this temperature scale. A temperature below 40 $^{\circ}\text{C}$ indicates an SMP region which remains fixed in its deformed configuration, whereas the shape recovery becomes increasingly rapid and thorough as the temperature is increased through 65 $^{\circ}\text{C}$.

The mechanical behavior of the SMP changes dramatically in relation to its local temperature as it passes through its glass transition. Storage and loss moduli for NGDE2 have been previously calculated for the SMP as functions of temperature in ref. [210]. Subsequent analysis presented in Section 5.2.2 confirmed these results and investigated the effects of large CB particle loading. Both data sets show a dramatic peak in loss modulus (indicated by $\tan \delta$) within the glass transition zone between approximately 40 $^{\circ}\text{C}$ and 65 $^{\circ}\text{C}$. Below this temperature range, the storage modulus (E') is $\sim 3 \text{ GPa}$, and above it $E' \approx 9 \text{ MPa}$. Reconstitution does not occur as rapidly as would be expected for an elastic material suddenly allowed to spring back from a compressed shape, but rather exhibits a short but noticeable time lag as it passes through the SMP's glass transition due to the viscous nature of the SMP, as evidenced by the characteristic sharp increase in loss modulus. Once temperatures reach the upper end of the glass transition the viscous nature of the response is significantly reduced and reconstitution occurs with greater rapidity and completeness. Mechanical response time is therefore strongly a function of the local temperature within the SMP's deformed structures. Reconstitution times below 50 ms have been observed for a modest 93 mW beam power. For the present purposes of conceptual demonstration, this is considered sufficiently rapid, and does not result in stamp damage even during extended pulses. Increased speed may be realized with higher beam power levels which would require

increased control over pulse duration to avoid overheating, which I observed as outgassing of the SMP material during extended pulses when beam power is in excess of 200 mW.

FEM results are provided for the same test configuration but with a full temperature scale and for longer pulse duration in Figure 4.9d. Thermogravimetric analysis of the SMP indicates significant material decomposition occurs once heated above approximately 275 °C (see Appendix A.5). It is therefore desirable to keep the local temperature well below this limit during operation. Examination of the thermal gradients within the model depicted in Figure 4.9d indicates adequate heat diffusion within the stamp to prevent excessive temperature for the power levels under consideration. Stronger power intensity can potentially improve printing speed as greater throughput is demanded.

Many factors affect the thermal behavior during a print cycle. Since a primary advantage of our CBSMP system over other laser-based transfer printing systems is its versatility with regard to the type of ink which may be printed, the thermal effects of changing ink material and geometry are of particular interest. Gold is frequently utilized in functional MEMS devices as an electrical contact surface or interfacial bond-facilitating layer, among other uses. Even thin layers of gold are highly reflective to NIR radiation [211], preventing their use in laser-based printing approaches which rely on NIR absorption within the ink material. The effect of a perfectly reflective thin gold coating is simulated and shown in Figure 4.11a, 100 ms into the laser illumination. Due to the reduced energy absorbed in the system, overall temperature decreases when compared to a similar simulation with the absorbing silicon ink. This can be effectively compensated for by modestly increasing the power input without negatively impacting temperature distribution (Figure 4.11b). The gold-coated silicon ink represents any class of thermally conductive, non-absorbing ink used in the CBSMP system. Increasing the thermal mass of the ink is investigated by increasing the thickness of ink in Figure 4.11c from 3 μm to 20 μm . Temperatures experience a modest decrease, which again may be easily compensated for with an increase in power. Although silicon remains a common standard ink material, many ink materials of interest are not thermally conductive. The effect of using a low-conductivity and non-absorbing ink is shown in Figure 4.11d, using Poly(methyl methacrylate) (PMMA) as an example material. The results demonstrate that a highly conductive ink is advantageous with regard to distributing heat across the surface of the stamp, although the less conductive ink still allows for adequate heat distribution to allow

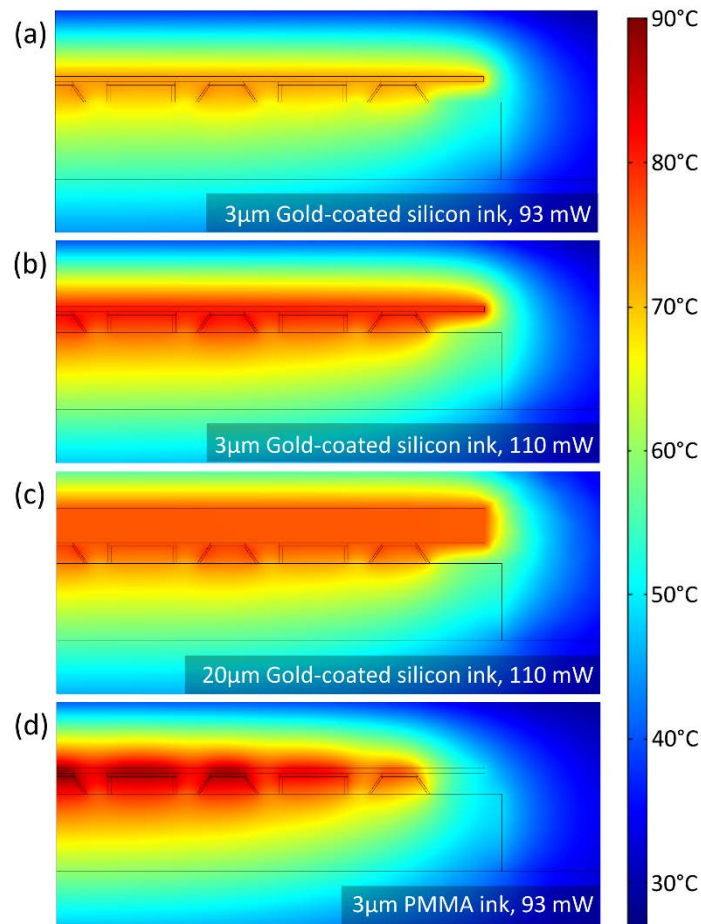


Figure 4.11 – Results at 100ms into the transient event are shown for several cases of interest, including a thermally conductive non-absorbing ink (a), the same ink with increased power (b), a thicker thermally conductive non-absorbing ink (c), and a low-conductivity, non-absorbing ink (d).

printing to occur. The intensity of localized hot spots within the CBSMP microstructures increase modestly, thus modestly reducing the maximum rate of safe power delivery and resulting in a corresponding modest increase in print time for a highly-optimized process.

Printing in the general case is carried out as depicted in Figure 4.6. A set of inks is retrieved from a donor substrate by a matching array of stamps, from which a pattern is printed in parallel to a receiving substrate. For the purposes of demonstration, a 5x5 array of stamps is used to retrieve and print silicon inks with 500 μm lateral dimension and 3 μm thickness. These inks are fabricated with center-to-center spacing of 1 mm. These dimensions were chosen for compatibility with the installed laser optics on the micro-transfer printer depicted in Figure 4.8, but may be scaled up or down by adjusting the laser spot size.

4.2.3 Printing Demonstrations

A first demonstration is shown in Figure 4.12, spelling the Department of Mechanical Science and Engineering acronym, MECHSE, with gold-coated silicon inks on a flexible PDMS substrate which is placed on a curved glass surface. The gold coating is approximately 100 nm in thickness and causes near total reflection of the NIR laser, thus providing an example of a printing task with a non-absorbing ink. Ink fabrication details are provided in Appendix C.2. The printing task is completed using a combination of parallel and serial printing, resulting in six letters printed using five sets of retrieved inks. This is clarified in Figure 4.12, where the first three parallel prints are represented in a diagram. Printing "M" requires using inks from every column, thus the inks are replenished before the next step. However, the letter "E" only requires four columns of inks. Repositioning the stamp over the substrate allows the final column of unused inks to be printed as the first column of the letter "C," thus completing the second of two parallel prints from one set of inks. This method conserves inks when compared to a purely parallel print method where unused inks are discarded. A significant time savings is also realized by reducing the number of pickup steps since a significant portion of a typical process cycle is used to transition between pickup and printing of the ink arrays. Serial printing is not limited to column-by-

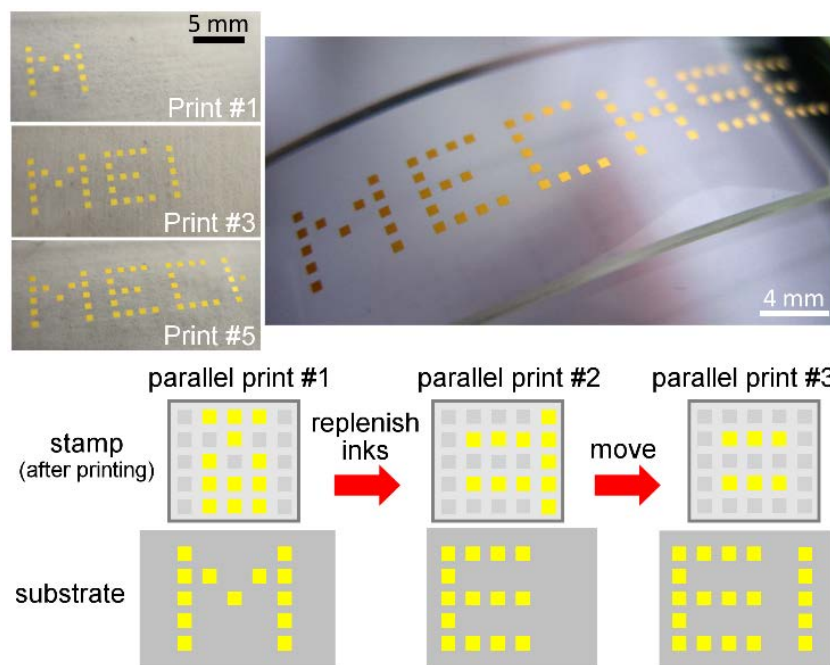


Figure 4.12 – A 5x5 array of CBSMP stamps are used to print “MECHSE” on a PDMS substrate with gold-coated Si inks using multiple parallel printing steps. The first three prints are clarified with a diagram. The PDMS substrate is conformed to a curved surface.

column print tasks. An example of a purely serial printing process is depicted in Figure 4.13a. Silicon inks with an initial edge-to-edge spacing of $500\text{ }\mu\text{m}$ are first shown attached to the CBSMP stamp array. Each ink is then printed in series while registering the receiving substrate to reduce the spacing to $100\text{ }\mu\text{m}$, as shown. A well designed industrial process utilizing a selective array-based transfer printing approach such the one presented here would most likely incorporate both serial and parallel elements. Multiple prints may be made over the same space of the receiving substrate. The University of Illinois Urbana-Champaign acronym, "UIUC," is printed with silicon inks on a PDMS receiving substrate using three parallel prints in Figure 4.13b. Also depicted is the stamp array following one of the parallel prints. The inks are bright and reflective, while the locations of the missing printed inks are dark due to the

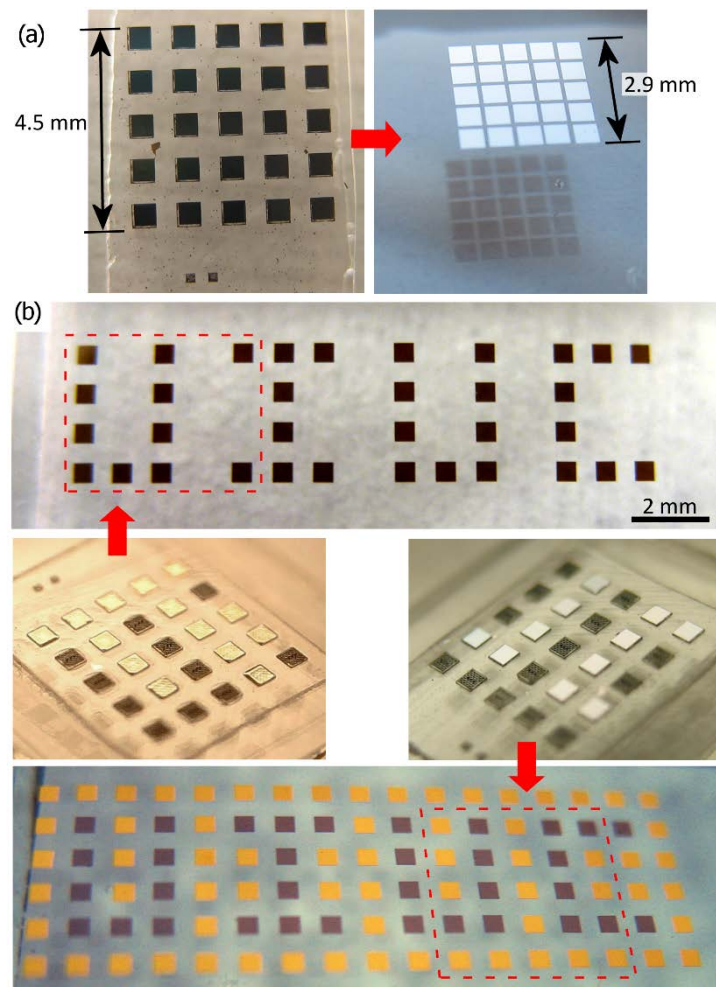


Figure 4.13. - Inks are printed individually in sequence to reduce ink spacing from $500\text{ }\mu\text{m}$ on the stamp array to $100\text{ }\mu\text{m}$ on the receiving substrate (a). "UIUC" is printed with Si inks via three parallel print steps to a PDMS substrate (b). Gold-coated Si inks are then printed utilizing both parallel and individual print methods to surround the original design.

CBSMP microstructures. The stamp array images are flipped horizontally to ease understanding. The printed pattern does not interfere with a second overlaid print task, in this case a surrounding arrangement of gold-coated silicon inks. These inks are printed using four 5×5 sets of inks using a combination of parallel and serial printing.

Much of the interest in transfer printing relates to the ability to assembly structures on semiconductor substrates. These substrates provide a particular challenge, due to the low surface adhesion they provide to aid ink release. The laser-driven CBSMP system is capable of selectively printing inks on these surfaces, with a few examples shown in Figure 4.14. The letters "UC" are printed as two separate print cycles, shown after thermally annealing at 900 °C to improve the ink-substrate bond. Multiple SEM

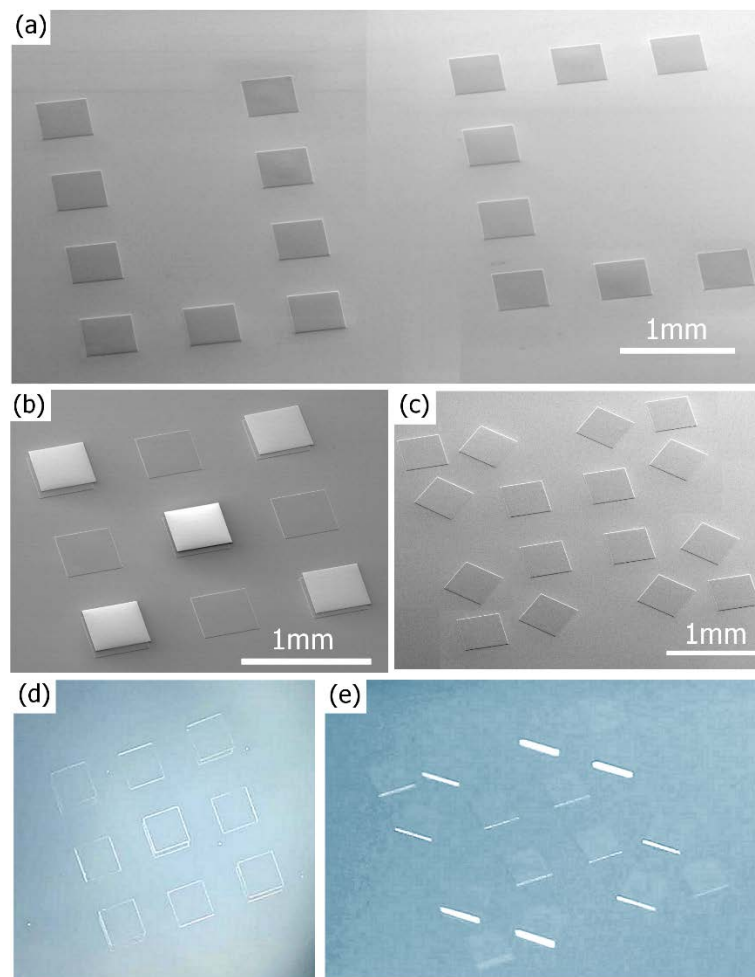


Figure 4.14 – The letters “UC” are printed in Si inks on a silicon substrate (a). A second layer of Si inks is printed on a first layer of Si inks (b). A 4x4 array of Si inks are printed in two parallel print steps, with a 45 degree rotation between them (c). Optical images of the demonstrations in (b) and (c) are shown in (d) and (e), respectively.

images are stitched together due to the size of the pattern in Figure 4.14a. Forming functional MEMS structures typically involves stacking more than one layer of inks. This is demonstrated in Figure 4.14b with a simple cross pattern printed on an initial 3×3 array of inks. A final demonstration of printing on silicon is shown in Figure 4.14c. A 4×4 array of inks is used to first print a pattern of eight inks as one parallel step, then the substrate is rotated 45 degrees to print the remaining inks also in parallel. Optical photographs are included in Figures 4.14d,e, demonstrating the bare silicon surfaces of both ink and substrate. The ability to overlay printed patterns on silicon is therefore demonstrated, as well as the ability to incorporate rotations into an assembly process utilizing a combination of parallel and serial printing elements.

The preceding examples demonstrated printing 3 μm -thick silicon inks on silicon and PDMS substrates, which comprises the scope of the current work. Previous publications utilizing microtip-based PDMS stamps demonstrate its capabilities for printing semiconductor inks with thicknesses ranging from 300 nm to 20 μm [212]–[214]. The operating principle of the microtip design requires the ink to be sufficiently stiff in bending such that the reconstitution of the microtips delaminates the ink from the intermediate regions, which are comprised of the drums in this work. For this reason, the microtip geometry reported here may not be a suitable choice to print very thin membranes, and particularly when made of very soft materials. This limitation can be mitigated by properly scaling the stamp's microstructures [215], [216]. Thicker inks should suffer no such limitation. Metal-film inks have been successfully printed with microtip PDMS stamps [217], and should be likewise printable with SMP-based stamps although demonstrations have yet to be performed. As described herein, the thermal limitations imposed on inks by the laser-driven CBSMP printing process are modest, only requiring that the ink briefly withstand temperatures of approximately 90 °C. Inks made of very soft materials, and those with very low surface energy, can be expected to pose challenges during retrieval, similarly to other transfer printing methods, which require an extension of the presently developed technique.

Chapter 5. Scaling Up Shape Memory Polymer Dry Adhesives

The successful application of SMP as a dry adhesive in Chapter 4 for microscale transfer printing suggests it may also provide unique benefits for larger, macroscale applications. In this chapter I will describe my efforts to investigate this question, beginning with a series of tests to measure the adhesive performance modestly-sized SMP which retains a reversibility-enhancing microscale structure similar to the one presented in Chapter 4 for the purpose of transfer printing. There, it was stated that the microtips were sized to allow delamination from the ink. In Appendix D.1, the state of stress within the microtips and considerations for proper sizing are considered in some detail.

5.1 SMP as a Reversible Macroscale Dry Adhesive

The macroscale SMP described in this section functions essentially as a much larger version of the transfer printing stamp described in Section 4.1. NGDE2 is again chosen for the SMP. The full bond and release cycle is depicted in Figure 5.1, shown for only a small portion of the larger adhesive. Due to the increased size, cycle time is significantly longer on the order of minutes, and is applied in this case by a custom temperature controlled aluminum-block heater.

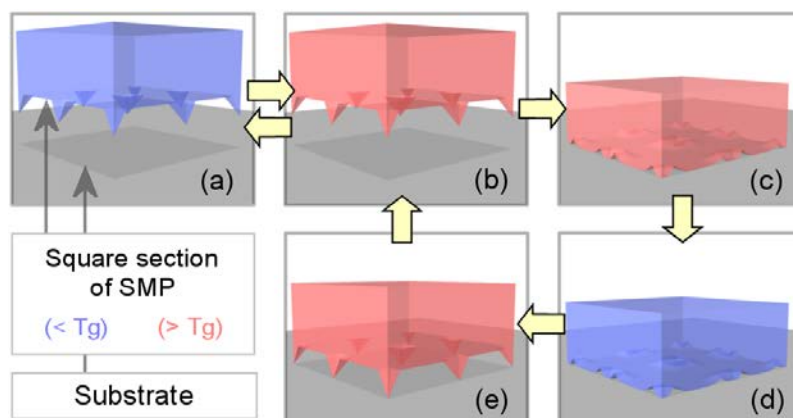


Figure 5.1. (a-e) A schematic illustration of the bonding/debonding between SMP surface and a substrate. (a) A section of SMP with microtips in their permanent shape at temperature ($< T_g$). (b) To begin the bonding process, the SMP is heated above its T_g to become compliant ($> T_g$). (c) Preload is applied to cause the SMP to collapse into contact with the substrate ($> T_g$). (d) The SMP is cooled down to become rigid and bonded to the substrate in this temporary shape ($< T_g$). (e) To reverse the adhesion, the SMP is heated above its T_g and shape recovery causes debonding ($> T_g$).

In order to quantitatively test the adhesive strength and reversibility of a larger-scale dry adhesive, SMP dry adhesives with circular adhesive surfaces, 0.25 inch (6.35 mm) diameter, were prepared by first curing the SMP atop a silicon mold prepared as described in Appendix D.2. In order to apply force in compression and tension for bonding and failure testing, respectively, cylindrical aluminum "sample holders" of 0.375 inch length were made. Each segment then had a 0.125 inch diameter cross hole drilled through it. The unpatterned face of each cylindrical SMP sample is glued to the end of one sample holder using a general purpose epoxy (Figure 5.2). The epoxy is also used to affix a 0.25 inch diameter steel ball bearing to the center of the opposing end of the sample holder to ensure compressive weight applied to the sample during bonding acts through the adhesive's center.

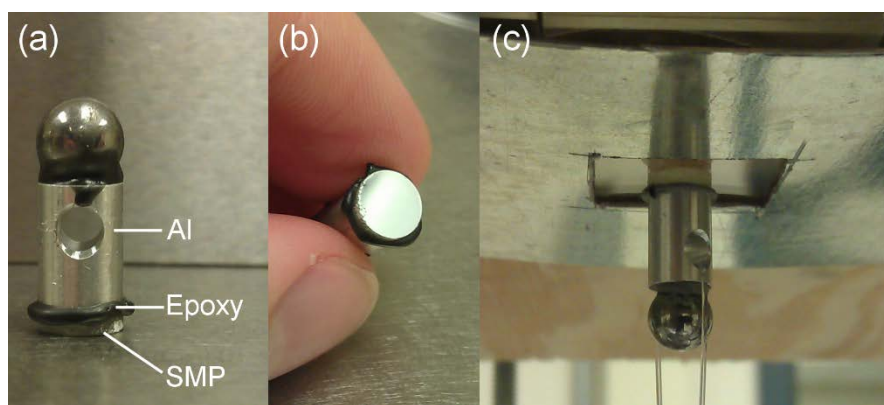


Figure 5.2. (a) An example of an SMP adhesive bonded to an aluminum cylinder with epoxy for handling purposes. (b) The adhesive face of the SMP with microtip pattern. (c) SMP bonded to a glass surface during an adhesion test with weight applied via string fed through the hole in the aluminum.

The glass slide with bonded SMP sample are placed in a custom apparatus so that the glass slide is held in place with the SMP-to-glass interface parallel to the ground and with the SMP sample pointing downwards. A container hangs from the cross hole in the SMP sample holder, placing a small initial load ($< 20 \text{ N cm}^{-2}$) on the adhesive interface. A small water pump is used to gradually fill the container with water at a rate of 12 mL s^{-1} , increasing the load on the SMP-to-glass adhesive interface at a rate of $0.37 \text{ N cm}^{-2} \text{ s}^{-1}$, until failure of the SMP-to-glass bond. The flow of water is stopped, and the adhesive strength is indicated by the combined weight hanging from the SMP sample at the time of failure.

5.1.1 Observations Particular to the Sample Geometry

The backside of our SMP surfaces are bonded to aluminum holders of the same diameter (0.25 inch) in order to apply tensile load during the adhesion testing. As temperature is increased, the SMP expands much more than the aluminum due to the thermal expansion coefficient mismatch, and so the free face of the SMP becomes subtly convex (the SMP thermal expansion is calculated in Appendix A.8). During bonding, a preload is applied acting through the center of the SMP-substrate interface. This preload will initiate collapse of the microtips as described previously in a process I term “local collapse,” as shown in Figure 5.3.

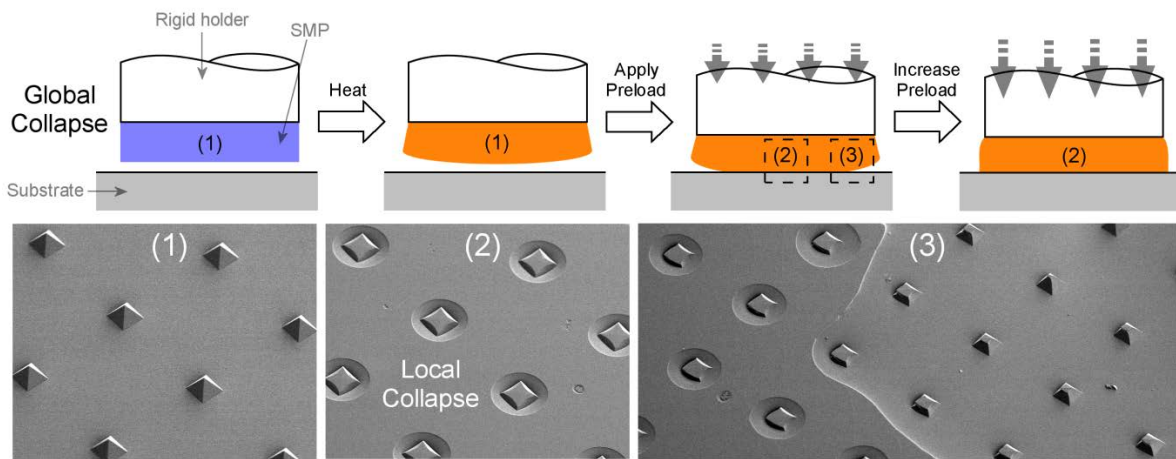


Figure 5.3. Diagram showing the progression of collapse for our particular testing procedure, contrasting global and local collapse.

The process of local collapse to generate adhesion, followed by reconstitution of the original shape to reverse the adhesion, is fundamental to the operation of our reversible dry adhesive. However, local collapse does not occur simultaneously for all regions of the sample surface due to the global curvature of the sample. In general, the central region of a sample will experience local collapse first as a preload is applied. As the preload is increased, the locally collapsed region expands outward toward the sample edges in a process I term "global collapse," also shown in Figure 5.3. Poisson's effect also works to inhibit full collapse by causing outward radial motion of the SMP as preload is increased. The result is that the necessary force to fully bond our SMP adhesives to glass is primarily dictated by global collapse, rather than local collapse. Likewise, the presence of the aluminum holder has an effect on the initial detachment process, which progresses as the reverse of the collapse process. However, it should

be stressed that the aluminum cylinder inclusion is not a prerequisite for detachment. In its absence, bonded microtip SMP can consistently and completely detach from a glass substrate upon heating above approximately 70 °C.

The SMP adhesive layer, referred to as a 'backing layer,' for the gathered data was approximately 4 mm thick. There are a variety of factors to consider when choosing an appropriate thickness, some of them specific to the production and testing methods. A very thin backing layer may increase the force necessary to compress the microtips when compared with a thicker layer. The FEM model described in Appendix D.1 and rough analytical estimates indicate that a backing layer on the order of several hundred microns is sufficient to avoid this issue, and so it was not a concern during the tests. The curvature and distortion due to the bonding process described above is reduced by a thinner backing layer, but with the trade-off that the backing layer becomes less compliant and therefore any imperfections in the surface are more difficult to "flatten out" during bonding. Very thin, high-aspect ratio samples were more prone to warping during our production process (prior to bonding to the aluminum holder), and coupled with the reduced compliance appeared to negatively impact the consistency of adhesion between samples. In addition, it proved difficult to precisely control the thickness of the backing layer, and so choosing a greater thickness reduced the importance of tightly controlling this variable.

On the other hand, thinner backing layers are appealing since an increase in adhesive strength for a well-made and well-bonded adhesive sample with a very thin backing layer should be expected based on the principles of crack propagation by elastic energy release. In addition, by reducing or eliminating the convexity formed during bonding, a very thin backing layer would further highlight the utility of the microtips since release by peeling would become especially difficult without them. Many of the thinner samples (~1 mm) showed excellent adhesive performance, though not noticeably better than the thicker samples. High-quality samples with very thin backing layers may exhibit improved performance.

5.1.2 Demonstrating Adhesive Performance

The adhesive strength and reversibility of the microtip SMP surface to a glass substrate is demonstrated in Figure 5.4. The microtip SMP surface is bonded to a glass-topped 5 kg mass using the process described in Figure 5.1a-d. The SMP-to-glass interface can support the full weight of the 5 kg mass as it is lifted and held, representing an adhesive strength of more than 156 N cm^{-2} . To reverse the adhesion, the load is removed and the SMP heated to 90°C to initiate shape recovery. The adhesion is now essentially zero, as in Figure 5.1e, and the SMP is easily lifted away from the glass surface.

To quantify the adhesion, tests were performed using similarly constructed SMP samples with an aluminum holder. As described above, the bonding of the rigid aluminum to the side opposite to the adhesive interface of the SMP was found to have unintended consequences for the observed collapse behavior. The slight surface convexity observed during bonding contributes to the observed relationship between the preload applied during bonding and the strength of the resulting bond in Figure 5.4d. Adhesive strength increases steadily with increasing bonding preload due to the progressive radially-outward collapse of the inter-microtip regions of the SMP to the substrate. As preload approaches approximately 30 N cm^{-2} , all inter-tip regions are in contact with the substrate and further increases in bonding pressure yield no measureable increase in adhesion because gains in contact area become

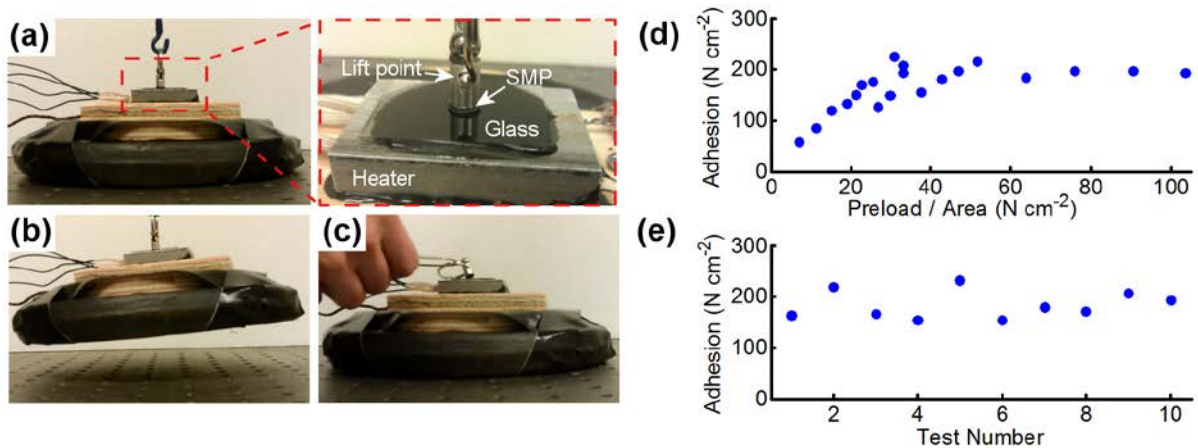


Figure 5.4. The demonstration of adhesive performance of an SMP microtip surface (diameter: 6.35 mm). (a) SMP is bonded to a glass surface applying preload initially at 90°C (b) 5 kg of mass is lifted by SMP bonded to a glass surface with the contact area of $\sim 3 \times 10^{-5} \text{ m}^2$. (c) Heating to 90°C causes detachment with negligible residual adhesion. (d) Effect of preload on adhesion. (e) 10 consecutive cycling tests of a single SMP microtip surface.

minimal. The magnitude of the preload required to reach this plateau in adhesive strength is expected to depend on the aspect ratio, i.e. the ratio of width to thickness, of the SMP adhesive layer.

The SMP's ability to undergo deformation and recover its original shape repeatedly without deterioration has been demonstrated previously [210]. To test whether its adhesive qualities are similarly robust, a single SMP adhesive was put through 20 bond/debond cycles and then tested to failure 10 consecutive times with results in Figure 5.4e. The tests indicate an average adhesive strength of 184 N cm^{-2} , an exceptionally high adhesive force compared with other macroscale dry adhesives which range from 0.1 to 100 N cm^{-2} , where the upper portion of this range has only been achieved using carbon nanotubes and polymer-based adhesives are generally below 10 N cm^{-2} [218]. Additionally, the adhesive does not show visible signs of degradation with repeated uses. In contrast to the large maximum adhesion strength, the minimum adhesion strength was below the resolution of the available equipment (1 mN). This corresponds to a residual adhesion less than $\sim 3 \times 10^{-3} \text{ N cm}^{-2}$, demonstrating more than four orders of magnitude difference between the adhesion of the temporary and permanent shape states.

5.2 Internally Heated Conductive SMP Dry Adhesives

An obvious drawback to the use of thermosensitive functional materials in a dry adhesive is the necessity of a heat source to cycle between compliant and rigid states. An external heat source constitutes additional equipment cost and reduced flexibility of operation for the adhesive system, making the bonding process more complex and adding thermal mass thus slowing the thermal response time of the functional material with a given power input. In contrast, an internally conductive material would allow the functional material to also act as the heat source by passing current through it. In this section, I describe an epoxy-based SMP dry adhesive system doped with electrically conductive carbon black (CB) to enable internal joule heating, bypassing the operational requirement of a secondary heat source. This approach additionally enables adhesion to non-flat surfaces.

5.2.1 Transmission Line Model (TLM) Measurements of Electrical Conductivity

The preparation of CBSMP blends is described in Appendix E.1. Carbon black is well known as an additive to confer electrical conductivity to polymers [204], [205], [219]. The critical concentration of

CB necessary to enable conductivity in an insulating polymer is called the percolation threshold, and is dependent on a variety of factors, including the type of carbon black used (see Appendix A.3), the polymer chemistry, and the method of mixing. Using the relatively common furnace black variety, the percolation threshold generally occurs at concentrations below 5 wt% [205]. For this reason, electrical characterization of our CBSMP blends begins at 5 wt% CB and extends to 30 wt% CB. The transmission line model (TLM) method is used to characterize the electrical properties [220], with two variations of the contact method used as shown in Figure 5.5. An easy attachment method to one side of a strip of material, leaving the entirety of the opposing face as a continuous adhesive surface, is desirable. The natural choice is to use an electrically conductive copper tape that may be pressed to the surface as the method of creating an electrical contact that will be flexible and removable, yet will remain in place while the adhesive is being handled. TLM measurements using Cu tape as the contact path were difficult with blends below approximately 25 wt% CB due to a large and highly variable contact resistance. This is likely due to an uneven surface distribution of CB in blends with a lower CB concentration, as well as some variation and viscous flow within the Cu tape's conductive sticky layer after application. For this reason, bulk resistivity was calculated using alligator clips squeezing flat steel plates against the CBSMP blend surface as the contact points with which to make TLM resistance measurements, as shown in Figure 5.5a. Surface resistivity of the CBSMP blends to Cu tape could then be more confidently calculated down to 15 wt%, using the configuration shown in Figure 5.5b.

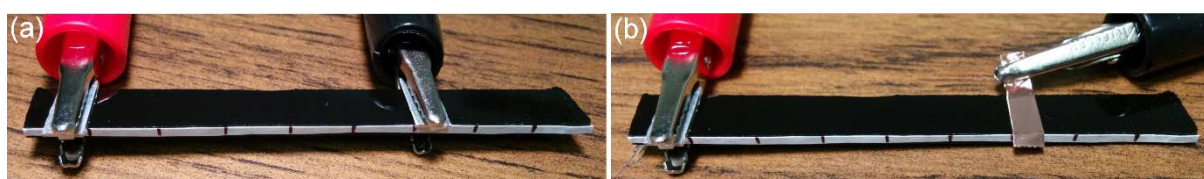


Figure 5.5. Transmission line model (TLM) data is collected using (a) the steel clip method and (b) the Cu tape method. The steel clip method yields more consistent data for mixtures with low weight percentage of carbon black (CB).

TLM measurements were collected at 1 cm increments, stepping along the length of the CBSMP samples which had 2 mm \times 10 mm cross sections, and using steel or Cu tape contact pads that are 5 mm \times 10 mm in area. The data was slightly corrected to minimize the effect of variable contact resistance between contact points prior to the calculation of the least-squares regression line.

Examples of TLM curves for CBSMP blends of 15 and 30 wt% CB are shown in Figure 5.6a for samples with a 20 mm² cross section, with contact pads that are 50 mm² in area. The 15/30 CB composite curve will be addressed later. Above 20 wt% CB, the CBSMP blends become thick, even clumpy, prior to curing and tend to form significant cracks at free surfaces while curing. It has been documented previously for other CB/polymer blends that tensile strength is expected to decrease with increasing CB loading [205], most likely due to internal and surface cracks. Measurements terminate at 30 wt% CB due to the practical challenge of manufacturing and handling continuous bars above this CB concentration. Bulk and contact resistivities are calculated based upon least-squares regression line of the TLM data, together with the sample and contact pad geometries. A greater slope to the regression line indicates a larger bulk resistivity, while a greater y-intercept indicates a larger contact resistance. Performing the similar measurements for several CBSMP blends provides bulk and contact resistivities as a function of CB wt% in Figure 5.6b,c, respectively. The calculation of contact resistivity includes the contribution from bulk resistance beneath the contact pad, and so these values can be considered somewhat conservatively high, though the contribution is not large for the homogeneous samples. As

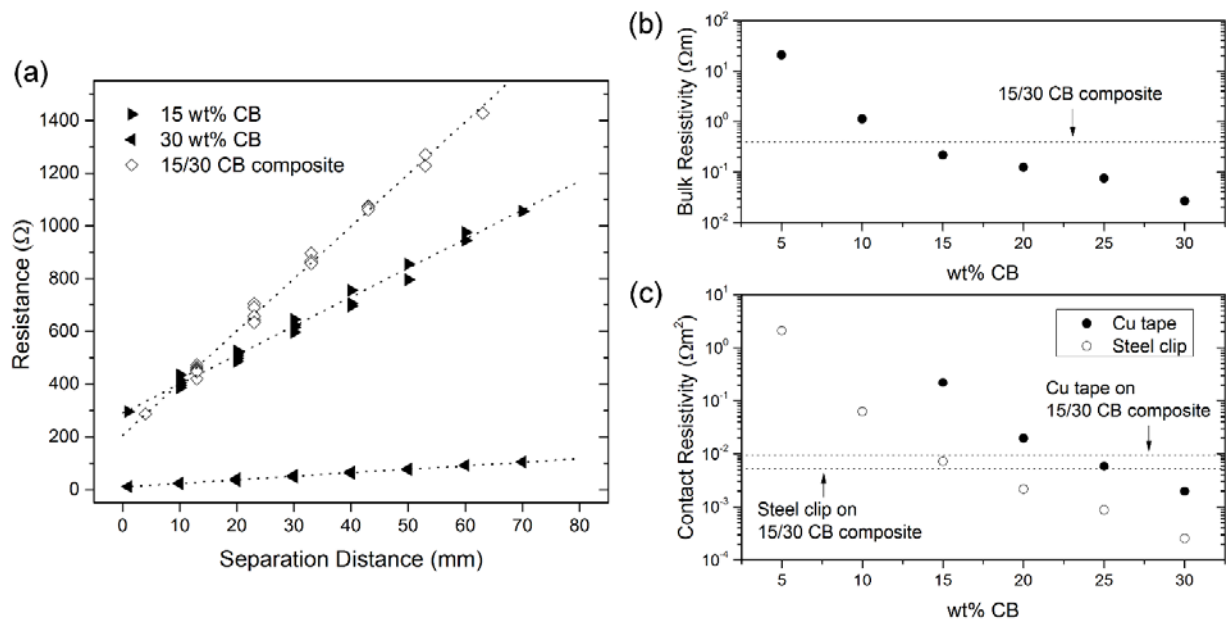


Figure 5.6. (a) TLM data gathered using the steel clip method for homogeneous 15 and 30 wt% CB/shape memory polymer (SMP) blends, and the 15/30 CB composite design. Linear curve fits used to calculate effective bulk and contact resistivities are shown. The 15/30 CB composite has a relatively high effective bulk resistivity (b) and a relatively low effective contact resistance (c), shifting the power dissipation into the bulk of the material for more even heating when using Cu tape.

should be expected, both bulk and surface resistivities are inversely proportional to the concentration of CB. Contact resistance decreases more steeply with increasing CB concentration than the bulk resistance, as shown in Table 5.1 where the ratio of bulk to contact resistivities are calculated for each CBSMP blend tested.

To evenly heat a slender strip of CBSMP, most of the power input should be dissipated within the bulk of the material. Therefore, it is desirable to have a large bulk resistivity in comparison to the contact resistivity to the Cu tape. From Table 5.1, it is clear that this ratio increases with CB loading, and so a higher CB loading is expected to provide better heating performance. As previously described, continuous sheets with high CB loading above 20 wt% become prone to crack formation and lose the mechanical durability necessary for a flexible, reusable adhesive. Figure 5.7a shows infrared (IR) and optical images of a 15 wt% CBSMP blend experiencing internal joule heating through Cu tape attached to the ends of its opposite face. The hot spots directly beneath the Cu tape contact regions clearly indicate poor heating performance, with the majority of power dissipation occurring at the SMP–Cu tape interface. The tape adhesive layer thins and loses contact well before the bulk of the CBSMP strip reaches its T_g , as is required for its use as an adhesive.

Table 5.1. Ratio between the experimentally determined bulk and surface resistivities as a function of wt% carbon black (CB).

wt% CB	Bulk to Surface Resistivity Ratio (m^{-1})	
	Cu Tape	Steel Clip
5	–	10
10	–	18
15	1	30
20	6	57
25	13	86
30	14	105
15/30	42	76

5.2.2 A Composite Design for Improved Electrical Heating and Connectivity

Reduced contact resistance may be achieved by introducing small integrated contact pads within the moderately doped (15 wt%) bulk CBSMP made of more highly doped (30 wt%) CBSMP. An initial goal of the project was to create sheets of adhesive which may be cut arbitrarily to form usable strips of varying size and orientation. Therefore, the 30 wt% contact pads are molded as small (3.5 mm \times 3.5 mm), separate islands set into the surface of a bulk sheet of 15 wt% composite CBSMP, referred to as the filler. The finished product will be referred to as 15/30 CB composite, and is described with more detail in Appendix E.2. This design allows power to flow relatively unimpeded through the interface between the 30 wt% CBSMP and Cu tape to be dissipated as heat within the connecting 15 wt% CBSMP material. Thermal performance is shown in Figure 5.7b to be far superior to the homogeneous strip shown in Figure 5.7a, enabling consistent heating without threatening the integrity of the Cu tape contact. The fabrication method is described in Figure 5.8, where an additional “adhesive layer”, in this case consisting of non-doped SMP, has been added to give added bending strength,

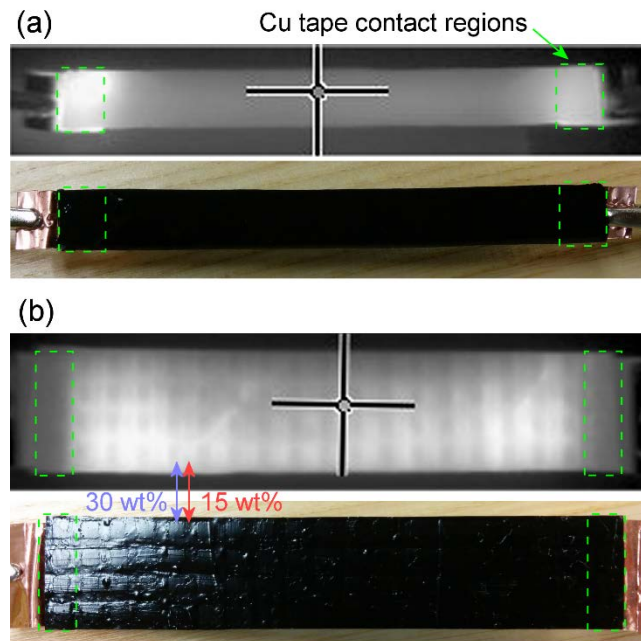


Figure 5.7. (a) Infrared and visible spectrum images of a homogeneous strip of 15 wt% CB doped SMP with applied voltage, showing excessive power dissipation at the tape contact regions; and (b) Similar images of a composite strip with 30 wt% islands and 15 wt% filler, showing the power dissipation now occurs mostly between the tape contact regions, within the more resistive filler material.

increased surface compliance (described later) and a smoother surface finish. The finished sheet may be cut arbitrarily to create adhesive strips with one electrically conductive side, and one adhesive side. The entire sheet consists of an SMP functional material, as depicted in Figure 5.9.

The electrical properties of the 15/30 CB composite strips are characterized for comparison to the homogeneous CBSMP values in Figure 5.6. The contact resistance measured for the composite strips using the steel clip method is much closer to the 15 wt% CB value than expected, most likely because contact pressure from the alligator clip is applied unevenly, more heavily weighted towards the edge of the samples which consist of the 15 wt% CBSMP material. Surprisingly, the bulk resistivity is also increased compared with the homogeneous 15 wt% CBSMP samples. This is most likely explained by the existence of an additional interfacial resistance between the 15 and 30 wt% CBSMP components within the composite. It was observed that air bubbles were easily trapped within the CBSMP mixtures during mixing and resulted in small internal voids after curing. It is likely these bubbles are especially prevalent at the interfaces between the composite components, resulting in an increased resistance to current flow. The ratio of bulk to surface resistivities is compared to the homogeneous blends in Table 5.1, indicating a significantly increased ratio particularly in the case of the Cu tape contact, which as previously stated is a desirable quality for bulk heating.

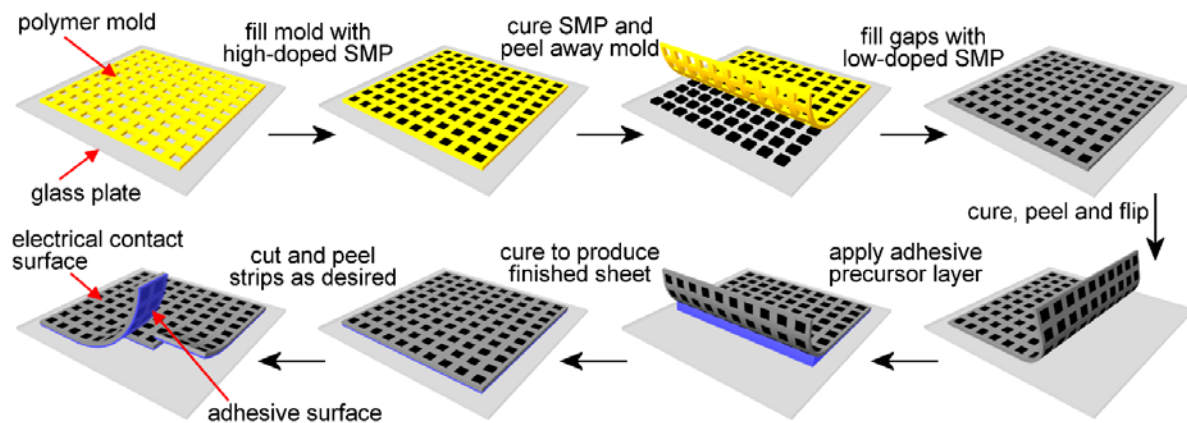


Figure 5.8. The fabrication method for the composite SMP conductive layer is shown.

Treating the 15/30 CB composite as a repeating pattern of parallel and sequential resistors, a rough estimate of the expected effective bulk resistivity may be calculated using the homogeneous CBSMP data. Likewise, an effective contact resistivity may be estimated from the homogeneous data. These

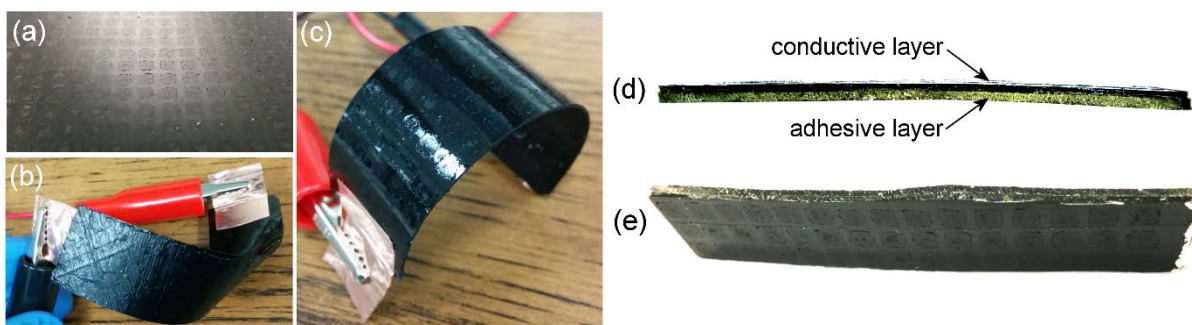


Figure 5.9. (A) A composite carbon-doped SMP sheet with 30 wt% islands and 15 wt% filler; (B) A strip of the sheet is heated above its T_g by internal joule heating and deformed; (C) The material's shape fixing property allows the strip to maintain its deformed shape when cooled; and (D) An adhesive layer comprised of non-doped SMP is applied to the conductive composite, viewed from the side and (E) the conductive face.

calculated estimates are provided in Table 5.2 along with the corresponding experimentally determined values. The calculated values assume simple, 1D current flow, and so it is unsurprising that the experimental values are greater. The significant increase over the calculated values again indicates additional interfacial resistances within the composite material, which would affect the data used to calculate contact resistivity as well as the bulk resistivity.

Table 5.2. Comparison of experimentally determined 15/30 CB composite resistivities to estimates calculated from homogeneous test data.

Material Property	Calculated	Experimental
Bulk Resistivity (Ωm)	0.089	0.396
Contact Resistivity (Ωm^2)	0.0040	0.0094

In addition to conferring electrical conductivity, adding CB to polymers is known to affect mechanical properties. Specifically, an increase in storage modulus and hardness are to be expected [204], [205]. Dynamic mechanical analysis measurements of 10 and 20 wt% CBSMP blends are compared with a non-doped control sample in Figure 5.10a (see Appendix A.4.1). Storage modulus (E') is shown to generally increase with increasing CB loading, particularly when above the material's T_g around 40 °C. Since the increase in compliance above T_g is a fundamental feature for the operation of our adhesive, this increase in E' above T_g is a negative consequence of the added CB. However, the addition of a non-doped SMP layer as the adhesive interface as shown in Figure 5.8 negates this potential problem. The

$\tan \delta$ curves provide additional assurance that the T_g undergoes only slight variation due to the addition of CB into the SMP. Comparing the non-doped SMP curves to those reported in Reference [210] shows essentially identical results. The final property of significant interest is whether the shape fixity and recovery of the non-doped SMP is maintained with added CB. Several initially-straight bars of varying CBSMP blends are shown in Figure 5.10b, bent and fixed into a horse-shoe shape with a loaded separation of ~ 1.5 mm. Upon unloading, this gap changes only a trivial amount up to a CB loading of 25 wt%, the highest loading tested, indicating that CB loading does not significantly impact the SMPs excellent shape fixity. Upon reheating, Figure 5.10c indicates similarly excellent shape recovery of each tested sample, with only perhaps a slight bend remaining in the 25 wt% CBSMP.

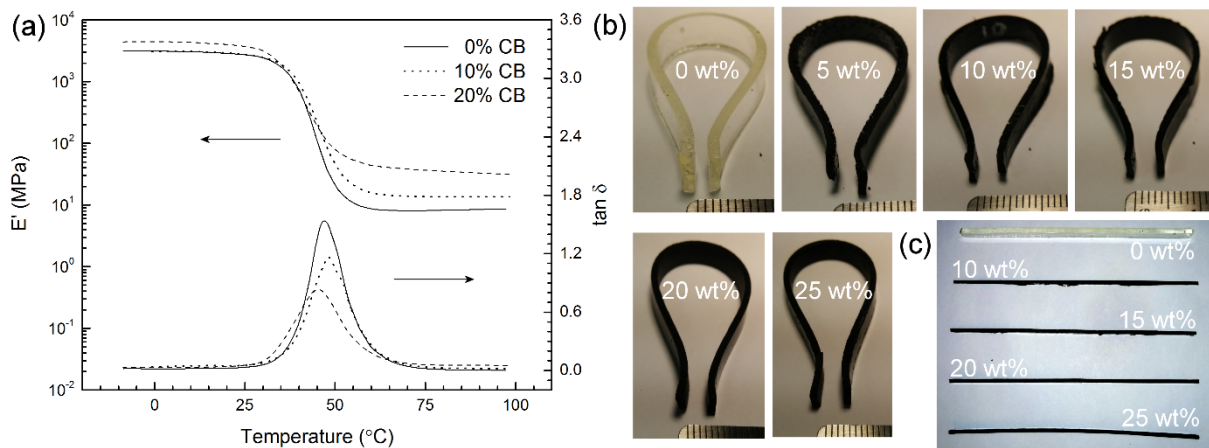


Figure 5.10 (a) Dynamic mechanical analysis (DMA) curves for various levels of CB-doped SMP. The SMP (b) shape-fixing and (c) shape-recovery properties are minimally affected by carbon doping, demonstrated using initially-straight material strips.

In Section 5.1, test samples with interfacial areas of 0.32 cm^2 were externally heated and required preload of about 40 N cm^{-2} during bonding to generate a maximum adhesion of approximately 200 N cm^{-2} . To compare the CBSMP dry adhesive with the previous results, adhesive tests were performed using similar preload for $55 \times 5 \text{ mm}$ strips (2.75 cm^2), heated by 2 W of internal joule heating using a 60 V power source. The CBSMP test strips were fabricated in a U-shape with smooth, flat glass as the test substrate. The resulting adhesion averaged approximately 30 N cm^{-2} . The reduction in adhesion strength as compared to the previous work is most likely primarily due to thermal contraction increasing interfacial stresses as lateral dimensions of the adhesive increase. Over the usual range of bonding temperatures the CBSMP adhesive expands and contracts on the order of 1% due its large thermal

expansion coefficient on the order of $200 \mu\text{m m}^{-1} \text{K}^{-1}$ (appendix A.8). It was observed during loading that failure of the SMP-substrate interface occurs suddenly, analogous to brittle fracture. The role of thermal contraction is further indicated by the occurrence of spontaneous fracture in large samples (cm scale) even in the absence of load if the difference between bonding temperature and ambient temperature is too great. For this reason, interface temperatures were limited to 75°C , compared with the previous work which used a standard of 90°C for bonding temperature. It is a general trend that adhesion for the selected SMP increases with bonding temperature with other conditions held constant; therefore, reduced bonding temperature is likely a secondary cause for the lower-than-expected adhesion. Surface patterning to promote crack trapping may be a worthwhile strategy to alleviate the issue of catastrophic failure due to localized interfacial stresses. The stresses may be further reduced by adding a less-rigid layer as the adhesive interface in place of the SMP. As the bulk SMP contracts, the more compliant surface material would deform more easily to reduce the buildup of interfacial stresses.

The adhesive performance of the finished CBSMP composite adhesive is demonstrated in Figure 5.11 on curved surfaces. First, a CBSMP strip 15 mm wide by 65 mm long is heated using a 70 V power supply with Cu tape forming the electrical contacts on opposing ends. The now-compliant strip is pressed using finger pressure to a 4.25 inch diameter clean glass cylinder, covering a 70° arc. The pressure is maintained as the power supply is turned off, resulting in a strong, rigid bond. A 10 lb weight is supported by the strip, indicating an adhesive strength in excess of 4.6 N cm^{-2} . It is believed that the reduction in adhesion compared with the flat CBSMP strip tests is due largely to the greatly reduced preload applied during bonding. It was observed after bonding that some areas were not in proper contact after cooling, partly from trapped air pockets and partly from thermal contraction as explained above. Testing the adhesion of the strip necessitated choosing a pick point; in this case, the weight was applied to the center of the strip, creating an additional localized concentration of stress on the interface thus reducing the apparent adhesion. This was likewise the case for the concave-surface demonstration, for which a 25 mm wide by 45 mm long CBSMP strip was bonded using finger pressure to the inside of a watch glass. This configuration yielded a failure strength exceeding 5.9 N cm^{-2} ; again, less than the result from the smaller and higher-preload flat strip tests. Surface patterns designed to promote crack trapping could also effectively alleviate the issues of air entrapment by creating pathways for the air to

escape during bonding. Increased preload during bonding or the use of a softer and/or stickier adhesive layer in place of or in addition to the non-doped SMP would also be expected to increase performance by helping to reduce thermally-induced interfacial stresses and reducing the necessary preload to ensure proper surface contact. As a final demonstration in Figure 5.11e, a composite SMP adhesive is gently removed from the glass by heating and peeling, thus achieving the desired adhesive reversibility.

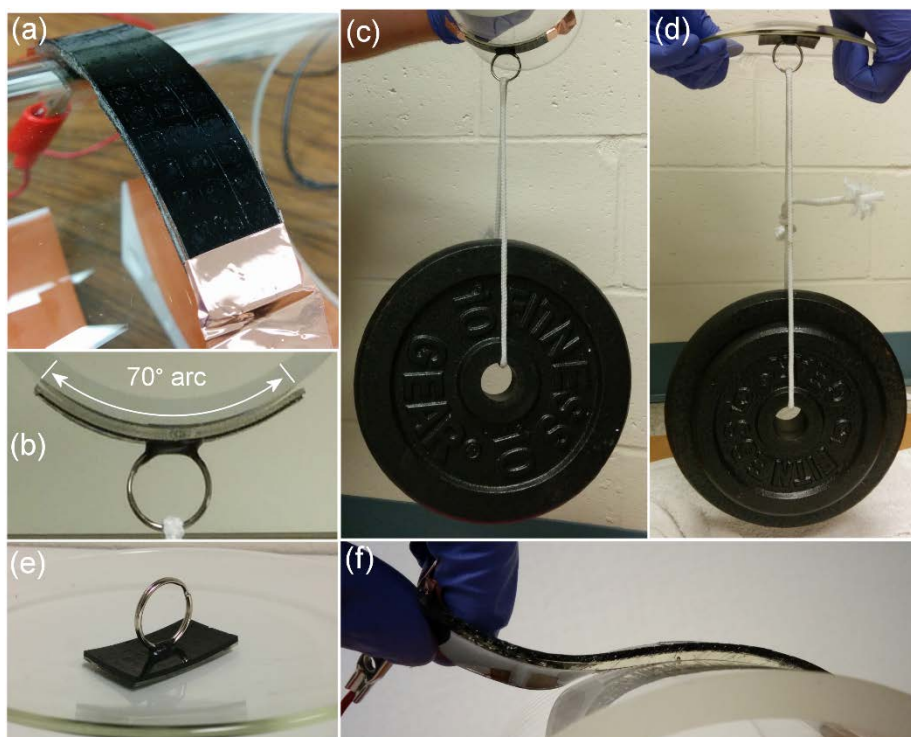


Figure 5.11. (a) An adhesive strip is internally heated and bonded to a curved glass surface covering a 70° arc (b); (c) The bonded strip supports a 10 lb weight; (D) A bonded strip supports 15 lbs on a concave glass surface, shown in greater detail in (E); and (F) Heating the bonded strip allows for easy peel removal.

A brief collection of representative conventional, or “wet”, and dry adhesive strengths are given in Table 5.3. Fibrillar adhesives are typically tested in shear, since this is also typically their direction of maximum strength and reversibility. It is stressed that wet adhesives are fundamentally different than dry adhesives, and should not be treated as a competitor to dry adhesive systems. A dry adhesive bond is by nature a temporary one, whereas the use of wet adhesives is usually intended as a permanent bond between two surfaces. Both the uses for the methods of action of each are very different.

Table 5.3. Conventional “wet” adhesive and representative fibrillar dry adhesive strength for comparison to the adhesive described in this work.

Classification	Adhesive	Adhesive Strength (N cm ⁻²)	Substrate	Reference
Wet (permanent, requires cure time)	Mussel adhesive extracts	10–300	Skin to skin	[221]
	Cyanoacrylates (super glue)	1500	Steel to Al	Master Bond (MB) Series data sheets
		210	Steel to butyl	
	3 M Epoxy 2216 B/A	1170–1320 (shear)	Steel to steel	3 M technical data sheet
		900 (shear)	Plastic to plastic	
	LOCTITE epoxy E-120HP	2300 (shear)	Glass to glass	LOCTITE technical data sheet
		150 (shear)	Acrylic to acrylic	
Dry (reusable, reversible, no cure time)	Carbon nanotube fibers	3–150 (shear)	Glass/plastic	[218]
	Polymer fibers	0.2–15 (shear)		
	Gekko gecko	10 (shear)	Acetate sheet	[222]
	SMP (<cm)	200	Glass	[223]
	SMP (>cm)	5–30	Glass	This work

Chapter 6. Alternative Formulations

Thus far in this dissertation, all experimental work and demonstrations have utilized the NGDE2 formulation described in Appendix A.1. Whether as a structural layer or as a direct-contact adhesive, the current body of SMP-based dry adhesives primarily utilize this or similar epoxy-based SMPs which possess many desirable characteristics including excellent shape fixity and recovery, thermo-mechanical stability, and ease of processing. Less desirable are their tendencies to remain stiff in their rubbery state relative to most pressure sensitive adhesives (PSAs), and their susceptibility to tearing under moderate strains. A soft rubbery state is desirable to facilitate adhesive bonding by reducing the required preload, while large recoverable strains are desirable to enable greater flexibility in the adhesives' structural design and to improve general durability.

A recent study has demonstrated a successful modification of an oft-used epoxy SMP formula, wherein the authors used a heavier (longer) epoxy monomer and greatly increased the concentration of the curing, or crosslinking, agent [224]. The resulting SMP was found to be both softer in its rubbery state and substantially more stretchable, while retaining its superlative shape memory properties. The differences in the SMP's properties are directly attributed to a decrease in crosslinking density, which allows the polymer chains greater freedom of movement in the polymer's rubbery state. The chains therefore may rearrange more readily when subjected to stress, aligning in the direction of the stress more completely and with less resistance. In this section I investigate the effects of these modifications to the epoxy SMP formula regarding dry adhesive performance, and to produce a prototype practical dry adhesive using similar formulations described herein. The effect of increased curing agent and increased monomer chain length are investigated independently through the production of several SMP formulations as described in Appendix A.2. These SMPs are tested with regard to their dry adhesive performance, and to confirm that they possess excellent mechanical and shape memory properties on par with those previously reported, for example in Reference [224].

Plots of storage modulus versus temperature for each of the SMP formulations listed in Table A.2 are provided in Figure 6.1 (see Appendix A.4.2). The data indicate the effects of increasing Jeffamine concentration are very similar to those reported in Ref. [224], decreasing the glass transition temperature (T_g) and rubbery state storage modulus while maintaining a similar glassy state storage modulus. These

observations indicate that the expected reduction in crosslinking density was achieved. The flat rubbery and glassy plateaus, together with the narrow T_g band, suggest the presence of strong shape memory performance in each of the twelve formulations. Similarly to Reference [224], changing the proportion of Jeffamine has more of an effect on the material, particularly its T_g , as its proportion is increased. This is clearly evident in E362 and E448 series tests where for example E362-J050 and E362-J060 are nearly the same, whereas E362-J060, E362-J075, and E362-J100 are substantially different, though significant and nearly uniform changes to T_g are observed between each variant of the E533 series of SMP. Varying the average molecular weight of the epoxy base has little effect on the shape and character of the modulus curves, except a noticeable reduction in rubbery state modulus for the higher-weight formulations.

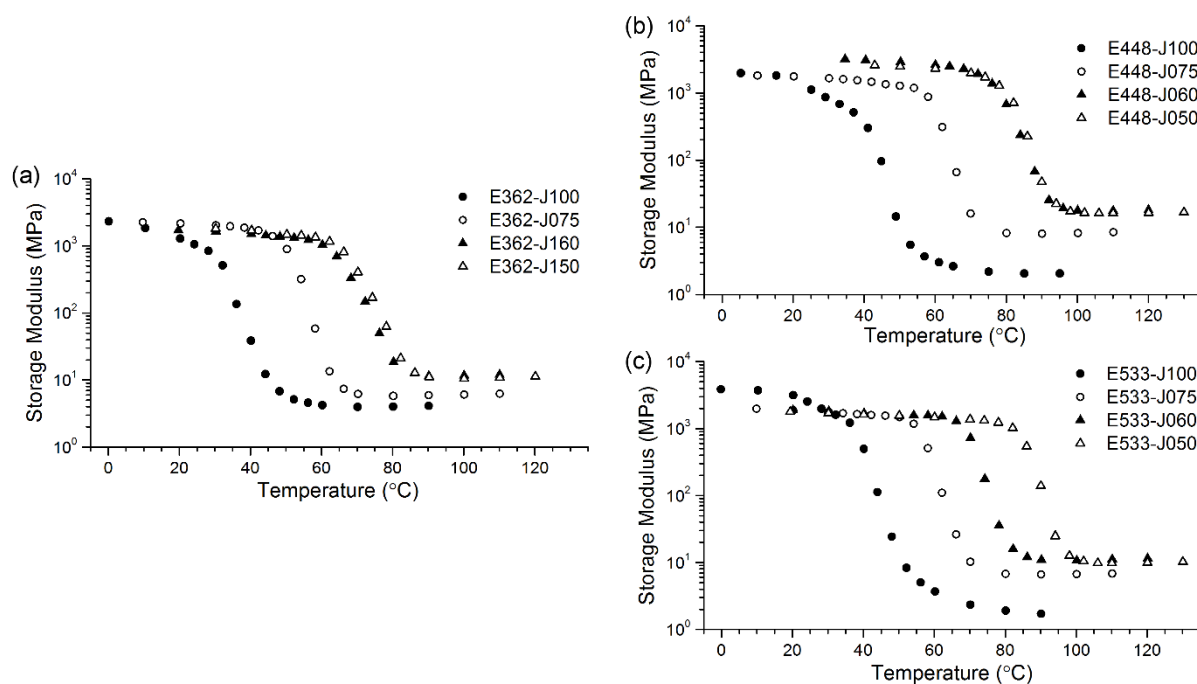


Figure 6.1 - The SMP storage modulus as a function of temperature for formulations with base epoxy average M_n of 362 g mol^{-1} (a), 448 g mol^{-1} (b), and 533 g mol^{-1} (c).

The shape memory performance of E533-J100 was tested, with results depicted in Figure 6.2a. Both fixity and recovery factors of $>99\%$ were found for a 6% peak strain, showing that even the formulation with the lowest crosslinking density shows excellent shape memory properties. Recovery at larger strains was tested using E448-J100. The first ten cycles of $\sim 100\%$ strain with temperature held constant at 50 $^{\circ}\text{C}$ shown in Figure 6.2b. The first cycle appears to show some irrecoverable strain, which is

partially due to the slower, more viscous response of the SMP at relatively low temperature not allowing complete recovery during the cycle time. Some slippage or deformation of material at the tensile grips as they sink into the SMP during its first cycle may additionally account for some apparent irrecoverable strain.

Stress versus strain curves for uniaxial tension tests of E448-J100 are shown in Figure 6.2c for three temperatures corresponding to the upper end of its T_g transition (50 °C, 60 °C, and 70 °C). In agreement with previous studies, the strain at failure or break, ϵ_b , is greater when deforming the SMP within its glass transition and show similar characteristic shapes as those provided in Reference [224]. Data for ϵ_b was collected for each of the three temperatures for E363-J100, E448-J100, and E533-J100 SMP formulations, and compared against the previously-developed NGDE2 formulation which has seen significant use in dry adhesive studies [156], [172], [194], [206], [223], [225]. Each of these formulations has a similar T_g in terms of both onset and width of transition, and therefore direct comparison of results at each temperature is reasonably fair. Figure 6.2d shows the data, presented as the average of five tests for each formulation at each temperature. Error bars indicate a 95% confidence interval for the true mean based on Student's t-test of the available sample data. The results reinforce

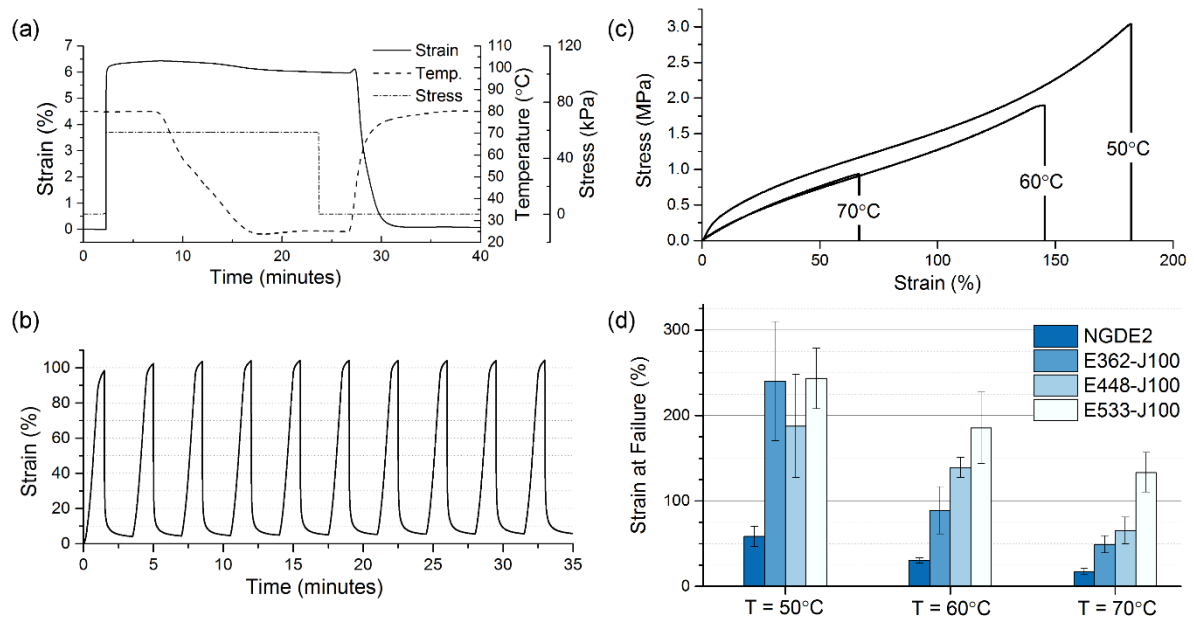


Figure 6.2 - A shape memory cycle of E533-J100 (a). Cyclic strain and recovery of E448-J100 at 50 °C (b). Typical uniaxial stress-strain curves at selected temperatures for E448-J100 (c). Failure strain results for four SMP formulations (d). Error bars represent 95% Student's t-test confidence intervals.

the observation that ϵ_b increases when tested at temperatures within each SMP's glass transition. An enhancement in ϵ_b is also clearly apparent for all three newer formulations over the more highly-crosslinked NGDE2.

The role of increased Jeffamine with respect to ϵ_b is evident through a comparison of NGDE2 with those of the other three formulations of Figure 6.2d. NGDE2 is expected to have greatly increased crosslink density compared with each of the other formulations, due in small part to the shorter average chain length of its precursor epoxy monomers [210], but more significantly due to the disparity in Jeffamine. Comparing the measured average ϵ_b for each at 50 °C (NGDE2, 58% : E362-J100, 240%), 60 °C (NGDE2, 30% : E362-J100, 89%), and 70 °C (NGDE2, 17% : E362-J100, 49%) shows a three to four-fold increase.

The effect of the epoxy base average molecular weight on ϵ_b is directly comparable across the three -J100 series formulations, and clearly indicates that a longer base monomer provides an enhancement, particularly when each SMP is in its rubbery state. The trend is less clear at 50 °C, given the surprisingly large measured ϵ_b of the E362-J100 formulation which may be attributable to the fact that the glass transitions of each formulation are similar but not identical, and thus 50 °C may happen to be nearer to the optimal ϵ_b temperature of E362-J100 than that of the other formulations. At 70 °C the difference in

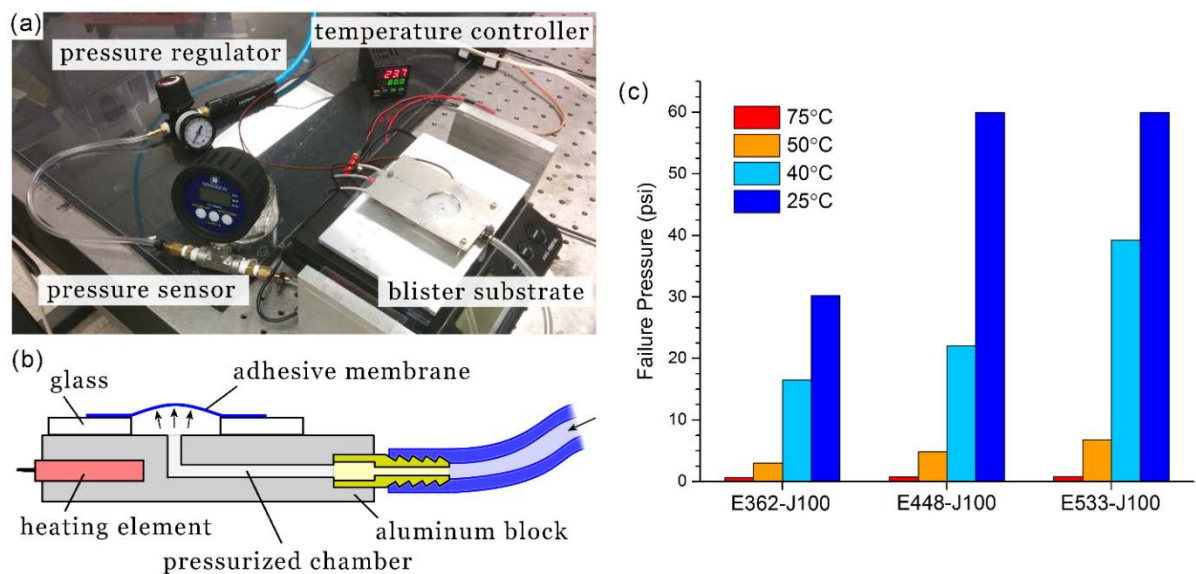


Figure 6.3 - The temperature-controlled blister test apparatus is shown (a). A cross section schematic of the blister substrate and pressure chamber (b). Blister test pressure results (c).

ϵ_b between the three newer formulations is substantial at 49%, 65%, and 133% for E362-J100, E448-J100, and E533-J100 respectively. It is worthwhile to compare results for our E448-J100 to those of the EPON1 formula of Reference [224], since they are identical in all respects except that I achieve the target average molecular weight by mixing epoxy bases of dissimilar weights. The comparison indicates a reduced ϵ_b at 50 °C and 70 °C for E448-J100, but a similar result at 60 °C. The differences may be attributable to dissimilar testing equipment and procedures, or may suggest a difference in the polymer's structure and behavior due to the bimodal distribution of monomer length in E448-J100.

The blister test apparatus shown in Figure 6.3a,b was constructed to quantitatively measure the relative adhesive performance of the high-strain SMP formulations including E363-J100, E448-J100, and E533-J100. Test procedures are outlined in Appendix F.1. Tests were conducted with each SMP in its glassy state (25 °C), rubbery state (75 °C), and at two intermediate temperatures (Figure 6.3c). The results clearly show an increase in failure pressure, indicating enhanced adhesive strength, as the SMP's temperature is reduced through its glass transition. This trend has been previously observed and attributed primarily to the increase in storage modulus and corresponding inhibition of crack propagation [194], [223]. The failure pressure is also influenced by the SMP formula, with greater monomer weight yielding enhanced adhesion. I speculate that this result is due to enhanced energy dissipation of the higher-weight formulation, particularly at lower temperatures. This theory is reinforced by observing that the measured loss modulus increases significantly with increased monomer weight (231 MPa, 299 MPa, and 534 MPa for E362-J100, E448-J100 and E533-J100 respectively at their peaks ~25 °C). The maximum pressure the test apparatus can measure is 60 psi, which was achieved for 25 °C tests of both E448-J100 and E533-J100 specimens.

A prototype practical dry adhesive system was fabricated as shown in Figure 6.4a, comprised of a block of E448-J100 with an embedded nichrome wire heating element secured to a 3D-printed attachment piece which allows for a firm connection to a separate hook (see Appendix F.2). The adhesive is bonded by first briefly heating the SMP with an attached power source (battery) and pressing it by hand against an adherend for several seconds as it cools. The hook then slides into place. It is shown supporting a backpack, loaded with approximately 3 kg of items, on multiple adherends with varying surface characteristics. It has additionally been shown to form a weight-bearing bond in both dry and wet

conditions, even firmly bonding to a glass surface coated by a film of flowing water. Regardless of bonding conditions, the adhesive may be easily removed by peeling, once the SMP is re-heated to its rubbery state. As a dry adhesive relying primarily on van der Waals adhesive forces, rather than a flowing glue layer, it is inherently reusable. When stored at room temperature, the glassy SMP is rigid and non-tacky, additionally improving its resistance to fouling from the environment.

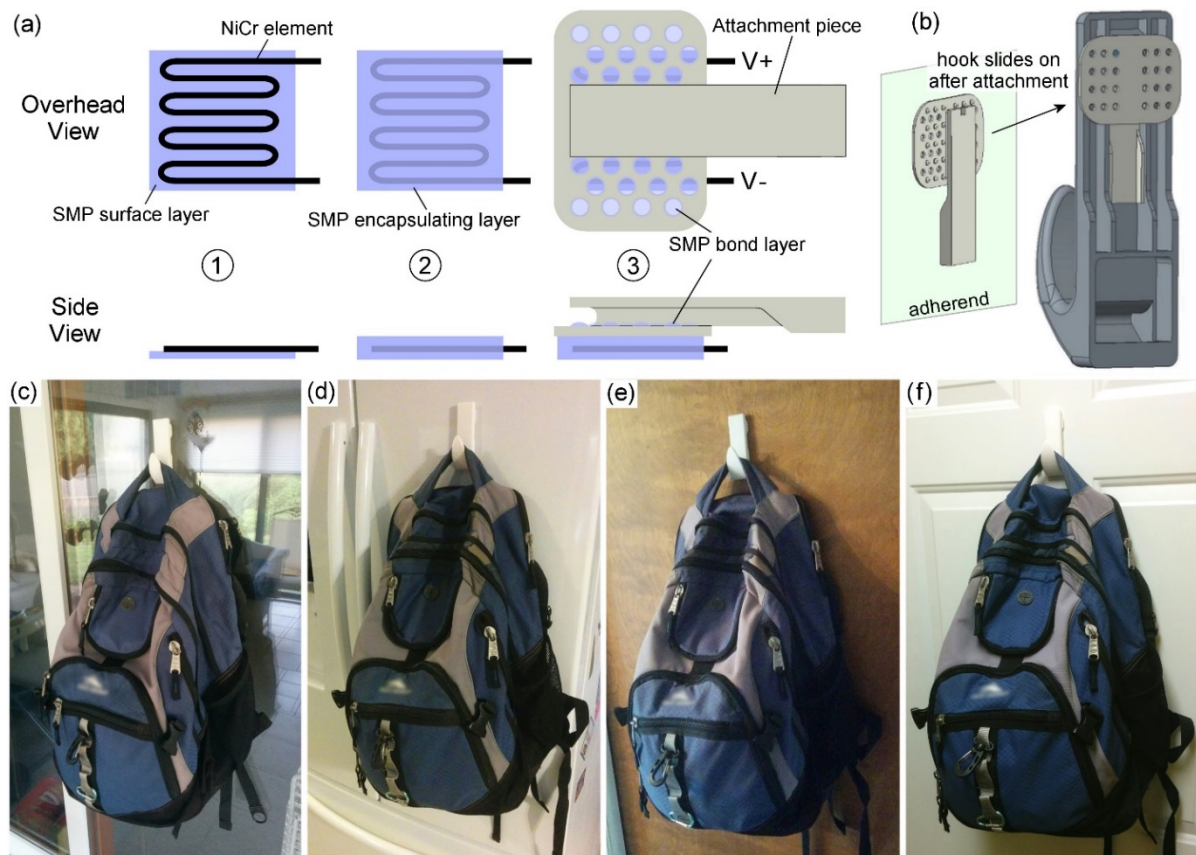


Figure 6.4 - The steps to fabricate a practical SMP adhesive are depicted (a). The completed adhesive unit is rendered usable by attaching a hook, which fits together with the attachment piece (b). Using this system, a loaded backpack is suspended by the SMP adhesive hook assembly on a glass door (c), a curved plastic refrigerator door (d), a wooden door (e), and a powder-coated metal door (f).

Chapter 7. Conclusion

Nature shows us what is possible in the field of dry adhesion. Dry adhesive research has made great strides in recent years, resulting in artificial adhesives with remarkable strength, a high degree of reversibility, impressive durability and low cost. However, no existing solution yet embodies all of these qualities simultaneously, and even those that claim to satisfy one or more frequently do so only conditionally. Thus, while a long-term goal of artificial dry adhesive research will remain the development of an integrated system conveying the versatility, strength, and longevity of the solutions found in nature, much can be said for the shorter-term development of simpler designs which provide economical solutions for less constrained problems. The adhesive pads and supporting structure of the tokay gecko are indeed impressive, but is mimicking their design the best bet for human applications? One may look to the airfoil for an example where the optimal solution to a problem is not necessarily a direct replication of the one utilized by nature. Biological systems are subject to numerous constraints to which artificial systems are not including the need to be grown and maintained by organic processes, and exist within dirty, wet, otherwise uncontrolled environments where few dry adhesive applications are expected to perform. An artificial adhesive's ability to adhere firmly to tree bark or wet leaves, for example, is irrelevant for most practical purposes.

Shape memory polymers offer numerous unique benefits over currently available alternative materials for dry adhesive applications. In the case of automated manufacturing, and in particular microscale transfer printing, SMPs offer significantly enhanced strength and versatility in terms of process design. The ability to switch the SMP's compliance on demand correspondingly allows active control over adhesive strength for unpatterned stamps. When combined with the material's inherent shape fixing and recovery abilities, a wide range of exciting design opportunities present themselves. Simple microstructuring, easily deformable due to the SMP's switchable compliance, can be used to dramatically improve the adhesive's reversibility with only a very small impact on maximum adhesive strength while also being free from time-sensitive constraints because of the on-demand nature of the SMP's shape memory properties. This ability to precisely control the SMP's compliance and the timing, speed, and extent of shape recovery adds flexibility of design, allowing full control regarding the conditions of ink release and leaves open the possibility for a wide range of stamp and microstructure

designs not possible with stamps made from inactive materials. Methods of conductive or radiative heating are highly effective at small scales, enabling shape recovery and corresponding print cycle times well below 1 second for an optimized process. Radiative heat delivery by laser absorption in SMP stamp arrays is arguably the best way forward if commercial-scale programmable and selective transfer printing is to become a reality, due to its potential for high packing density, low cost of stamp manufacture, and scalability.

Larger-scale dry adhesive applications stand to benefit from the use of SMP as well. Far more durable than most artificial fibrillar concepts, an unpatterned sheet of crosslinked SMP is capable of forming a strong and removable bond to many common surfaces found in commercial or residential environments. Certain design elements become increasingly critical as scale increases. Temperature cycle time grows substantially with SMP length scale, which is most easily countered by using very thin SMP layers and corresponding heat delivery systems positioned as near to the active material as possible. This in turn forces stronger consideration of the supporting structure to both ensure that the adhesive surface has preload evenly applied during bonding, and to provide an effective method of connecting the adhesive to the system's load during use. Issues of thermal mismatch appear to increase with length scale as well, potentially causing instability in the bond due to the development of residual stress at the adhesive interface. The use of softer, more stretchable SMPs can help to alleviate these issues somewhat by requiring less preload and reducing the residual stresses developed during the cooling cycle, though at a cost of increased compliance during unloading. The trade-off appears to be beneficial overall however, with epoxy-based SMPs with greater molecular weight can substantially increase adhesion over their more rigid variants. The observed improvement is most likely due to a combination of reduced interfacial residual stresses, enhanced interfacial conformation, and enhanced viscoelastic dissipation within the material.

List of References

- [1] K. Autumn *et al.*, “Evidence for van der Waals adhesion in gecko setae,” *Proc. Natl. Acad. Sci.*, vol. 99, no. 19, pp. 12252–12256, Sep. 2002.
- [2] B. Henning, “Morphologie und histologie der tarsen von *Tettigonia viridissima* L. (Orthoptera, Ensifera),” *Z. Für Morphol. Tiere*, vol. 79, no. 4, pp. 323–342, Dec. 1974.
- [3] W. Federle, E. L. Brainerd, T. A. McMahon, and B. Hölldobler, “Biomechanics of the movable pretarsal adhesive organ in ants and bees,” *Proc. Natl. Acad. Sci.*, vol. 98, no. 11, pp. 6215–6220, May 2001.
- [4] A. F. G. Dixon, P. C. Croghan, and R. P. Gowing, “The mechanism by which aphids adhere to smooth surfaces,” *J. Exp. Biol.*, vol. 152, no. 1, pp. 243–253, Sep. 1990.
- [5] N. Gravish, M. Wilkinson, and K. Autumn, “Frictional and elastic energy in gecko adhesive detachment,” *J. R. Soc. Interface*, vol. 5, no. 20, pp. 339–348, Mar. 2008.
- [6] W. Federle, “Why are so many adhesive pads hairy?,” *J. Exp. Biol.*, vol. 209, no. 14, pp. 2611–2621, Jul. 2006.
- [7] K. Autumn, “Gecko Adhesion: Structure, Function, and Applications,” *MRS Bull.*, vol. 32, no. 6, pp. 473–478, 2007.
- [8] R. Ruibal and V. Ernst, “The structure of the digital setae of lizards,” *J. Morphol.*, vol. 117, no. 3, pp. 271–293, Nov. 1965.
- [9] M. Henrey, J. P. Díaz Téllez, K. Wormnes, L. Pambaguian, and C. Menon, “Towards the use of mushroom-capped dry adhesives in outer space: Effects of low pressure and temperature on adhesion strength,” *Aerosp. Sci. Technol.*, vol. 29, no. 1, pp. 185–190, Aug. 2013.
- [10] J. Purto, M. Frensemeier, and E. Kroner, “Switchable Adhesion in Vacuum Using Bio-Inspired Dry Adhesives,” *ACS Appl. Mater. Interfaces*, vol. 7, no. 43, pp. 24127–24135, Nov. 2015.
- [11] L. Heepe, M. Varenberg, Y. Itovich, and S. N. Gorb, “Suction component in adhesion of mushroom-shaped microstructure,” *J. R. Soc. Interface*, vol. 8, no. 57, pp. 585–589, Apr. 2011.
- [12] D. Sameoto, H. Sharif, and C. Menon, “Investigation of low-pressure adhesion performance of mushroom shaped biomimetic dry adhesives,” *J. Adhes. Sci. Technol.*, vol. 26, no. 23, pp. 2641–2652, Dec. 2012.
- [13] M. Henrey, J. P. D. Tellez, K. Wormnes, L. Pambaguian, and C. Menon, “Sticking in space: manufacturing dry adhesives and testing their performance in space environments,” presented at the 12th Symp. on Adv. Space Technologies in Robotics and Automation, 2013.
- [14] S. Kalouche, N. Wiltsie, H. J. Su, and A. Parness, “Inchworm style gecko adhesive climbing robot,” in *2014 IEEE/RSJ International Conference on Intelligent Robots and Systems*, 2014, pp. 2319–2324.
- [15] M. Amjadi, K.-U. Kyung, I. Park, and M. Sitti, “Stretchable, Skin-Mountable, and Wearable Strain Sensors and Their Potential Applications: A Review,” *Adv. Funct. Mater.*, vol. 26, no. 11, pp. 1678–1698, Mar. 2016.
- [16] H. Chen, L. Zhang, D. Zhang, P. Zhang, and Z. Han, “Bioinspired Surface for Surgical Graspers Based on the Strong Wet Friction of Tree Frog Toe Pads,” *ACS Appl. Mater. Interfaces*, vol. 7, no. 25, pp. 13987–13995, Jul. 2015.

- [17] M. Henrey, A. Ahmed, P. Boscariol, L. Shannon, and C. Menon, "Abigaille-III: A Versatile, Bioinspired Hexapod for Scaling Smooth Vertical Surfaces," *J. Bionic Eng.*, vol. 11, no. 1, pp. 1–17, Jan. 2014.
- [18] Y. Li, J. Krahn, and C. Menon, "Bioinspired Dry Adhesive Materials and Their Application in Robotics: A Review," *J. Bionic Eng.*, vol. 13, no. 2, pp. 181–199, Apr. 2016.
- [19] S. Kim, M. Spenko, S. Trujillo, B. Heyneman, D. Santos, and M. R. Cutkosky, "Smooth Vertical Surface Climbing With Directional Adhesion," *IEEE Trans. Robot.*, vol. 24, no. 1, pp. 65–74, Feb. 2008.
- [20] E. W. Hawkes, E. V. Eason, A. T. Asbeck, and M. R. Cutkosky, "The Gecko's Toe: Scaling Directional Adhesives for Climbing Applications," *IEEEASME Trans. Mechatron.*, vol. 18, no. 2, pp. 518–526, Apr. 2013.
- [21] D. Santos, S. Kim, M. Spenko, A. Parness, and M. Cutkosky, "Directional Adhesive Structures for Controlled Climbing on Smooth Vertical Surfaces," in *Proceedings 2007 IEEE International Conference on Robotics and Automation*, 2007, pp. 1262–1267.
- [22] E. W. Hawkes, J. Ulmen, N. Esparza, and M. R. Cutkosky, "Scaling walls: Applying dry adhesives to the real world," in *2011 IEEE/RSJ International Conference on Intelligent Robots and Systems*, 2011, pp. 5100–5106.
- [23] E. W. Hawkes, E. V. Eason, D. L. Christensen, and M. R. Cutkosky, "Human climbing with efficiently scaled gecko-inspired dry adhesives," *J. R. Soc. Interface*, vol. 12, no. 102, p. 20140675, Jan. 2015.
- [24] M. R. Cutkosky, "Climbing with adhesion: from bioinspiration to biounderstanding," *Interface Focus*, vol. 5, no. 4, p. 2015.0015, Aug. 2015.
- [25] L. Daler, A. Klaptocz, A. Briod, M. Sitti, and D. Floreano, "A perching mechanism for flying robots using a fibre-based adhesive," in *2013 IEEE International Conference on Robotics and Automation*, 2013, pp. 4433–4438.
- [26] A. Kalantari, K. Mahajan, D. Ruffatto, and M. Spenko, "Autonomous perching and take-off on vertical walls for a quadrotor micro air vehicle," in *2015 IEEE International Conference on Robotics and Automation (ICRA)*, 2015, pp. 4669–4674.
- [27] E. W. Hawkes, H. Jiang, and M. R. Cutkosky, "Three-dimensional dynamic surface grasping with dry adhesion," *Int. J. Robot. Res.*, vol. 35, no. 8, pp. 943–958, Jul. 2016.
- [28] R. D. Adams, "Strength Predictions for Lap Joints, Especially with Composite Adherends. A Review," *J. Adhes.*, vol. 30, no. 1–4, pp. 219–242, Jan. 1989.
- [29] W. R. Hansen and K. Autumn, "Evidence for self-cleaning in gecko setae," *Proc. Natl. Acad. Sci. U. S. A.*, vol. 102, no. 2, pp. 385–389, Jan. 2005.
- [30] B. Bhushan and Y. C. Jung, "Natural and biomimetic artificial surfaces for superhydrophobicity, self-cleaning, low adhesion, and drag reduction," *Prog. Mater. Sci.*, vol. 56, no. 1, pp. 1–108, Jan. 2011.
- [31] C. J. Clemente, J. M. R. Bullock, A. Beale, and W. Federle, "Evidence for self-cleaning in fluid-based smooth and hairy adhesive systems of insects," *J. Exp. Biol.*, vol. 213, no. 4, pp. 635–642, Feb. 2010.
- [32] J. Genzer and A. Marmur, "Biological and Synthetic Self-Cleaning Surfaces," *MRS Bull.*, vol. 33, no. 8, pp. 742–746, Aug. 2008.

- [33] S. Kim, E. Cheung, and M. Sitti, “Wet Self-Cleaning of Biologically Inspired Elastomer Mushroom Shaped Microfibrillar Adhesives,” *Langmuir*, vol. 25, no. 13, pp. 7196–7199, Jul. 2009.
- [34] Y. Wang, S. Lehmann, J. Shao, and D. Sameoto, “Adhesion Circle: A New Approach To Better Characterize Directional Gecko-Inspired Dry Adhesives,” *ACS Appl. Mater. Interfaces*, Dec. 2016.
- [35] R. Sahay, H. Y. Low, A. Baji, S. Foong, and K. L. Wood, “A state-of-the-art review and analysis on the design of dry adhesion materials for applications such as climbing micro-robots,” *RSC Adv.*, vol. 5, no. 63, pp. 50821–50832, Jun. 2015.
- [36] X. A. Wu *et al.*, “Tactile sensing for gecko-inspired adhesion,” in *2015 IEEE/RSJ International Conference on Intelligent Robots and Systems (IROS)*, 2015, pp. 1501–1507.
- [37] N. Wettels and A. Parness, “Advances in fibrillar on-off polymer adhesive: Sensing and engagement speed,” in *2014 IEEE/RSJ International Conference on Intelligent Robots and Systems*, 2014, pp. 4266–4271.
- [38] E. V. Eason, E. W. Hawkes, M. Windheim, D. L. Christensen, T. Libby, and M. R. Cutkosky, “Stress distribution and contact area measurements of a gecko toe using a high-resolution tactile sensor,” *Bioinspir. Biomim.*, vol. 10, no. 1, p. 16013, 2015.
- [39] Y. Cui *et al.*, “Mimicking a gecko’s foot with strong adhesive strength based on a spinnable vertically aligned carbon nanotube array,” *RSC Adv.*, vol. 4, no. 18, pp. 9056–9060, Jan. 2014.
- [40] H. E. Jeong, J.-K. Lee, H. N. Kim, S. H. Moon, and K. Y. Suh, “A nontransferring dry adhesive with hierarchical polymer nanohairs,” *Proc. Natl. Acad. Sci.*, vol. 106, no. 14, pp. 5639–5644, Apr. 2009.
- [41] H. E. Jeong, J.-K. Lee, M. K. Kwak, S. H. Moon, and K. Y. Suh, “Effect of leaning angle of gecko-inspired slanted polymer nanohairs on dry adhesion,” *Appl. Phys. Lett.*, vol. 96, no. 4, p. 43704, Jan. 2010.
- [42] Y.-C. Lin, Y.-N. Hsu, and Y.-C. Chung, “Bio-inspired HDPE-based dry adhesives and their layer-by-layer catechol modification on the surface for use in humid environments,” *RSC Adv.*, vol. 4, no. 44, pp. 22931–22937, 2014.
- [43] J. Lee and R. S. Fearing, “Contact Self-Cleaning of Synthetic Gecko Adhesive from Polymer Microfibers,” *Langmuir*, vol. 24, no. 19, pp. 10587–10591, Oct. 2008.
- [44] H. Ko *et al.*, “Wet and Dry Adhesion Properties of Self-Selective Nanowire Connectors,” *Adv. Funct. Mater.*, vol. 19, no. 19, pp. 3098–3102, Oct. 2009.
- [45] M. Xu, F. Du, S. Ganguli, A. Roy, and L. Dai, “Carbon nanotube dry adhesives with temperature-enhanced adhesion over a large temperature range,” *Nat. Commun.*, vol. 7, p. 13450, Nov. 2016.
- [46] S. Y. Yang *et al.*, “Elastomer Surfaces with Directionally Dependent Adhesion Strength and Their Use in Transfer Printing with Continuous Roll-to-Roll Applications,” *Adv. Mater.*, vol. 24, no. 16, pp. 2117–2122, Apr. 2012.
- [47] M. P. Murphy, S. Kim, and M. Sitti, “Enhanced Adhesion by Gecko-Inspired Hierarchical Fibrillar Adhesives,” *ACS Appl. Mater. Interfaces*, vol. 1, no. 4, pp. 849–855, Apr. 2009.
- [48] J. Y. Chung and M. K. Chaudhury, “Roles of discontinuities in bio-inspired adhesive pads,” *J. R. Soc. Interface*, vol. 2, no. 2, pp. 55–61, Mar. 2005.

- [49] A. Ghatak, "Peeling off an adhesive layer with spatially varying modulus," *Phys. Rev. E*, vol. 81, no. 2, p. 21603, Feb. 2010.
- [50] D. S. Kim *et al.*, "Replication of high-aspect-ratio nanopillar array for biomimetic gecko foot-hair prototype by UV nano embossing with anodic aluminum oxide mold," *Microsyst. Technol.*, vol. 13, no. 5–6, pp. 601–606, Mar. 2007.
- [51] T. S. Kustandi, V. D. Samper, D. K. Yi, W. S. Ng, P. Neuzil, and W. Sun, "Self-Assembled Nanoparticles Based Fabrication of Gecko Foot-Hair-Inspired Polymer Nanofibers," *Adv. Funct. Mater.*, vol. 17, no. 13, pp. 2211–2218, Sep. 2007.
- [52] T. Kim, C. Pang, and K. Y. Suh, "Shape-Tunable Polymer Nanofibrillar Structures by Oblique Electron Beam Irradiation," *Langmuir*, vol. 25, no. 16, pp. 8879–8882, Aug. 2009.
- [53] K. Autumn *et al.*, "Adhesive force of a single gecko foot-hair," *Nature*, vol. 405, no. 6787, pp. 681–685, Jun. 2000.
- [54] R. Sahay, H. Parveen, A. Baji, V. A. Ganesh, and A. S. Ranganath, "Fabrication of PVDF hierarchical fibrillar structures using electrospinning for dry-adhesive applications," *J. Mater. Sci.*, vol. 52, no. 5, pp. 2435–2441, Mar. 2017.
- [55] R. Sahay, H. Parveen, A. Sargur Ranganath, V. Anand Ganesh, and A. Baji, "On the adhesion of hierarchical electrospun fibrous structures and prediction of their pull-off strength," *RSC Adv.*, vol. 6, no. 53, pp. 47883–47889, 2016.
- [56] M. D. Bartlett, A. B. Croll, D. R. King, B. M. Paret, D. J. Irschick, and A. J. Crosby, "Looking Beyond Fibrillar Features to Scale Gecko-Like Adhesion," *Adv. Mater.*, vol. 24, no. 8, pp. 1078–1083, Feb. 2012.
- [57] R. Sahay, A. Baji, A. S. Ranganath, and V. Anand Ganesh, "Durable adhesives based on electrospun poly(vinylidene fluoride) fibers," *J. Appl. Polym. Sci.*, vol. 134, no. 2, p. n/a-n/a, Jan. 2017.
- [58] J. Risan, A. B. Croll, and F. Azarmi, "Compliance switching for adhesion control," *J. Polym. Sci. Part B Polym. Phys.*, vol. 53, no. 1, pp. 48–57, Jan. 2015.
- [59] R. Wang, X. Xiao, and T. Xie, "Viscoelastic Behavior and Force Nature of Thermo-Reversible Epoxy Dry Adhesives," *Macromol. Rapid Commun.*, vol. 31, no. 3, pp. 295–299, Feb. 2010.
- [60] B. T. Michal, E. J. Spencer, and S. J. Rowan, "Stimuli-Responsive Reversible Two-Level Adhesion from a Structurally Dynamic Shape-Memory Polymer," *ACS Appl. Mater. Interfaces*, vol. 8, no. 17, pp. 11041–11049, May 2016.
- [61] D. R. King and A. J. Crosby, "Optimizing Adhesive Design by Understanding Compliance," *ACS Appl. Mater. Interfaces*, vol. 7, no. 50, pp. 27771–27781, Dec. 2015.
- [62] D. R. King, M. D. Bartlett, C. A. Gilman, D. J. Irschick, and A. J. Crosby, "Creating Gecko-Like Adhesives for 'Real World' Surfaces," *Adv. Mater.*, vol. 26, no. 25, pp. 4345–4351, Jul. 2014.
- [63] M. D. Bartlett and A. J. Crosby, "High Capacity, Easy Release Adhesives From Renewable Materials," *Adv. Mater.*, vol. 26, no. 21, pp. 3405–3409, Jun. 2014.
- [64] S. A. Pendergraph, M. D. Bartlett, K. R. Carter, and A. J. Crosby, "Enhancing Adhesion of Elastomeric Composites through Facile Patterning of Surface Discontinuities," *ACS Appl. Mater. Interfaces*, vol. 6, no. 9, pp. 6845–6850, May 2014.
- [65] S. Kim and M. Sitti, "Biologically inspired polymer microfibers with spatulate tips as repeatable fibrillar adhesives," *Appl. Phys. Lett.*, vol. 89, no. 26, p. 261911, Dec. 2006.

- [66] C. Greiner, A. del Campo, and E. Arzt, “Adhesion of Bioinspired Micropatterned Surfaces: Effects of Pillar Radius, Aspect Ratio, and Preload,” *Langmuir*, vol. 23, no. 7, pp. 3495–3502, Mar. 2007.
- [67] A. del Campo, C. Greiner, and E. Arzt, “Contact Shape Controls Adhesion of Bioinspired Fibrillar Surfaces,” *Langmuir*, vol. 23, no. 20, pp. 10235–10243, Sep. 2007.
- [68] B. Aksak, M. P. Murphy, and M. Sitti, “Adhesion of Biologically Inspired Vertical and Angled Polymer Microfiber Arrays,” *Langmuir*, vol. 23, no. 6, pp. 3322–3332, Mar. 2007.
- [69] D. Sameoto and C. Menon, “Deep UV patterning of acrylic masters for molding biomimetic dry adhesives,” *J. Micromechanics Microengineering*, vol. 20, no. 11, p. 115037, 2010.
- [70] Z. Rong *et al.*, “Bio-Inspired Hierarchical Polymer Fiber–Carbon Nanotube Adhesives,” *Adv. Mater.*, vol. 26, no. 9, pp. 1456–1461, Mar. 2014.
- [71] N. J. Glassmaker, A. Jagota, C.-Y. Hui, and J. Kim, “Design of biomimetic fibrillar interfaces: 1. Making contact,” *J. R. Soc. Interface*, vol. 1, no. 1, pp. 23–33, Nov. 2004.
- [72] M. P. Murphy, B. Aksak, and M. Sitti, “Adhesion and anisotropic friction enhancements of angled heterogeneous micro-fiber arrays with spherical and spatula tips,” *J. Adhes. Sci. Technol.*, vol. 21, no. 12–13, pp. 1281–1296, Jan. 2007.
- [73] S. Kim, M. Sitti, C.-Y. Hui, R. Long, and A. Jagota, “Effect of backing layer thickness on adhesion of single-level elastomer fiber arrays,” *Appl. Phys. Lett.*, vol. 91, no. 16, p. 161905, Oct. 2007.
- [74] S. M. Kang, “Bioinspired design and fabrication of green-environmental dry adhesive with robust wide-tip shape,” *Int. J. Precis. Eng. Manuf.-Green Technol.*, vol. 3, no. 2, pp. 189–192, Apr. 2016.
- [75] H. Yi *et al.*, “Continuous and Scalable Fabrication of Bioinspired Dry Adhesives via a Roll-to-Roll Process with Modulated Ultraviolet-Curable Resin,” *ACS Appl. Mater. Interfaces*, vol. 6, no. 16, pp. 14590–14599, Aug. 2014.
- [76] W.-G. Bae, D. Kim, and K.-Y. Suh, “Instantly switchable adhesion of bridged fibrillar adhesive via gecko-inspired detachment mechanism and its application to a transportation system,” *Nanoscale*, vol. 5, no. 23, pp. 11876–11884, 2013.
- [77] V. Barreau, R. Hensel, N. K. Guimard, A. Ghatak, R. M. McMeeking, and E. Arzt, “Fibrillar Elastomeric Micropatterns Create Tunable Adhesion Even to Rough Surfaces,” *Adv. Funct. Mater.*, vol. 26, no. 26, pp. 4687–4694, Jul. 2016.
- [78] K. L. Johnson, K. Kendall, and A. D. Roberts, “Surface Energy and the Contact of Elastic Solids,” *Proc. R. Soc. Lond. Math. Phys. Eng. Sci.*, vol. 324, no. 1558, pp. 301–313, Sep. 1971.
- [79] K. Autumn and A. M. Peattie, “Mechanisms of Adhesion in Geckos,” *Integr. Comp. Biol.*, vol. 42, no. 6, pp. 1081–1090, Dec. 2002.
- [80] L. Pastewka and M. O. Robbins, “Contact between rough surfaces and a criterion for macroscopic adhesion,” *Proc. Natl. Acad. Sci. U. S. A.*, vol. 111, no. 9, pp. 3298–3303, Mar. 2014.
- [81] Y. Zhao, T. Tong, L. Delzeit, A. Kashani, M. Meyyappan, and A. Majumdar, “Interfacial energy and strength of multiwalled-carbon-nanotube-based dry adhesive,” *J. Vac. Sci. Technol. B*, vol. 24, no. 1, pp. 331–335, Jan. 2006.
- [82] S. Kawai *et al.*, “Van der Waals interactions and the limits of isolated atom models at interfaces,” *Nat. Commun.*, vol. 7, p. 11559, May 2016.

- [83]F. London, “The general theory of molecular forces,” *Trans. Faraday Soc.*, vol. 33, no. 0, p. 8b–26, Jan. 1937.
- [84]F. M. Fowkes, “Attractive forces at interfaces,” *Ind. Eng. Chem.*, vol. 56, no. 12, pp. 40–52, Dec. 1964.
- [85]M. E. Schrader, “Young-Dupre Revisited,” *Langmuir*, vol. 11, no. 9, pp. 3585–3589, Sep. 1995.
- [86]L. A. Girifalco and R. J. Good, “A Theory for the Estimation of Surface and Interfacial Energies. I. Derivation and Application to Interfacial Tension,” *J. Phys. Chem.*, vol. 61, no. 7, pp. 904–909, Jul. 1957.
- [87]D. Maugis, “Adherence of Elastomers: Fracture Mechanics Aspects,” *J. Adhes.*, vol. 23, no. 1, pp. 61–66, Sep. 1987.
- [88]C.-Y. Hui, J. A. S. J. Bennison, and J. D. Londono, “Crack blunting and the strength of soft elastic solids,” *Proc. R. Soc. Lond. Math. Phys. Eng. Sci.*, vol. 459, no. 2034, pp. 1489–1516, Jun. 2003.
- [89]R. Dhelika, K. Sawai, K. Takahashi, W. Takarada, T. Kikutani, and S. Saito, “Electrostatic chuck consisting of polymeric electrostatic inductive fibers for handling of objects with rough surfaces,” *Smart Mater. Struct.*, vol. 22, no. 9, p. 95010, 2013.
- [90]J. Krahn and C. Menon, “Electro-Dry-Adhesion,” *Langmuir*, vol. 28, no. 12, pp. 5438–5443, Mar. 2012.
- [91]D. Ruffatto, A. Parness, and M. Spenko, “Improving controllable adhesion on both rough and smooth surfaces with a hybrid electrostatic/gecko-like adhesive,” *J. R. Soc. Interface*, vol. 11, no. 93, Apr. 2014.
- [92]K. H. Koh, M. Sreekumar, and S. G. Ponnambalam, “Hybrid electrostatic and elastomer adhesion mechanism for wall climbing robot,” *Mechatronics*, vol. 35, pp. 122–135, May 2016.
- [93]C. Cao, X. Sun, Y. Fang, Q.-H. Qin, A. Yu, and X.-Q. Feng, “Theoretical model and design of electroadhesive pad with interdigitated electrodes,” *Mater. Des.*, vol. 89, pp. 485–491, Jan. 2016.
- [94]H. E. Jeong, S. H. Lee, P. Kim, and K. Y. Suh, “High aspect-ratio polymer nanostructures by tailored capillarity and adhesive force,” *Colloids Surf. Physicochem. Eng. Asp.*, vol. 313–314, pp. 359–364, Feb. 2008.
- [95]G. Hanna, W. Jon, and W. P. J. Barnes, “Adhesion and Detachment of the Toe Pads of Tree Frogs,” *J. Exp. Biol.*, vol. 155, no. 1, pp. 103–125, Jan. 1991.
- [96]S. Ishii, “Adhesion of a Leaf Feeding Ladybird *Epilachna vigintioctomaculta* (Coleoptera : Coccinellidae) on a Virtically Smooth Surface,” *Appl. Entomol. Zool.*, vol. 22, no. 2, pp. 222–228, 1987.
- [97]W. Federle, M. Riehle, A. S. G. Curtis, and R. J. Full, “An Integrative Study of Insect Adhesion: Mechanics and Wet Adhesion of Pretarsal Pads in Ants,” *Integr. Comp. Biol.*, vol. 42, no. 6, pp. 1100–1106, Dec. 2002.
- [98]G. Huber *et al.*, “Evidence for capillarity contributions to gecko adhesion from single spatula nanomechanical measurements,” *Proc. Natl. Acad. Sci. U. S. A.*, vol. 102, no. 45, pp. 16293–16296, Nov. 2005.
- [99]C. Gay, “Stickiness—Some Fundamentals of Adhesion,” *Integr. Comp. Biol.*, vol. 42, no. 6, pp. 1123–1126, Dec. 2002.

- [100] R. Bates, "Studies in the nature of adhesive tack," *J. Appl. Polym. Sci.*, vol. 20, no. 11, pp. 2941–2954, Nov. 1976.
- [101] N. Menga, L. Afferrante, and G. Carbone, "Adhesive and adhesiveless contact mechanics of elastic layers on slightly wavy rigid substrates," *Int. J. Solids Struct.*, vol. 88–89, pp. 101–109, Jun. 2016.
- [102] S. Abbot, "Dahlquist Criterion | Practical Adhesion Science | Prof Steven Abbott," 28-Dec-2016. [Online]. Available: <http://www.stevenabbott.co.uk/practical-adhesion/dahlquist.php>. [Accessed: 28-Dec-2016].
- [103] A. Jagota and S. J. Bennison, "Mechanics of Adhesion Through a Fibrillar Microstructure," *Integr. Comp. Biol.*, vol. 42, no. 6, pp. 1140–1145, Dec. 2002.
- [104] M. Sitti and R. S. Fearing, "Synthetic gecko foot-hair micro/nano-structures as dry adhesives," *J. Adhes. Sci. Technol.*, vol. 17, no. 8, pp. 1055–1073, Jan. 2003.
- [105] E. Arzt, S. Gorb, and R. Spolenak, "From micro to nano contacts in biological attachment devices," *Proc. Natl. Acad. Sci.*, vol. 100, no. 19, pp. 10603–10606, Sep. 2003.
- [106] M. Varenberg, B. Murarash, Y. Kligerman, and S. N. Gorb, "Geometry-controlled adhesion: revisiting the contact splitting hypothesis," *Appl. Phys. A*, vol. 103, no. 4, pp. 933–938, Jun. 2011.
- [107] M. L. Williams, "The continuum interpretation for fracture and adhesion," *J. Appl. Polym. Sci.*, vol. 13, no. 1, pp. 29–40, Jan. 1969.
- [108] D. Maugis and M. Barquins, "Fracture mechanics and the adherence of viscoelastic bodies," *J. Phys. Appl. Phys.*, vol. 11, no. 14, p. 1989, 1978.
- [109] G. R. Irwin, "Linear fracture mechanics, fracture transition, and fracture control," *Eng. Fract. Mech.*, vol. 1, no. 2, pp. 241–257, Aug. 1968.
- [110] G. J. Lake and A. G. Thomas, "The Strength of Highly Elastic Materials," *Proc. R. Soc. Lond. Math. Phys. Eng. Sci.*, vol. 300, no. 1460, pp. 108–119, Aug. 1967.
- [111] A. N. Gent, "Adhesion and Strength of Viscoelastic Solids. Is There a Relationship between Adhesion and Bulk Properties?," *Langmuir*, vol. 12, no. 19, pp. 4492–4496, Jan. 1996.
- [112] D. Maugis, "Subcritical crack growth, surface energy, fracture toughness, stick-slip and embrittlement," *J. Mater. Sci.*, vol. 20, no. 9, pp. 3041–3073, Sep. 1985.
- [113] R. A. Schapery, "A theory of crack initiation and growth in viscoelastic media," *Int. J. Fract.*, vol. 11, no. 1, pp. 141–159, 1975.
- [114] A. N. Gent and J. Schultz, "Effect of Wetting Liquids on the Strength of Adhesion of Viscoelastic Material," *J. Adhes.*, vol. 3, no. 4, pp. 281–294, Mar. 1972.
- [115] P. Prentice, "The influence of molecular weight on the fracture of thermoplastic glassy polymers," *J. Mater. Sci.*, vol. 20, no. 4, pp. 1445–1454, 1985.
- [116] N. Lakhera *et al.*, "Effect of viscoelasticity on the spherical and flat adhesion characteristics of photopolymerizable acrylate polymer networks," *Int. J. Adhes. Adhes.*, vol. 44, pp. 184–194, Jul. 2013.
- [117] R.-J. Chang and A. N. Gent, "Effect of interfacial bonding on the strength of adhesion of elastomers. I. Self-adhesion," *J. Polym. Sci. Polym. Phys. Ed.*, vol. 19, no. 10, pp. 1619–1633, Oct. 1981.
- [118] F. Saulnier, T. Ondarçuhu, A. Aradian, and E. Raphaël, "Adhesion between a Viscoelastic Material and a Solid Surface," *Macromolecules*, vol. 37, no. 3, pp. 1067–1075, Feb. 2004.

- [119] B. N. J. Persson, “On the mechanism of adhesion in biological systems,” *J. Chem. Phys.*, vol. 118, no. 16, pp. 7614–7621, Apr. 2003.
- [120] B. N. J. Persson, “Fracture of polymers,” *J. Chem. Phys.*, vol. 110, no. 19, pp. 9713–9724, May 1999.
- [121] H. Gao and J. R. Rice, “A First-Order Perturbation Analysis of Crack Trapping by Arrays of Obstacles,” *J. Appl. Mech.*, vol. 56, no. 4, pp. 828–836, Dec. 1989.
- [122] N. J. Glassmaker, A. Jagota, C.-Y. Hui, W. L. Noderer, and M. K. Chaudhury, “Biologically inspired crack trapping for enhanced adhesion,” *Proc. Natl. Acad. Sci.*, vol. 104, no. 26, pp. 10786–10791, Jun. 2007.
- [123] W. L. Noderer, L. Shen, S. Vajpayee, N. J. Glassmaker, A. Jagota, and C.-Y. Hui, “Enhanced adhesion and compliance of film-terminated fibrillar surfaces,” *Proc. R. Soc. Lond. Math. Phys. Eng. Sci.*, vol. 463, no. 2086, pp. 2631–2654, Oct. 2007.
- [124] S. Yan, L. He, and H. Wang, “Adhesion hysteresis of a film-terminated fibrillar array,” *Sci. China Phys. Mech. Astron.*, vol. 55, no. 6, pp. 1026–1031, Jun. 2012.
- [125] N. Nadermann, J. Ning, A. Jagota, and C.-Y. Hui, “Active Switching of Adhesion in a Film-Terminated Fibrillar Structure,” *Langmuir*, vol. 26, no. 19, pp. 15464–15471, Oct. 2010.
- [126] L. Shen, N. J. Glassmaker, A. Jagota, and C.-Y. Hui, “Strongly enhanced static friction using a film-terminated fibrillar interface,” *Soft Matter*, vol. 4, no. 3, pp. 618–625, Feb. 2008.
- [127] S. Gorb, Y. Jiao, and M. Scherge, “Ultrastructural architecture and mechanical properties of attachment pads in *Tettigonia viridissima* (Orthoptera Tettigoniidae),” *J. Comp. Physiol. A*, vol. 186, no. 9, pp. 821–831, Sep. 2000.
- [128] R. E. Snodgrass, *Anatomy of the Honey Bee*. Cornell University Press, 1984.
- [129] Y. Zhou, A. Robinson, C. Viney, and W. Federle, “Effect of shear forces and ageing on the compliance of adhesive pads in adult cockroaches,” *J. Exp. Biol.*, vol. 218, no. 17, pp. 2775–2781, Sep. 2015.
- [130] C. J. Clemente, J.-H. Dirks, D. R. Barbero, U. Steiner, and W. Federle, “Friction ridges in cockroach climbing pads: anisotropy of shear stress measured on transparent, microstructured substrates,” *J. Comp. Physiol. A*, vol. 195, no. 9, pp. 805–814, Sep. 2009.
- [131] J. W. Arnold, “Adaptive features on the tarsi of cockroaches (Insecta: Dictyoptera),” *Int. J. Insect Morphol. Embryol.*, vol. 3, no. 3, pp. 317–334, Dec. 1974.
- [132] J.-H. Dirks, C. J. Clemente, and W. Federle, “Insect tricks: two-phasic foot pad secretion prevents slipping,” *J. R. Soc. Interface*, vol. 7, no. 45, pp. 587–593, Apr. 2010.
- [133] A. D. Lees and J. Hardie, “The organs of adhesion in the aphid *Megoura viciae*,” *J. Exp. Biol.*, vol. 136, no. 1, pp. 209–228, May 1988.
- [134] W. Federle, W. J. P. Barnes, W. Baumgartner, P. Drechsler, and J. M. Smith, “Wet but not slippery: boundary friction in tree frog adhesive toe pads,” *J. R. Soc. Interface*, vol. 3, no. 10, pp. 689–697, Oct. 2006.
- [135] D.-M. Drotlef, L. Stepien, M. Kappl, W. J. P. Barnes, H.-J. Butt, and A. del Campo, “Insights into the Adhesive Mechanisms of Tree Frogs using Artificial Mimics,” *Adv. Funct. Mater.*, vol. 23, no. 9, pp. 1137–1146, Mar. 2013.
- [136] M. Kappl, F. Kaveh, and W. J. P. Barnes, “Nanoscale friction and adhesion of tree frog toe pads,” *Bioinspir. Biomim.*, vol. 11, no. 3, p. 35003, 2016.

- [137] J. Iturri *et al.*, “Torrent Frog-Inspired Adhesives: Attachment to Flooded Surfaces,” *Adv. Funct. Mater.*, vol. 25, no. 10, pp. 1499–1505, Mar. 2015.
- [138] S. B. Emerson and D. Diehl, “Toe pad morphology and mechanisms of sticking in frogs,” *Biol. J. Linn. Soc.*, vol. 13, no. 3, pp. 199–216, May 1980.
- [139] N. E. Stork, “A scanning electron microscope study of tarsal adhesive setae in the Coleoptera,” *Zool. J. Linn. Soc.*, vol. 68, no. 3, pp. 173–306, Mar. 1980.
- [140] S. Niederegger and S. N. Gorb, “Friction and adhesion in the tarsal and metatarsal scopulae of spiders,” *J. Comp. Physiol. A*, vol. 192, no. 11, pp. 1223–1232, Nov. 2006.
- [141] D. Labonte *et al.*, “Extreme positive allometry of animal adhesive pads and the size limits of adhesion-based climbing,” *Proc. Natl. Acad. Sci.*, vol. 113, no. 5, pp. 1297–1302, Feb. 2016.
- [142] E. Bauchnenß and M. Renner, “Pulvillus of *Calliphora erythrocephala* Meig. (Diptera : Calliphoridae),” *Int. J. Insect Morphol. Embryol.*, vol. 6, no. 3, pp. 225–227, Aug. 1977.
- [143] Y. Chen, M.-C. Shih, M.-H. Wu, E.-C. Yang, and K.-J. Chi, “Underwater attachment using hairs: the functioning of spatula and sucker setae from male diving beetles,” *J. R. Soc. Interface*, vol. 11, no. 97, p. 20140273, Aug. 2014.
- [144] E. Wohlfart, J. O. Wolff, E. Arzt, and S. N. Gorb, “The whole is more than the sum of all its parts: collective effect of spider attachment organs,” *J. Exp. Biol.*, vol. 217, no. 2, pp. 222–224, Jan. 2014.
- [145] J. O. Wolff and S. N. Gorb, “Radial arrangement of Janus-like setae permits friction control in spiders,” *Sci. Rep.*, vol. 3, p. 1101, Jan. 2013.
- [146] E. E. Williams and J. A. Peterson, “Convergent and Alternative Designs in the Digital Adhesive Pads of Scincid Lizards,” *Science*, vol. 215, no. 4539, pp. 1509–1511, Mar. 1982.
- [147] M. S. Prowse, M. Wilkinson, J. B. Puthoff, G. Mayer, and K. Autumn, “Effects of humidity on the mechanical properties of gecko setae,” *Acta Biomater.*, vol. 7, no. 2, pp. 733–738, Feb. 2011.
- [148] N. Gravish *et al.*, “Rate-dependent frictional adhesion in natural and synthetic gecko setae,” *J. R. Soc. Interface*, vol. 7, no. 43, pp. 259–269, Feb. 2010.
- [149] C.-Y. Hui, N. J. Glassmaker, and A. Jagota, “How Compliance Compensates for Surface Roughness in Fibrillar Adhesion,” *J. Adhes.*, vol. 81, no. 7–8, pp. 699–721, Jul. 2005.
- [150] J. McKittrick, P.-Y. Chen, S. G. Bodde, W. Yang, E. E. Novitskaya, and M. A. Meyers, “The Structure, Functions, and Mechanical Properties of Keratin,” *JOM*, vol. 64, no. 4, pp. 449–468, Apr. 2012.
- [151] B. Wang, W. Yang, J. McKittrick, and M. A. Meyers, “Keratin: Structure, mechanical properties, occurrence in biological organisms, and efforts at bioinspiration,” *Prog. Mater. Sci.*, vol. 76, pp. 229–318, Mar. 2016.
- [152] K. Autumn, A. Dittmore, D. Santos, M. Spenko, and M. Cutkosky, “Frictional adhesion: a new angle on gecko attachment,” *J. Exp. Biol.*, vol. 209, no. 18, pp. 3569–3579, Sep. 2006.
- [153] C. J. Clemente and W. Federle, “Pushing versus pulling: division of labour between tarsal attachment pads in cockroaches,” *Proc. R. Soc. Lond. B Biol. Sci.*, vol. 275, no. 1640, pp. 1329–1336, Jun. 2008.
- [154] H. Liu, J. Choi, G. Zaghi, J. Zhang, C. Carraro, and R. Maboudian, “Frictional characteristics of stiff, high aspect ratio microfiber arrays based on cyclic olefin polymers,” *J. Adhes. Sci. Technol.*, vol. 0, no. 0, pp. 1–11, Oct. 2016.

- [155] A. Parness *et al.*, “A microfabricated wedge-shaped adhesive array displaying gecko-like dynamic adhesion, directionality and long lifetime,” *J. R. Soc. Interface*, vol. 6, no. 41, pp. 1223–1232, Dec. 2009.
- [156] S. Kim, M. Sitti, T. Xie, and X. Xiao, “Reversible dry micro-fibrillar adhesives with thermally controllable adhesion,” *Soft Matter*, vol. 5, no. 19, pp. 3689–3693, Sep. 2009.
- [157] B. Zhao *et al.*, “Role of Tilted Adhesion Fibrils (Setae) in the Adhesion and Locomotion of Gecko-like Systems,” *J. Phys. Chem. B*, vol. 113, no. 12, pp. 3615–3621, Mar. 2009.
- [158] J. Genzer and K. Efimenko, “Recent developments in superhydrophobic surfaces and their relevance to marine fouling: a review,” *Biofouling*, vol. 22, no. 5, pp. 339–360, Jan. 2006.
- [159] R. Spolenak, S. Gorb, and E. Arzt, “Adhesion design maps for bio-inspired attachment systems,” *Acta Biomater.*, vol. 1, no. 1, pp. 5–13, Jan. 2005.
- [160] C. Greiner, R. Spolenak, and E. Arzt, “Adhesion design maps for fibrillar adhesives: The effect of shape,” *Acta Biomater.*, vol. 5, no. 2, pp. 597–606, Feb. 2009.
- [161] J. Seo, J. Eisenhaure, and S. Kim, “Micro-wedge array surface of a shape memory polymer as a reversible dry adhesive,” *Extreme Mech. Lett.*, vol. 9, Part 1, pp. 207–214, Dec. 2016.
- [162] P. Day, E. V. Eason, N. Esparza, D. Christensen, and M. Cutkosky, “Microwedge Machining for the Manufacture of Directional Dry Adhesives,” *J. Micro Nano-Manuf.*, vol. 1, no. 1, pp. 11001-11001–10, Mar. 2013.
- [163] H. Yi, M. Kang, M. K. Kwak, and H. E. Jeong, “Simple and Reliable Fabrication of Bioinspired Mushroom-Shaped Micropillars with Precisely Controlled Tip Geometries,” *ACS Appl. Mater. Interfaces*, vol. 8, no. 34, pp. 22671–22678, Aug. 2016.
- [164] Y. Zhang, S. Qu, X. Cheng, X. Gao, and X. Guo, “Fabrication and Characterization of Gecko-inspired Dry Adhesion, Superhydrophobicity and Wet Self-cleaning Surfaces,” *J. Bionic Eng.*, vol. 13, no. 1, pp. 132–142, Jan. 2016.
- [165] H. Hu *et al.*, “Biomimetic Mushroom-Shaped Microfibers for Dry Adhesives by Electrically Induced Polymer Deformation,” *ACS Appl. Mater. Interfaces*, vol. 6, no. 16, pp. 14167–14173, Aug. 2014.
- [166] M. Röhrig, M. Thiel, M. Worgull, and H. Hölscher, “3D Direct Laser Writing of Nano- and Microstructured Hierarchical Gecko-Mimicking Surfaces,” *Small*, vol. 8, no. 19, pp. 3009–3015, Oct. 2012.
- [167] A. K. Geim, S. V. Dubonos, I. V. Grigorieva, K. S. Novoselov, A. A. Zhukov, and S. Y. Shapoval, “Microfabricated adhesive mimicking gecko foot-hair,” *Nat. Mater.*, vol. 2, no. 7, pp. 461–463, Jul. 2003.
- [168] J. Krahn, E. Bovero, and C. Menon, “Magnetic Field Switchable Dry Adhesives,” *ACS Appl. Mater. Interfaces*, vol. 7, no. 4, pp. 2214–2222, Feb. 2015.
- [169] T. Xie, “Recent advances in polymer shape memory,” *Polymer*, vol. 52, no. 22, pp. 4985–5000, Oct. 2011.
- [170] K. S. Santhosh Kumar, R. Biju, and C. P. Reghunadhan Nair, “Progress in shape memory epoxy resins,” *React. Funct. Polym.*, vol. 73, no. 2, pp. 421–430, Feb. 2013.
- [171] I. A. Rousseau, “Challenges of shape memory polymers: A review of the progress toward overcoming SMP’s limitations,” *Polym. Eng. Sci.*, vol. 48, no. 11, pp. 2075–2089, Nov. 2008.

- [172] T. Xie and X. Xiao, "Self-Peeling Reversible Dry Adhesive System," *Chem. Mater.*, vol. 20, no. 9, pp. 2866–2868, May 2008.
- [173] S. M. Spearing, "Materials issues in microelectromechanical systems (MEMS)," *Acta Mater.*, vol. 48, no. 1, pp. 179–196, Jan. 2000.
- [174] Y. Zhang, B. K. Chen, X. Liu, and Y. Sun, "Autonomous Robotic Pick-and-Place of Microobjects," *IEEE Trans. Robot.*, vol. 26, no. 1, pp. 200–207, Feb. 2010.
- [175] H. T. Miyazaki, Y. Tomizawa, S. Saito, T. Sato, and N. Shinya, "Adhesion of micrometer-sized polymer particles under a scanning electron microscope," *J. Appl. Phys.*, vol. 88, no. 6, pp. 3330–3340, Sep. 2000.
- [176] D. S. Haliyo and S. Regnier, "Advanced applications using [mu]MAD, the adhesion based dynamic micro-manipulator," in *2003 IEEE/ASME International Conference on Advanced Intelligent Mechatronics, 2003. AIM 2003. Proceedings, 2003*, vol. 2, pp. 880–885 vol.2.
- [177] N. Dechev, W. L. Cleghorn, and J. K. Mills, "Microassembly of 3-D microstructures using a compliant, passive microgripper," *J. Microelectromechanical Syst.*, vol. 13, no. 2, pp. 176–189, Apr. 2004.
- [178] S. Saito and M. Sonoda, "Non-impact deposition for electrostatic micromanipulation of a conductive particle by a single probe," *J. Micromechanics Microengineering*, vol. 18, no. 10, p. 107001, Oct. 2008.
- [179] O. Fuchiwaki, A. Ito, D. Misaki, and H. Aoyama, "Multi-axial micromanipulation organized by versatile micro robots and micro tweezers," in *IEEE International Conference on Robotics and Automation, 2008. ICRA 2008, 2008*, pp. 893–898.
- [180] A. Carlson, A. M. Bowen, Y. Huang, R. G. Nuzzo, and J. A. Rogers, "Transfer printing techniques for materials assembly and micro/nanodevice fabrication," *Adv. Mater.*, vol. 24, no. 39, pp. 5284–5318, Oct. 2012.
- [181] H. Keum *et al.*, "Microassembly of Heterogeneous Materials using Transfer Printing and Thermal Processing," *Sci. Rep.*, vol. 6, p. 29925, Jul. 2016.
- [182] H. Keum *et al.*, "Silicon micro-masonry using elastomeric stamps for three-dimensional microfabrication," *J. Micromechanics Microengineering*, vol. 22, no. 5, p. 55018, May 2012.
- [183] J. Viventi *et al.*, "A Conformal, Bio-Interfaced Class of Silicon Electronics for Mapping Cardiac Electrophysiology," *Sci. Transl. Med.*, vol. 2, no. 24, p. 24ra22-24ra22, Mar. 2010.
- [184] D.-H. Kim *et al.*, "Materials for multifunctional balloon catheters with capabilities in cardiac electrophysiological mapping and ablation therapy," *Nat. Mater.*, vol. 10, no. 4, pp. 316–323, Apr. 2011.
- [185] Z. Fan, J. C. Ho, Z. A. Jacobson, H. Razavi, and A. Javey, "Large-scale, heterogeneous integration of nanowire arrays for image sensor circuitry," *Proc. Natl. Acad. Sci. U. S. A.*, vol. 105, no. 32, pp. 11066–11070, Aug. 2008.
- [186] T. Kim *et al.*, "Thin Film Receiver Materials for Deterministic Assembly by Transfer Printing," *Chem. Mater.*, vol. 26, no. 11, pp. 3502–3507, Jun. 2014.
- [187] S. Kim *et al.*, "Microstructured elastomeric surfaces with reversible adhesion and examples of their use in deterministic assembly by transfer printing," *Proc. Natl. Acad. Sci.*, vol. 107, no. 40, pp. 17095–17100, Oct. 2010.

- [188] A. Carlson *et al.*, “Shear-enhanced adhesiveless transfer printing for use in deterministic materials assembly,” *Appl. Phys. Lett.*, vol. 98, no. 26, p. 264104, Jun. 2011.
- [189] R. Saeidpourazar *et al.*, “Laser-Driven Micro Transfer Placement of Prefabricated Microstructures,” *J. Microelectromechanical Syst.*, vol. 21, no. 5, pp. 1049–1058, Oct. 2012.
- [190] A. Carlson, S. Wang, P. Elvikis, P. M. Ferreira, Y. Huang, and J. A. Rogers, “Active, Programmable Elastomeric Surfaces with Tunable Adhesion for Deterministic Assembly by Transfer Printing,” *Adv. Funct. Mater.*, vol. 22, no. 21, pp. 4476–4484, Nov. 2012.
- [191] Y. Yang *et al.*, “Microcontact Printing: Arrays of Silicon Micro/Nanostructures Formed in Suspended Configurations for Deterministic Assembly Using Flat and Roller-Type Stamps (Small 4/2011),” *Small*, vol. 7, no. 4, pp. 417–417, Feb. 2011.
- [192] Y. Y. Huang *et al.*, “Stamp Collapse in Soft Lithography,” *Langmuir*, vol. 21, no. 17, pp. 8058–8068, Aug. 2005.
- [193] A. F. Bower, *Applied Mechanics of Solids*, 1 edition. CRC Press, 2011.
- [194] J. D. Eisenhaure, S. I. Rhee, A. M. Al-Okaily, A. Carlson, P. M. Ferreira, and S. Kim, “The Use of Shape Memory Polymers for MEMS Assembly,” *J. Microelectromechanical Syst.*, vol. 25, no. 1, pp. 69–77, Feb. 2016.
- [195] B. Lorenz *et al.*, “Adhesion: role of bulk viscoelasticity and surface roughness,” *J. Phys. Condens. Matter*, vol. 25, no. 22, p. 225004, Jun. 2013.
- [196] Z. Chen, S. Diebels, N. J. Peter, and A. S. Schneider, “Identification of finite viscoelasticity and adhesion effects in nanoindentation of a soft polymer by inverse method,” *Comput. Mater. Sci.*, vol. 72, pp. 127–139, May 2013.
- [197] G. Haiat and E. Barthel, “An approximate model for the adhesive contact of rough viscoelastic surfaces,” *ArXiv07090584v1 Cond-Mat*, Sep. 2007.
- [198] G. Castellanos, E. Arzt, and M. Kamperman, “Effect of viscoelasticity on adhesion of bioinspired micropatterned epoxy surfaces,” *Langmuir ACS J. Surf. Colloids*, vol. 27, no. 12, pp. 7752–7759, Jun. 2011.
- [199] S. Wanka, M. Kappl, M. Wolkenhauer, and H.-J. Butt, “Measuring Adhesion Forces in Powder Collectives by Inertial Detachment,” *Langmuir*, vol. 29, no. 52, pp. 16075–16083, Dec. 2013.
- [200] S. Kim *et al.*, “Enhanced adhesion with pedestal-shaped elastomeric stamps for transfer printing,” *Appl. Phys. Lett.*, vol. 100, no. 17, p. 171909, Apr. 2012.
- [201] Y. Mengüç, S. Y. Yang, S. Kim, J. A. Rogers, and M. Sitti, “Gecko-Inspired Controllable Adhesive Structures Applied to Micromanipulation,” *Adv. Funct. Mater.*, vol. 22, no. 6, pp. 1246–1254, Mar. 2012.
- [202] Y. Yang *et al.*, “Arrays of Silicon Micro/Nanostructures Formed in Suspended Configurations for Deterministic Assembly Using Flat and Roller-Type Stamps,” *Small*, vol. 7, no. 4, pp. 484–491, Feb. 2011.
- [203] N. Ahmed, C. Dagdeviren, J. A. Rogers, and P. M. Ferreira, “Active Polymeric Composite Membranes for Localized Actuation and Sensing in Microtransfer Printing,” *J. Microelectromechanical Syst.*, vol. 24, no. 4, pp. 1016–1028, Aug. 2015.
- [204] J.-C. Huang and C.-L. Wu, “Processability, mechanical properties, and electrical conductivities of carbon black-filled ethylene-vinyl acetate copolymers,” *Adv. Polym. Technol.*, vol. 19, no. 2, pp. 132–139, Jun. 2000.

- [205] J.-C. Huang, "Carbon black filled conducting polymers and polymer blends," *Adv. Polym. Technol.*, vol. 21, no. 4, pp. 299–313, Dec. 2002.
- [206] J. Eisenhaure and S. Kim, "An Internally Heated Shape Memory Polymer Dry Adhesive," *Polymers*, vol. 6, no. 8, pp. 2274–2286, Aug. 2014.
- [207] R. Saeidpourazar, M. D. Sangid, J. A. Rogers, and P. M. Ferreira, "A prototype printer for laser driven micro-transfer printing," *J. Manuf. Process.*, vol. 14, no. 4, pp. 416–424, Oct. 2012.
- [208] A. M. Al-okaily and P. M. Ferreira, "Multi-physics modeling for laser micro-transfer printing delamination," *J. Manuf. Process.*, vol. 20, pp. 414–424, Oct. 2015.
- [209] K. Kanari and T. Ozawa, "Thermal Conductivity of Epoxy Resins Cured with Aliphatic Amines," *Polym. J.*, vol. 4, no. 4, pp. 372–378, May 1973.
- [210] T. Xie and I. A. Rousseau, "Facile tailoring of thermal transition temperatures of epoxy shape memory polymers," *Polymer*, vol. 50, no. 8, pp. 1852–1856, Apr. 2009.
- [211] O. Loebich, "The optical properties of gold," *Gold Bull.*, vol. 5, no. 1, pp. 2–10, Mar. 1972.
- [212] A. Bhaswara *et al.*, "Fabrication of nanoplate resonating structures via micro-masonry," *J. Micromechanics Microengineering*, vol. 24, no. 11, p. 115012, 2014.
- [213] B. Jeong *et al.*, "Complex nonlinear dynamics in the limit of weak coupling of a system of microcantilevers connected by a geometrically nonlinear tunable nanomembrane," *Nanotechnology*, vol. 25, no. 46, p. 465501, 2014.
- [214] Z. Yang, B. Jeong, A. Vakakis, and S. Kim, "A Tip-Tilt-Piston Micromirror With an Elastomeric Universal Joint Fabricated via Micromasonry," *J. Microelectromechanical Syst.*, vol. 24, no. 2, pp. 262–264, Apr. 2015.
- [215] Y. Xue, Y. Zhang, X. Feng, S. Kim, J. A. Rogers, and Y. Huang, "A theoretical model of reversible adhesion in shape memory surface relief structures and its application in transfer printing," *J. Mech. Phys. Solids*, vol. 77, pp. 27–42, Apr. 2015.
- [216] J. Wu *et al.*, "Mechanics of reversible adhesion," *Soft Matter*, vol. 7, no. 18, pp. 8657–8662, Sep. 2011.
- [217] D.-W. Oh, S. Kim, J. A. Rogers, D. G. Cahill, and S. Sinha, "Interfacial Thermal Conductance of Transfer-Printed Metal Films," *Adv. Mater.*, vol. 23, no. 43, pp. 5028–5033, Nov. 2011.
- [218] S. Hu and Z. Xia, "Rational Design and Nanofabrication of Gecko-Inspired Fibrillar Adhesives," *Small*, vol. 8, no. 16, pp. 2464–2468, Aug. 2012.
- [219] H. Münstedt, "Rheological experiments at constant stress as efficient method to characterize polymeric materials," *J. Rheol. 1978-Present*, vol. 58, no. 3, pp. 565–587, May 2014.
- [220] G. K. Reeves and H. B. Harrison, "Obtaining the specific contact resistance from transmission line model measurements," *IEEE Electron Device Lett.*, vol. 3, no. 5, pp. 111–113, May 1982.
- [221] L. Ninan, J. Monahan, R. L. Stroshine, J. J. Wilker, and R. Shi, "Adhesive strength of marine mussel extracts on porcine skin," *Biomaterials*, vol. 24, no. 22, pp. 4091–4099, Oct. 2003.
- [222] D. J. IRSCHICK, C. C. AUSTIN, K. PETREN, R. N. FISHER, J. B. LOSOS, and O. ELLERS, "A comparative analysis of clinging ability among pad-bearing lizards," *Biol. J. Linn. Soc.*, vol. 59, no. 1, pp. 21–35, Sep. 1996.
- [223] J. D. Eisenhaure, T. Xie, S. Varghese, and S. Kim, "Microstructured Shape Memory Polymer Surfaces with Reversible Dry Adhesion," *ACS Appl. Mater. Interfaces*, vol. 5, no. 16, pp. 7714–7717, Aug. 2013.

- [224] N. Zheng, G. Fang, Z. Cao, Q. Zhao, and T. Xie, “High strain epoxy shape memory polymer,” *Polym. Chem.*, vol. 6, no. 16, pp. 3046–3053, Apr. 2015.
- [225] J. Eisenhaure and S. Kim, “Laser-Driven Shape Memory Effect for Transfer Printing Combining Parallelism with Individual Object Control,” *Adv. Mater. Technol.*, vol. 1, no. 7, p. 1600098–n/a, Oct. 2016.
- [226] D. Maugis, “Adhesion of spheres: The JKR-DMT transition using a dugdale model,” *J. Colloid Interface Sci.*, vol. 150, no. 1, pp. 243–269, Apr. 1992.
- [227] J. Krahn, D. Sameoto, and C. Menon, “Controllable biomimetic adhesion using embedded phase change material,” *Smart Mater. Struct.*, vol. 20, no. 1, p. 15014, Jan. 2011.
- [228] X. Luo, K. E. Lauber, and P. T. Mather, “A thermally responsive, rigid, and reversible adhesive,” *Polymer*, vol. 51, no. 5, pp. 1169–1175, Mar. 2010.
- [229] L. Qu, L. Dai, M. Stone, Z. Xia, and Z. L. Wang, “Carbon Nanotube Arrays with Strong Shear Binding-On and Easy Normal Lifting-Off,” *Science*, vol. 322, no. 5899, pp. 238–242, Oct. 2008.
- [230] L. Qu and L. Dai, “Gecko-Foot-Mimetic Aligned Single-Walled Carbon Nanotube Dry Adhesives with Unique Electrical and Thermal Properties,” *Adv. Mater.*, vol. 19, no. 22, pp. 3844–3849, Nov. 2007.
- [231] Y. Wang *et al.*, “Switchable Dry Adhesion with Step-like Micropillars and Controllable Interfacial Contact,” *ACS Appl. Mater. Interfaces*, vol. 8, no. 15, pp. 10029–10037, Apr. 2016.
- [232] S. Song and M. Sitti, “Soft Grippers Using Micro-fibrillar Adhesives for Transfer Printing,” *Adv. Mater.*, vol. 26, no. 28, pp. 4901–4906, Jul. 2014.
- [233] Z. Ye, G. Z. Lum, S. Song, S. Rich, and M. Sitti, “Phase Change of Gallium Enables Highly Reversible and Switchable Adhesion,” *Adv. Mater.*, vol. 28, no. 25, pp. 5088–5092, Jul. 2016.
- [234] A. G. Gillies, J. Kwak, and R. S. Fearing, “Controllable Particle Adhesion with a Magnetically Actuated Synthetic Gecko Adhesive,” *Adv. Funct. Mater.*, vol. 23, no. 26, pp. 3256–3261, Jul. 2013.
- [235] J. Lee, C. Majidi, B. Schubert, and R. S. Fearing, “Sliding-induced adhesion of stiff polymer microfibre arrays. I. Macroscale behaviour,” *J. R. Soc. Interface*, vol. 5, no. 25, pp. 835–844, Aug. 2008.
- [236] J. Lee and R. S. Fearing, “Wet Self-Cleaning of Superhydrophobic Microfiber Adhesives Formed from High Density Polyethylene,” *Langmuir*, vol. 28, no. 43, pp. 15372–15377, Oct. 2012.
- [237] S. Kim, B. Aksak, and M. Sitti, “Enhanced friction of elastomer microfiber adhesives with spatulate tips,” *Appl. Phys. Lett.*, vol. 91, no. 22, p. 221913, Nov. 2007.

Appendix A. Materials and SMP Property Test Procedures

A.1 Preparation of NGDE2

For the majority of the experimental work in this dissertation, a particular SMP formulation developed by Xie and Rousseau in Reference [210] was used. In that work it is referred to as “NGDE2,” and here I will continue to use that designation. This particular formulation has been used as part of several dry adhesive systems [156], [172], [223]. The epoxy-based SMP used for this work was created from a 1:1:1 molar ratio of three liquids: EPON 826 (The diglycidyl ether of bisphenol A epoxy monomer; Momentive, Columbus, OH, USA), Jeffamine D230 (poly(propylene glycol)bis(2-aminopropyl) ether; Huntsman Corporation, The Woodlands, TX, USA), and NGDE (Neopentyl glycol diglycidyl ether; TCI America, New York, NY, USA). The mixing ratios of the chemicals by mole and by weight are included in Table A.1. The usual procedure for preparing the SMP precursor is to first heat the EPON 826 to 60 °C for 30 min to remove any crystallization which may have formed sitting at room temperature. NGDE is then added in proper proportion, followed by Jeffamine D230. Blending is easily accomplished by vigorously shaking the mixture in a sealed container for several seconds. Before use, the mixture may be set aside for up to several hours at room temperature, or longer if refrigerated.

The precursor may be poured onto or into any surface and allowed to fill the mold cavities, if any. Curing is accelerated by heating, accomplished at 100 °C for 90 minutes unless otherwise stated. An additional hour of time at 130 °C is sometimes used to ensure completeness of the curing process.

Table A.1 - Component Mixing Proportions for NGDE2

Formulation	Epoxy M _n (g mol ⁻¹)	Molar Proportion			Weight Proportion		
		EPON 826	NGDE	Jeffamine	EPON 826	NGDE	Jeffamine
NGDE2	289	0.5	0.5	0.5	1.000	0.600	0.639

A.2 Preparation of High Molecular Weight SMP Formulations

SMP with increased molecular weights were created similarly as described in Section A.1, but with a higher molecular weight variant of EPON 826, here referred to as E1075, substituted for the NGDE. The proportion of Jeffamine D230, hereafter referred to as simply Jeffamine, is also varied. EPON 826 has an average molecular weight of ~362 g mol⁻¹, while the chemically identical E1075 has an average molecular weight of ~1075 g mol⁻¹. Intermediate epoxy monomer weights, determined on a molar basis,

were created by mixing EPON 826 and E1075 according to the ratios given in Table A.2. The proportion of Jeffamine used for each SMP formulation is likewise included in Table A.2, on both molar and weight bases. Formulation names are derived from the average molecular weight of the epoxy monomer mixture, followed by the ratio of Jeffamine to epoxy monomer mixture.

The higher molecular weight of E1075 results in it assuming a solid form at room temperature, thus somewhat complicating the blending process as follows. E1075 and EPON 826 were combined in a glass container, heated to 120 °C in order to completely melt the E1075, then thoroughly mixed by manual stirring while still at 120 °C. Room temperature Jeffamine was then stirred into the epoxy mixture. The precursor may then be poured and molded as previously, although the higher-molecular weight variants display greater viscosity compared with NGDE2 precursor can increase the practical difficulty of producing small molded features due to enhanced bubble trapping and the much shorter working time due to the need to keep it at elevated temperature to flow easily. Curing is again effected by curing for 90 minutes at 100 °C.

Table A.2 - Component Mixing Proportions for High Molecular Weight SMPs

Formulation	Epoxy M _n (g mol ⁻¹)	Molar Proportion			Weight Proportion		
		EPON 826	E1075	Jeffamine	EPON 826	E1075	Jeffamine
E362-J100	361.9	1.000	---	1.000	1.000	---	0.636
E362-J075				0.752	1.000	---	0.478
E362-J060				0.599	1.000	---	0.381
E362-J050				0.500	1.000	---	0.318
E448-J100	447.6	0.899	0.101	1.000	1.000	0.334	0.707
E448-J075				0.752	1.000	0.334	0.531
E448-J060				0.599	1.000	0.334	0.423
E448-J050				0.500	1.000	0.334	0.353
E533-J100	533.3	0.760	0.240	1.000	1.000	0.940	0.837
E533-J075				0.752	1.000	0.940	0.629
E533-J060				0.599	1.000	0.940	0.501
E533-J050				0.500	1.000	0.940	0.418

A.3 Other Materials

Carbon black VULCAN XC72R supplied by Cabot Corporation (Boston, MA, USA) was used for all CBSMP blends, including both laser-assisted transfer printing microscale stamps and electrically conductive, internally heated SMP.

Molds for dynamic mechanical analysis (DMA) and transmission line model (TLM) test samples and for composite CBSMP fabrication were created using a Formiga P 100 selective laser sintering system (EOS, Andrä-Wördern, Austria) with material PA 2200, polyamide white. This machine and material were likewise used for the production of the 3D-printed portions of the demonstrative wall-hanging system.

A.4 Dynamic Mechanical Analysis (DMA) -Based Test Measurements

All dynamic mechanical analysis (DMA) testing, failure strain measurements, thermal expansion measurements, and SMP fixity and recovery factor measurements where noted, were performed using a Q800 DMA from TA Instruments (New Castle, DE), with an attached gas cooling accessory (GCA) when testing below room temperature. Engineering stress and strain are reported, based on the test sample's initial length and cross sectional area.

A.4.1 Procedure for DMA-based Testing of Chapter 5

SMP and CBSMP samples 5 mm wide, 1.5 to 2.1 mm thick, and at least 35 mm long were produced by curing the SMP as a flat sheet and manually cutting them to size with a sharp knife. The samples were then clamped in the DMA in a tensile configuration for temperature step/frequency sweep testing. Across the glass transition range, measurements were taken at 2 °C intervals, with 4 °C intervals used away from T_g . The reported data was gathered at 1 Hz excitation with a 0.05% strain amplitude. Testing blends prepared above 20 wt% CB was prohibitively difficult due to the tendency for sample fracture during the course of the test.

Thermal expansion was measured by tracking the linear motion of a bar-shaped SMP sample with rectangular cross section of 0.7 mm² under a static load of 1 mN while it is incrementally heated and cooled. Temperature increments of 5 °C between -20 °C and 110 °C were used, except near T_g (35 °C to 60 °C) where temperature increments were reduced to 1 °C. The temperature was held isothermally for 5 minutes at each increment. The temperature range was spanned from -20 °C to 110 °C, then back to 20 °C, with the average of the two data sets used to produce the final reported curve.

A.4.2 Procedure for DMA-based Testing of Chapter 6

Laser-cut samples of rectangular cross section approximately 1.75 mm wide and 0.5 mm thick were used. Storage modulus data is reported at 1 Hz excitation, with data collection at discrete temperature intervals where the chamber was allowed to equilibrate for four minutes. Failure strain data was collected in uniaxial tension by ramping tensile force on each sample at a rate of 1 N min^{-1} until failure. Shape fixity and recovery factors were determined according to the definitions provided in Ref. [169] for a single shape fixing and recovery cycle.

Test samples for dynamic mechanical analysis (DMA) and adhesive blister testing were created by pouring the resulting mixture onto glass plates and curing for several minutes at 100°C until the precursor becomes viscous enough to spread into a uniform and thin sheet. Curing was completed in an oven at 100°C for 90 minutes. Samples were cut from the resulting sheets using a laser cutter, then removed from the glass at elevated temperature.

A.5 Thermogravimetric Analysis

Thermogravimetric Analysis: A solid block of SMP was machined to produce approximately 4.17g of small shavings and powder for analysis within a Cahn Thermomax 500 Thermogravimetric Analyzer. The test was carried out under oxygen and nitrogen simulated atmospheric conditions from 50°C to

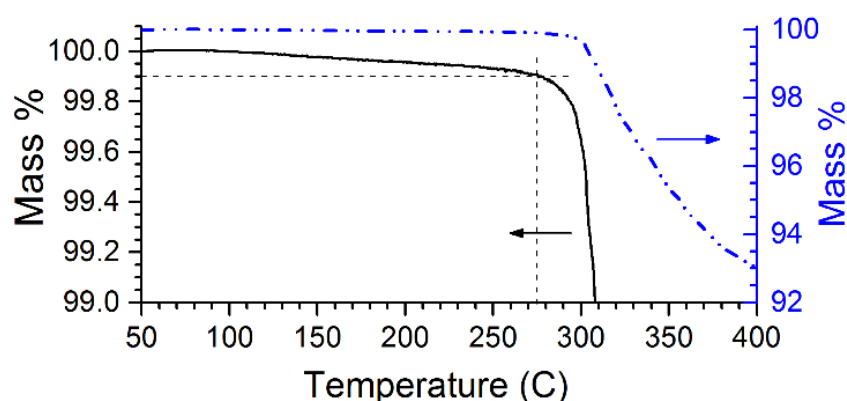


Figure A.1. Thermogravimetric analysis of NGDE2 from 50°C to 400°C . The full data set is shown as a dash-dotted blue line. The same data is shown with an expanded y-axis for greater detail as a solid black line, indicating the “degradation temperature” where the mass drops below 99.9% of its original value. $10^\circ\text{C min}^{-1}$ heating rate.

400 °C with a 10 °C min⁻¹ ramp. Temperature and weight measurements were recorded at one second increments.

A.6 Surface Roughness Characterization

An Asylum Research MFP-3D AFM was used to produce the surface roughness and microscale adhesion results. An SMP surface cured against a silicon wafer was used for both AFM roughness and micro scale adhesion testing. During adhesion testing, the SMP surface was additionally left exposed to air at 100 °C for two hours to reduce the possibility of air-to-SMP chemical interactions affecting surface chemistry during testing. A typical AFM image of 4.7 Å root mean square (RMS) roughness of SMP surfaces is shown in Figure A.2.

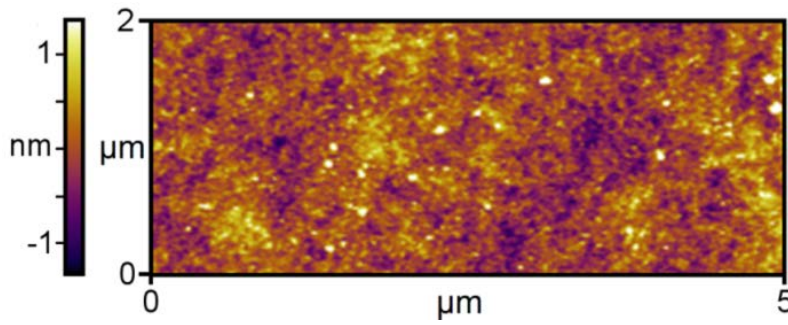


Figure A.2. AFM measurement of SMP surface roughness, cured against polished silicon. (RMS roughness = 4.7 Å)

A.7 Work of Adhesion to Silicon Measurement

The work of adhesion (γ) between a 1 μm diameter silica sphere and SMP near its glass transition range is calculated from atomic force microscope (AFM) adhesive force measurements in conjunction with the JKR theory of elastic contact using Equation A.1:[226]

$$F_c = -\frac{3}{2}\gamma\pi R \quad \text{Eq. A.1}$$

where R is the radius of the silica sphere, and the relationship is independent of elastic modulus. Measurements were taken in a grid, with 256 individual measurement locations using a 1 μm diameter silica particle tip. The indentation load is ~45 nN for each test with a speed of 2 μm s⁻¹ (Figure A.3).

The measurements were taken at 30 °C, while the polymer is in its rigid state. From the collected data, the work of adhesion is estimated to be 46 mJ m⁻².

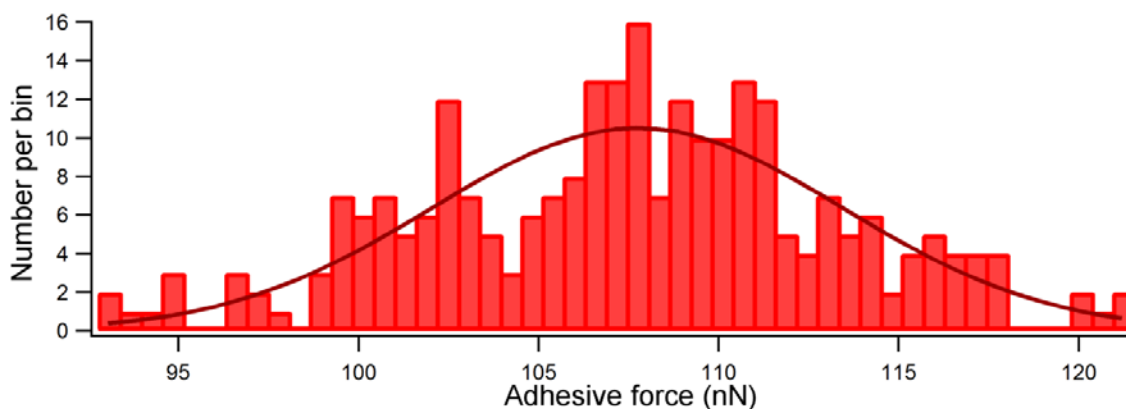


Figure A.3. AFM adhesive force histogram of 256 individual tests in a grid pattern at 30°C with a Gaussian curve-fit and mean of 108.7 nN.

A.8 SMP Thermal Expansion Coefficient

Thermal expansion was measured using a TA Instruments Q800 DMA by tracking the linear motion of a bar-shaped SMP sample with rectangular cross section of 0.7 mm² under a static load of 1 mN while it is incrementally heated and cooled. Temperature increments of 5 °C between -20 °C and 110 °C were used, except near T_g (35 °C to 60 °C) where temperature increments were reduced to 1 °C. The temperature was held isothermally for 5 minutes at each increment. The temperature range was spanned from -20 °C to 110 °C, then back to 20 °C, with the values in Figure A.4 reflecting the average of the two sets of data.

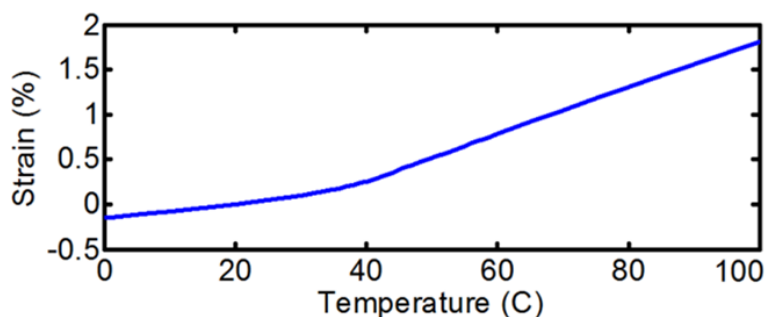


Figure A.4. Elongation due to thermal expansion is shown where zero strain is at 20 °C.

Appendix B. Single Microstamp, Micro-heater, and Ink Structure Fabrication and Performance Test Procedures

B.1 Microstamp Fabrication

Molds for the SMP stamps were fabricated using SU-8 on silicon wafers, using established methods [187]. The SMP stamps were fabricated on glass substrates by a double molding process utilizing PDMS (Sylgard 184 silicone elastomer kit). First, the SU-8 molds were treated with a non-stick layer (tridecafluoro-1,1,2,2-tetrahydrooctyltrichlorosilane; Sigma-Aldrich) by vapor deposition to facilitate mold release. PDMS was mixed in a 10:1 monomer to curing agent ratio and cured in the SU-8 molds at 100 °C for 30 minutes. The resulting PDMS stamps were then etched in an oxygen plasma for 15 seconds in a reactive ion etcher at 100 W to facilitate the bonding of a fluorinated non-stick layer, resulting in a low surface energy positive molds. These positive molds were used to make negative PDMS molds, again created with a 10:1 monomer to curing agent ratio and cured at 100 °C for 30 minutes. The resulting negative molds were then filled with a small volume of SMP precursor and pressed against a glass substrate for curing. When cured for use with a microscale heater, the mold cavity was aligned over the heater prior to curing at 100 °C for 90 minutes. Silica spheres were manually placed on flat-post stamps using precision stages. A small droplet of SMP precursor was first placed on an SMP flat-post stamp. Surface tension from the droplet was then used to pick and hold a single sphere prior to curing at 100 °C for 90 minutes.

B.2 Fabrication of Microheaters

The NiCr heater was fabricated by sputtering a 250 nm layer of NiCr on a glass substrate patterned with AZ 5214 photoresist, then lifting off excess NiCr by dissolving the photoresist in acetone under sonication. The final heater consists of a serpentine pattern of NiCr with approximately 1000 Ω resistance which heats the central stamp region to approximately 100 °C with 200 mW of power. Stamps are fabricated on the surface of the heater substrate using a PDMS negative mold. The mold is filled with SMP precursor, then pressed against the heater substrate and the stamp cavity aligned with the heater prior to curing. A thin layer of SMP approximately 50 μm coats the heater substrate, with the stamp situated within the central opening in the heater as depicted in Figure 4.4.

The ITO heater was fabricated by patterning AZ 5214 on an ITO-coated glass substrate, then etching the ITO with an 18% hydrochloric acid solution. The stamps are fabricated above the narrow central region of the ITO pattern in a manner similar to that described for the NiCr heaters. Due to its larger size compared with the NiCr heaters, this particular ITO design requires approximately 400 mW to achieve a similar temperature, and possesses a thermal response time on the order of one second.

B.3 Adhesion Tests for SMP stamps

To test the adhesion of the SMP stamps, the SMP stamps were mounted on precision translational and rotational stages. A small load cell (Transducer Techniques, GSO-25) was mounted below the stamp to measure the force between the stamp and the mating silicon substrate. The silicon substrate was placed atop a small ($\sim 0.5 \text{ cm}^3$) resistive heater mounted to the load cell to ensure consistent heating between the different stamps. To test the hot-state adhesion, the substrate surface was heated for approximately 3 minutes to attain a steady state temperature of 90°C . A custom program was written to control the movement of the stages to maintain a set preload. Using this program, the stamp was brought into contact with a preload of 10 mN. After one minute, the preload was reduced to 1.5 mN (release preparation in Figure 4.3), and five seconds after achieving this reduced preload the stamp and substrate were separated at varying speeds to generate adhesion data. To test adhesion as a function of storage modulus, the temperature of the stamp/substrate interface was monitored and the storage modulus was inferred from temperature based on material property data. After the bonding period at 90°C , the heater power was reduced to achieve the desired steady state temperature. Once this temperature was reached, preload was reduced to 1.5 mN for five seconds, followed by separation at the various speeds shown in Figure 4.3. To test the cold-state adhesion, the substrate was similarly heated, and after one minute of being held at 10 mN preload, power to the heater was shut off. Three minutes elapsed to ensure adequate cooling of the stamp below its T_g , and then the stamp was retracted at $5 \mu\text{m s}^{-1}$.

B.4 Assembly of Silicon Inks

An SMP microtip stamp heated by a thin-film NiCr resistive or an indium tin oxide (ITO) heater was used for retrieval and release of each silicon ink. Retrieval of a silicon ink was performed directly from a donor substrate and release was completed on a receiving silicon substrate or onto previously-printed silicon inks. During the retrieval step, the SMP stamp was heated prior to collapsing the full surface

area of the SMP on a silicon ink. While the SMP stamp was collapsed conformally on the silicon ink, the SMP was converted to cold state. Vertical retraction allowed retrieval of the ink from the donor substrate where the silicon ink was tethered. During the releasing step, the SMP stamp was heated to return to its adhesion-off state. The silicon ink was then released onto a desired receiving area or target structure. After retrieval-and-release cycle, the receiving substrate was moved to a furnace and annealed at 1000 °C for 5 minutes to bond the stacked silicon inks.

Appendix C. Laser-Activated Stamp Array Fabrication and Performance Test Procedures

C.1 Fabrication of SMP stamps

Molds for the SMP stamps were fabricated on silicon wafers, based on established microfabrication methods [187]. Microtips were etched into the wafer surface using KOH solution through a nitride mask. Drums were then etched using standard deep reactive ion etch (DRIE), with the posts formed by SU-8 50 processed to a depth of 45 μm . The SMP stamps were fabricated on glass substrates by a double molding process utilizing PDMS (Sylgard 184 silicone elastomer kit). First, the SU-8 molds were treated with a non-stick layer (tridecafluoro-1,1,2,2-tetrahydrooctyltrichlorosilane; Sigma-Aldrich) by vapor deposition to facilitate mold release. PDMS was mixed in a 10:1 base to curing agent ratio and cured in the SU-8 molds at 50 °C for six hours. After demolding, the resulting PDMS molds were then etched using oxygen (20 sccm) for 30 seconds in a reactive ion etcher at 200 mTorr and 100 W to facilitate the bonding of a silane non-stick layer, resulting in a low surface energy positive molds. These positive molds were used to make glass-mounted thin-film negative PDMS molds, to ensure surface flatness, again created with a 10:1 base to curing agent ratio and cured at 50 °C for six hours. This temperature was chosen to balance the effects of thermal expansion and curing shrinkage on the final product so that the SMP arrays spatially match with the ink arrays. The resulting negative molds were then lightly brushed with Cabot Vulcan XC72R powdered carbon black to coat all surfaces. Adhesive tape was repeatedly used to remove the excess carbon black, leaving only an adequate amount within the microstructures of the mold. The mold was then filled with a small volume of SMP precursor and pressed against a glass substrate for curing. When cured for use with a microscale heater, the mold cavity was aligned over the heater prior to curing at 50 °C for 24 hours followed by a 90 minute cure at 100 °C.

C.2 Fabrication of Silicon and Gold-Coated Silicon Inks

Square silicon inks were fabricated from silicon-on-insulator (SOI) wafers [182]. The shape of silicon square blocks were determined by patterning a masking layer of photoresist (AZ 5214) and then etching the exposed silicon layer using deep reactive ion etch. Wet etching with hydrofluoric (HF) acid removed the buried oxide to form an undercut trench below the perimeters of the patterned silicon inks. The

wafer was spin-coated with photoresist (AZ 5214) and flood-exposed, leaving only PR under the undercut trench after development. After final HF etching, silicon inks were suspended on photoresist which is tethered to the underlying silicon wafer and are ready for retrieval. For gold-coated silicon inks, the fabrication process is identical but with a final step consisting of first sputtering 5 nm of chrome followed by a 100 nm layer of gold. The chrome layer improves adhesion between the silicon and gold.

C.3 CBSMP Microstructure Absorption Tests

The illumination source during testing is an 807 nm continuous wave laser diode. Its beam is directed to the sample through a 200 μm core optical fiber terminated with a 4 mm collimator and a focusing lens with a 30 mm focal distance. A dichroic mirror is placed in the beam path to direct it onto the sample while allowing simultaneous observation using a digital video camera. The test samples are continuously illuminated at low laser power ($< 250 \text{ mW}$) with the laser focused to have a spot width of approximately 600 μm diameter. The diode temperature is kept at $19.8 \pm 0.5 \text{ }^{\circ}\text{C}$ to maintain consistent illumination intensity. For the power absorption tests, the laser is on continuously for a minimum of one minute until it reaches a steady state temperature, and remains on while photo-diode power takes continuous measurements of transmitted 807 nm radiation for at least one additional minute. The data for each continuous test are averaged to provide a representative measurement of the total transmitted power for that sample. This is performed at several locations of each sample to ensure uniformity of the samples, and repeatability of the results.

Appendix D. Large-Area Microtip Fabrication and Performance Test Procedures

D.1 Microtip Stress Fields and Size Selection

D.1.1 Finite Element Modeling

It is desirable to optimize the height and spacing of microtips so that they are large enough to reliably cause full delamination of the inter-microtip region, but no larger so that their impact on the maximum adhesive strength is minimal. The minimum height is a function of the SMP storage modulus, work of adhesion to the substrate material, detachment temperature and microtip spacing [187], [216]. Stresses are generated within the SMP microtips when they are compressed in the adhesion-on configuration. Cooling the material below its T_g traps these stresses internally within the polymer's molecular structure, eliminating the restoring force between SMP and substrate. When reheated, the stresses will be relieved and the restoring force reestablished. For delamination between SMP and substrate to occur, the released strain energy must exceed the work of adhesion of the contacting area.

In order to quantitatively determine the stress field in and around a compressed microtip and predict the optimal size, a quarter-symmetry finite element model of the large area SMP surface was developed using ABAQUS, with symmetry planes shown in Figure D.1 relative to the microtip locations. ABAQUS was used as it is particularly well suited for simulating transient dynamic events with an ability to handle severely nonlinear behavior such as contact and large deformation. The model was modified for 12 μm , 15 μm , 18 μm , and 21 μm microtip sizes as measured at the base. The backing layer thickness of the adhesive was modeled to be 400 μm , which is sufficiently far from the microtips for the top boundary to have a negligible impact on the microtip deformation. Adhesive force between substrate and SMP is modeled with linear springs to approximate the measured work of adhesion that was described earlier.

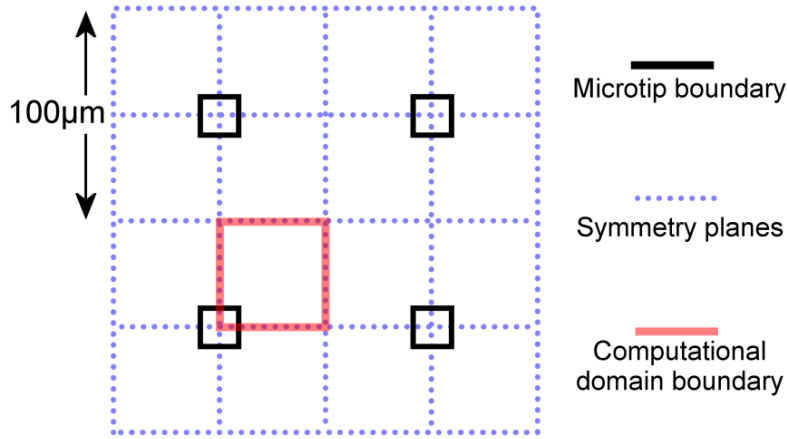


Figure D.1. Diagram of the quarter-symmetry used for FEM modeling.

The SMP is simulated in its rubbery state with elastic modulus of 10 MPa, a Poisson's ratio of 0.40, and the work of adhesion of 46 mJ m^{-2} (see Appendix A.7). A force is applied to the top of the SMP, opposite the microtip surface, pressing the SMP together with a substrate. The force is increased from 0 to 30 N cm^{-2} to simulate collapse, and then decreased to 0 N cm^{-2} to simulate re-heating following bonding where the elastic energy stored during the compression of the microtips acts to overcome the adhesive force to separate SMP and substrate.

The mesh is composed of both tetrahedral and structured quadrilateral elements. The area adjacent to the microtip was meshed using linear tetrahedral elements and distortion control was enabled for these

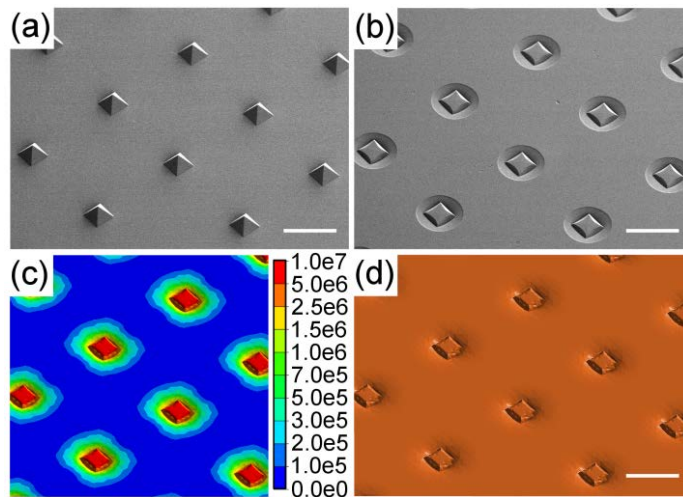


Figure D.2. (a) SEM image of SMP surface in the permanent and non-bonded state, (b) SEM image of SMP surface in the temporary and bonded state, (c) Von Mises stresses generated under 30 N cm^{-2} preload in FEM, and (d) corresponding FEM image showing the same temporary shape. (scale bars: 50 μm)

elements to ensure that these elements could withstand high deformation. The elements away from the microtip were meshed with structured linear quad elements without any distortion control to ensure optimal computational performance.

The validity of the FEM is checked by comparing to deformed SMP surfaces of the same dimensions. Scanning electron micrographs of a fabricated microtipped SMP in both its permanent and temporary shapes are shown in Figure D.2a,b, showing the microtips partially flattened and level with the collapsed inter-tip region, all of which now make intimate contact with the substrate. The collapsed, temporary shape reproduced with the FEM is shown in Figure D.2c,d along with the stress profile showing stresses concentrated near the microtips where deformation is greatest.

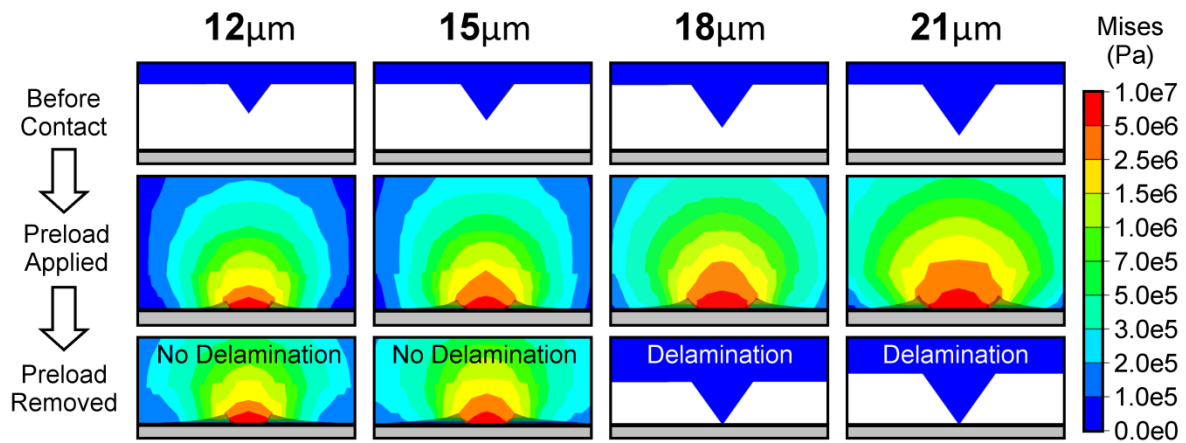


Figure D.3. Von Mises stress near four sizes of microtip calculated using FEM before, during, and after an equal preload is applied to each. The larger microtips store more strain energy when compressed, allowing easier delamination when the load is removed. Perfectly elastic behavior is assumed with a modulus of 10 MPa, corresponding to 90 °C.

It is clear that as the microtips increase in size, the surrounding stress field will likewise increase as the microtip is compressed to its adhesion on configuration. In order to estimate the required microtip height, the FEM is modified to simulate delamination conditions for several microtip sizes and assuming a center-to-center spacing of 100 μm for neighboring microtips. The results shown in Figure D.3 indicate the critical base-width to be between 15 μm and 18 μm for these conditions. Experimental observations indicate the critical base-width to be between 18 μm and 21 μm: a close result given the idealizations inherent in the computational analysis.

D.1.2 The Effect of Air Trapped and Compressed Near Microtips

As the SMP adhesive has preload applied, the inter-tip areas collapse to contact the substrate and seal off a volume of air surrounding the base of each microtip. As collapse proceeds, the air becomes pressurized, causing a repulsive force between adhesive and substrate. An estimate of the air pressure versus preload for several microtip sizes is shown in Figure D.4. Larger microtips require a larger preload before the intertip region collapses to seal the volume of air. The values are calculated from nodal positions using an FEM model that does not explicitly include the effect of the air pressure, and therefore are expected to be conservatively large.

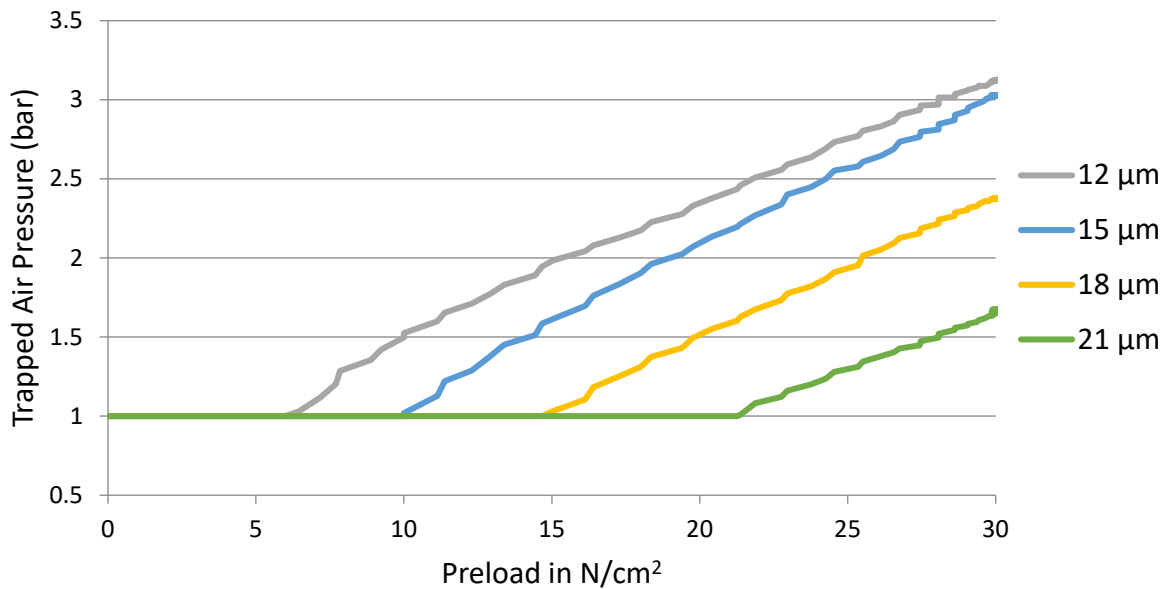


Figure D.4. Plot of the pressure of the air trapped around each microtip as preload is increased for various microtip sizes, obtained by FEM.

From Figures D.2 and 5.3, it may be seen that for a cross section at the SMP-substrate interface, the air pockets are $< 10\%$ of the total area. Assuming trapped air at a pressure of 3 bars acting over 10% of the interface, a conservatively high repulsive force of 3 N cm^{-2} (0.3 bar) is calculated. The total effective strength of our SMP adhesive is on the order of 200 N cm^{-2} (20 bar), and therefore it is concluded that the trapped air does not have a significant direct effect on the strength of adhesion.

It may be noticed in Figure D.2 that the FEM appears to predict shallower air pockets than the SEM images indicate. This is most easily explained by noting that the FEM mesh is large relative to the feature size in question, thus it is unable to capture such fine detail. Two other factors not present in

the FEM are expected to contribute to the shape seen in experimental SEM images. The FEM does not include the force of the compressed air, which should act to create more circular, slightly deeper pockets. However, it is also evident from Figure 5.3 that the line of contact between SMP and substrate along the global collapse front is similarly well defined even though no trapped air is present. The discrepancy in shapes may be better explained by the fact that in the case of the SEM images, the SMP is cooled to complete the bond. During the cooling process, the polymer contracts slightly and pulls back away from the substrate, enhancing the “sharpness” of the interface edges.

D.2 Silicon Microtip Pattern Molds

A mold was prepared to generate the pyramid microtip pattern in the SMP. The mold was created by first depositing a silicon nitride layer on a clean Si (100) wafer. A layer of photoresist was spin-coated and patterned to form square openings each 20 μm across in a square pattern with 100 μm center-to-center spacing. The silicon was exposed by etching the nitride briefly in a 10:1 BOE (buffered oxide etch) bath. The photoresist was then removed. Etching in a KOH solution (70 g KOH, 190 ml H₂O, 40 ml IPA) at 80 °C formed the pattern of pyramid recesses in the wafer using the remaining nitride layer as a mask. Finally, the nitride layer was removed, and the completed mold was coated with trichlorosilane for silanization in a vacuum chamber for 1 hour.

D.3 Bonding Procedure

A clean glass slide is placed on a custom temperature controlled aluminum heater, and is heated to 90 °C. The SMP sample is placed on the center of the glass slide so that the microtip patterned surface contacts the slide. The sample is allowed to sit on the slide for five minutes to come to thermal equilibrium, and force is then applied acting perpendicular to the SMP-to-glass interface by pressing on the top of the affixed ball bearing by applying a fixed weight. The weight is applied gradually, increasing over the course of several seconds. The heater remains on for two additional minutes while allowing the viscoelastic SMP to relax towards mechanical and thermal equilibrium in its collapsed state. The heater is switched off, and a gentle air flow is applied over the system to hasten the cooling process which lasts for seven minutes. The SMP and glass slide are now bonded.

Appendix E. Conductive CBSMP Fabrication and Performance Test Procedures

E.1 CBSMP Blend Preparation

The constituents of CBSMP blends were proportioned by weight and mixed manually using a stirring rod. The SMP mixture used the NGDE2 formula (Appendix A.1) and was prepared prior to adding CB. The base SMP precursor is a somewhat viscous liquid but is thickened considerably by the addition of CB. Blends containing greater than 10 wt% CB become pastes, while exceeding 25 wt% CB results in a thick, clumpy mixture that must be manually packed into molds to form the desired shapes. This was accomplished by shearing the mixture over the surface of the molds using a clean razor blade. The 5 wt% CB blends were observed to have many larger voids formed by bubbles trapped during the mixing process. This sometimes lead to fragile specimens. This issue was less prevalent at 10 wt%, since the mixture was thickened enough that the small trapped bubbles were no longer able to expand during curing.

E.2 15/30 CB Composite Design

The composite 1 mm thick conductive layer is fabricated with 30 wt% CB islands, connected with 15 wt% CB filler. The islands are 3.5×3.5 mm on the electrical contact side, tapering to 3×3 mm on the opposing side for easier release from the mold in which they are cured. The center-to-center spacing is 5 mm. This design provides roughly even distribution of the two CBSMP blends exposed on the electrical contact surface.

Appendix F. Blister Test Procedure and Demonstrative Prototype Fabrication

F.1 Blister Adhesion Testing

Thin (~0.50 mm) circular samples of several SMP formulations were bonded to form a seal over the 1 cm diameter circular glass opening of a pressure chamber by first heating the glass surface to 75 °C, followed by light pressure to ensure SMP-glass contact and maintaining 75 °C for three minutes. Temperature was controlled by an AGPtek® universal digital PID temperature controller. Tests were performed after allowing the sample to cool to the desired temperature. The flexibility of the thin SMP membranes allowed them to self-conform to the glass adherend when heated, obviating the need for preload during the bonding process. Pressure was applied through a manual regulating system, increasing pressure by ~10 psi min⁻¹ until interfacial failure was observed to have initiated.

F.2 Practical Adhesive Demonstration

Nichrome wire with 0.62 mm diameter was obtained from Sigma Aldrich and formed into a ~0.5 Ω heating element. The SMP formulation E448-J100 (Table) was applied in three layers. First, a flat sheet of SMP ~1 mm in thickness was formed by pouring the precursor on a glass surface and curing. The second layer encapsulated the NiCr heating element, then a third very thin layer bonds the first two layers to the 3D printed handle piece. Power is provided by a 7.4V lithium polymer battery.

Appendix G. Examples of Published Dry Adhesive Performance

The performance of a selection of dry adhesives as measured by their authors are provided below, organized by the adhesive performance metric used by the authors: Table G.1 reports normal adhesion measurements, Table G.2 reports shear adhesion measurements, and Table G.3 reports work of adhesion measurements.

List of acronyms used in Tables G.1, G.2, G.3: polycarbonate (PC), polypropylene (PP), polyurethane (PU), poly(ϵ -caprolactone) (PCL), shape memory polymer (SMP), polydimethylsiloxane (PDMS), carbon nanotube (CNT), single-walled carbon nanotube (SWCNT), multi-walled carbon nanotube (MWCNT), hexamethyldisilazane (HMDS), high density polyethylene (HDPE).

Table G.1. Measurements of Normal Adhesion.

SMP: shape memory polymer, PDMS: polydimethylsiloxane, PU: polyurethane, PCL: poly(ϵ -caprolactone), CNT: carbon nanotube, SWCNT: single-walled carbon nanotube, MWCNT: multi-walled carbon nanotube.

Surface Structure	Material	Test Method	Test Scale (mm)	Max. Normal Adhesion (N cm ⁻²)	Reversibility	Reference
microtips	epoxy SMP	glass adherend, free-hanging weight	10	200	~1000:1 microstructure, rigidity control	[223]
flat	epoxy SMP	glass adherend, free-hanging weight	100	5–30	-	[206]
microtips, flat, microspheres	epoxy SMP	Si adherend, load cell w/motor stage	0.1	700 (flat) 560 (microtip)	2:1 (flat) ~1000:1 (microtip) microstructure, rigidity control	[194]
microtips, flat	PDMS	Si adherend, load cell w/motor stage	0.1	3–6	>100:1 microstructure	[182]
flat	PDMS	Si adherend, load cell w/motor stage	0.1	7	~100:1 shear displacement	[188]
flat/angled	PDMS	Si adherend, load cell w/motor stage	0.1	10	~100:1 shear displacement	[46]
flat	PU or PDMS/carbon composite	glass adherend, universal mechanical tester, center loading	100	7.5 ^(a)	300:1 ^(b) loading location	[56]
spatula microfibrillar, flat	PDMS Crystalbond filler	6 mm sapphire lens adherend, load cell w/motor stage	1	20	~5:1 fibrillar ~20:1 flat rigidity control	[227]
flat	PCL and bisphenol-A epoxy	Al and stainless steel adherends, universal mechanical tester	10	80 to 650 ~200 solvent self-bonding	>75:1 heat release	[228]
microfibrillar, smooth	epoxy polymer PDMS	4 mm spherical sapphire adherend, interferometer w/motor stage	1	~1 ^(c)	4:1 loading rate	[198]

Table G.1. (cont.)

film-terminated fibrillar	PDMS	Si adherend, double-cantilever beam	1	2.6 fibrillar ~4 flat	-	[122]
nanofibrillar	CNT	glass adherend, free-hanging weight	4	~10	~10:1 loading direction	[229]
nanofibrillar	SWCNT, MWCNT	glass adherend, laboratory balance	4	12 MWCNT, 28 SWCNT	-	[230]
nanofibrillar	MWCNT	glass adherend, laboratory balance	2	11.7	-	[81]
nanofibrillar	Polyimide	glass adherend, laboratory balance	10	3	-	[167]
microfibrillar	PDMS	Si adherend, displacement sensor w/motor stage	8	0.6 maximum	20:1 shear displacement	[231]
inflatable hemisphere	ST-1060 PU	flat glass adherend, load cell w/motor stage	10	~0.5	204:1 inflation displacement	[232]
gallium liquid	PDMS with gallium liquid	glass, Au, Si, PDMS adherends, load cell w/motor stage	1	2.9 (smooth glass) 3.74 (silicon) 4.4 (gold)	178:1 rough glass 113:1 smooth glass 86:1 silicon Ga phase change	[233]
thick film-terminated fibrillar	PDMS/Fe-PDMS	spherical glass adherend, load cell w/motor stage	10	2.4	minimal, magnetic field orientation	[168]
micro-ridges	PDMS/Fe-PDMS	<1 mm glass sphere, cantilever deflection measurements	1	0.1	~10:1 magnetic field orientation	[234]
microfibrillar, various tips	PU ST-1060, ST-1087	6 mm glass sphere adherend, load cell w/motor stage	6	>0.05	-	[72]
flat	epoxy SMP, elastomer	PC and PP adherends, universal mechanical tester	10	100	>100:1 shape change	[59]
flat, single and dual layer microfibrillar	PU	12 mm spherical glass adherend, load cell w/motor stage	1	2.7 (flat) 5.9 (single layer) 3.75 (dual layer)	-	[47]

^(a) Shear (0°) adhesion reported as 29.5 N cm⁻². From Figure 2b in Ref. [56], normal adhesion is ~25% of this value; ^(b) From the caption of supporting information Figure 4 in Ref. [56]; ^(c) Estimated from the reported adhesive forces, with 4 mm diameter spherical probe, and reported maximum indentation depth of 100 µm.

Table G.2. Measurements of Shear Adhesion.

PC: polycarbonate, PP: polypropylene, HDPE: high density polyethylene, HMDS: hexamethyldisilazane.

Surface Structure	Material	Test Method	Test Scale (mm)	Max. Shear Adhesion (N cm ⁻²)	Reversibility	Reference
nanofibrillar	CNT	Cu adherend, spring scale w/manual force application	10	37 at 25 °C 124 at 1030 °C	-	[45]
nanofibrillar	CNT	glass adherend, free-hanging weight	4	~100	~10:1 loading direction	[229]
nanofibrillar, hierarchical	CNT/SU-8 hierarchical	HMDS-treated 1 mm glass sphere and 1.5 mm roughened steel sphere, load cell w/motor stage	10	~20	large ^(a) , normal vs. shear loading	[70]
nanofibrillar	SWCNT, MWCNT	glass adherend, laboratory balance	4	7 MWCNT, 17 SWCNT	-	[230]
nanofibrillar	MWCNT	glass adherend, laboratory balance	2	7.7	-	[81]
spatula microfibrillar	conductive PDMS (carbon black)	PP adherend, spring scale	100	0.4	-	[90]
microfibrillar	PP	glass adherend, load cell w/motor stage	20	2	~1000:1 peeling vs. shearing	[235]
microfibrillar, various tips	PU ST-1060, ST-1087	6 mm diameter glass sphere adherend, load cell w/motor stage	1	>0.15	-	[72]
flat	epoxy SMP, elastomer	PC and PP adherends, universal mechanical tester	10	55	>100:1 shape change	[59]
microfibrillar	HDPE	glass adherend, hanging water cup	10	4.7	-	[236]
nanofibrillar	Germanium/Parylene nanowires	self-adhering, wet and dry conditions	5	30	-	[44]
flat	PU or PDMS/carbon composite	glass adherend, universal mechanical tester, center loading	100	29.5 max 26.0 avg.	300:1 loading location	[56]
microfibrillar	PU	6 mm diameter glass sphere adherend, load cell w/ motor stage	1	41	-	[237]

^(a) The normal adhesion is reported in the supporting information of [70] to be undetectable to the test equipment.

Table G.3. Measurements of Work of Adhesion.

Surface Structure	Material	Test Method	Test Scale (mm)	Work of Adhesion (J m^{-2})	Reversibility	Reference
film-terminated fibrillar	PDMS	Si adherend, double-cantilever beam	1	0.137 (flat) 1.2 (fibrillar)	-	[122]
nanofibrillar	SWCNT, MWCNT	glass adherend, laboratory balance	4	0.07–0.2	-	[230]
nanofibrillar	MWCNT	glass adherend, laboratory balance	2	0.02–0.08	-	[81]
flat, single and dual layer microfibrillar	PU	12 mm spherical glass adherend, load cell w/motor stage	1	0.002 (flat surface) 0.034 (dual layer)	-	[47]
flat, incised	PDMS	silanized glass plate adherend, cantilever actuated by linear motor w/load cell	10	≤ 0.8 (crosswise incisions) ~ 0.1 (smooth surface)	-	[48]
film-terminated fibrillar	PDMS	8 mm diameter spherical glass adherend, load cell w/motor stage	1	0.3 (fiber/film) 0.12 (flat control)	-	[123]